

2018

# Experimental studies of heat transport across material interfaces at the nano and micro scales

---

<https://hdl.handle.net/2144/32340>

*Downloaded from DSpace Repository, DSpace Institution's institutional repository*

BOSTON UNIVERSITY  
COLLEGE OF ENGINEERING

Dissertation

**EXPERIMENTAL STUDIES OF HEAT TRANSPORT  
ACROSS MATERIAL INTERFACES AT THE NANO AND  
MICRO SCALES**

by

**MIGUEL ANGEL GONI RODRIGO**

B.S., Public University of Navarra, 2011

M.S., University of Rhode Island, 2013

Submitted in partial fulfillment of the

requirements for the degree of

Doctor of Philosophy

2018

© 2018 by  
MIGUEL ANGEL GONI RODRIGO  
All rights reserved

Approved by

First Reader

---

Aaron J. Schmidt, PhD  
Assistant Professor of Mechanical Engineering  
Assistant Professor of Materials Science and Engineering

Second Reader

---

Chuanhua Duan, PhD  
Assistant Professor of Mechanical Engineering  
Assistant Professor of Materials Science and Engineering

Third Reader

---

J. Scott Bunch, PhD  
Associate Professor of Mechanical Engineering  
Associate Professor of Materials Science and Engineering  
Associate Professor of Physics

Fourth Reader

---

Keith A. Brown, PhD  
Assistant Professor of Mechanical Engineering  
Assistant Professor of Materials Science and Engineering  
Assistant Professor of Physics

*Water has a pH 7 and I have a ph d*

## Acknowledgments

I would like to start my acknowledgments with my PhD advisor **Professor Aaron J. Schmidt** for recruiting me and giving me the opportunity to fulfill one of my life goals. I want to thank him for all the research training he provided me as well as for allowing me to build important teaching and mentoring experience. Thanks to him I have made a lot of progress at conducting research, analyzing experiments and communicating results. I will always be thankful to him for his trust and guidance.

I would also like to thank my committee members, **Professor Chuanhua Duan**, **Professor Scott Bunch** and **Professor Keith Brown**, for their help and rigor to guarantee the quality of my research. They all work hard at conducting outstanding research and I wish them the best success in their scientific careers.

I want to thank our main collaborator, NAMICS, for all their committed support during all my PhD years. It was a constant source of research ideas that helped me greatly.

I cannot forget two essential pieces that allowed me to get to this point, my labmates **Jia Yang** and **Elbara Ziade**. I am deeply thankful to both of them for welcoming me to the lab, for all the work they had done prior to my arrival, for patiently training me during my first year and for all the useful discussions we held for so many days. I would also like to thank the rest of the graduate students in the department for all their help at specific moments, especially **David Lloyd**, **Lauren Cantley**, **Corey Pollock**, **Leonard Kogos**, **Nourin Alsharif** and **Erin Arai**. Special thanks to **Rami Yazbeck** for all his help with the SEM. In addition, I would like to thank all the ME department and Photonics Center staff for always treating me so nicely and for being so helpful when I needed them.

Finally, I would like to thank my friends (**Helen**, **Jim**, **Pierre**, **Nora** and **Emily**) and tennis crew (**Mike**, **Rob**, **Hannu**, **German** and **Ed**) for all the moments we

shared in Boston and for often refreshing my mind, which definitely helped with my work at BU. I want to especially thank **Bob Diehl** for his support and mindfulness. And of course to **my family** for teaching me since very little the values of humbleness, perseverance, respect and hard work that were the foundation and most important tools for this PhD work. Thank you all.

Miguel Goni Rodrigo

Boston University

**EXPERIMENTAL STUDIES OF HEAT TRANSPORT  
ACROSS MATERIAL INTERFACES AT THE NANO AND  
MICRO SCALES**

**MIGUEL ANGEL GONI RODRIGO**

Boston University, College of Engineering, 2018

Major Professor: Aaron J. Schmidt, PhD  
Assistant Professor of Mechanical Engineering  
Assistant Professor of Materials Science and  
Engineering

ABSTRACT

Heat generated by electronic devices must be dissipated in order to ensure reliability and prevent device failure. In order to design devices properly, it is important to have precise knowledge of materials' thermal properties at the nano and micro scales. Here we present a series of experimental studies of heat transport for two different types of material: a two dimensional (2D) material such as MoS<sub>2</sub> and micron scale particles. We used frequency domain thermoreflectance (FDTR) to conduct all thermal property measurements. This technique can measure thin film thermal properties as well as characterize the interface between two materials.

Molybdenum disulfide (MoS<sub>2</sub>), a transition metal dichalcogenide, is a 2D material that has potential applications as a transistor in nanoelectronics due to its semiconductor properties. We studied cross plane thermal transport across exfoliated monolayer and few layer MoS<sub>2</sub> deposited on two distinct substrates: SiO<sub>2</sub> and Muscovite mica. The cross plane direction is critical in layer structure devices since the

largest thermal resistances are found along this way. The results show enhanced thermal transport across monolayer MoS<sub>2</sub> on both substrates indicating that monolayer MoS<sub>2</sub> has superior thermal properties for its use in electronic devices. On the other hand, thermally conductive micro particles are used as fillers in composite materials in order to improve the thermal conductivity of the host or matrix material. They can be embedded in polymers for die attach applications as well as in metals to create more efficient heat sinks. We developed new FDTR based thermal models that apply to isolated particles as well as particles surrounded by another material. We tested the models with isolated diamond and silicon micron size particles and with diamond particles embedded in tin. We were able to obtain the thermal conductivity of individual particles, an effective particle volume and the thermal interface conductance between a particle and its surrounding matrix. This technique could have important applications in industry since it could be used to measure in situ the thermal interface conductance between particles and their matrix, often the highest thermal resistance in composite materials.

# Contents

<b>1</b>	<b>Introduction</b>	<b>1</b>
1.1	Two dimensional (2D) materials . . . . .	2
1.2	Particle enhanced thermal management materials . . . . .	3
1.3	Thesis outline . . . . .	4
<b>2</b>	<b>Frequency Domain Thermorefectance (FDTR)</b>	<b>7</b>
2.1	FDTR Imaging . . . . .	8
<b>3</b>	<b>Thermal transport across monolayer and few layer MoS<sub>2</sub></b>	<b>12</b>
3.1	Introduction . . . . .	12
3.2	Experimental methods . . . . .	13
3.3	Results and discussion . . . . .	20
3.4	Conclusions . . . . .	27
<b>4</b>	<b>Measuring individual micro particles with FDTR</b>	<b>29</b>
4.1	Introduction . . . . .	29
4.2	Theory . . . . .	30
4.2.1	Model derivation . . . . .	32
4.3	Experimental methods . . . . .	39
4.3.1	Particles modeling . . . . .	41
4.3.2	Fitting procedure and uncertainty of the fit . . . . .	44
4.4	Results and discussion . . . . .	51
4.4.1	Spot size effects . . . . .	54
4.4.2	Heating effects . . . . .	54

4.4.3	Thermal conductivity of all particles measured . . . . .	55
4.4.4	Particle shape dependence . . . . .	57
4.5	Conclusion . . . . .	59
<b>5</b>	<b>Measuring particle-matrix interfaces with FDTR</b>	<b>60</b>
5.1	Introduction . . . . .	60
5.2	Experimental methods . . . . .	61
5.2.1	Sample preparation . . . . .	61
5.2.2	Frequency Domain Thermorefectance (FDTR) . . . . .	61
5.3	Thermal model . . . . .	63
5.4	Sample results . . . . .	71
5.5	Conclusion . . . . .	78
<b>6</b>	<b>Conclusions</b>	<b>80</b>
6.1	Summary of the thesis . . . . .	80
	<b>References</b>	<b>82</b>
	<b>Curriculum Vitae</b>	<b>89</b>

# List of Tables

3.1	Anisotropic thermal conductivity of bulk MoS <sub>2</sub> and mica and the thermal interface conductance to Au/Ti. $k_{cr}$ represents cross-plane thermal conductivity, $k_{in}$ represents in-plane thermal conductivity and G represents the thermal interface conductance between the transducer layer and the bulk sample. . . . .	18
3.2	Thermal interface conductance values according to hypothesis A. . . .	27
3.3	Thermal interface conductance values according to hypothesis B. . . .	28
4.1	Fitting parameter values for the best fit of each diamond and silicon particle size shown in Fig. 4-11 as well as the silicon bulk sample. D stands for diamond and Si for silicon. . . . .	52
5.1	Fitted parameter values for the best fits of the three diamond particles shown in Fig. 5-8. . . . .	76
5.2	Fitted parameter values for the best fits of all diamond-tin particles measured. . . . .	77

# List of Figures

1·1	Thermal interface material (Corporation, 2016) . . . . .	3
1·2	Effective thermal conductivity of a diamond-aluminum composite for different values of the thermal interface conductance ( $G$ ) between the particles and the matrix. Calculations according to the Bruggeman model (Pietrak and Winiewski, 2015; Every et al., 1992) for a diamond particle size of 30 $\mu\text{m}$ diameter and an aluminum matrix. . . . .	5
2·1	a) FDTR setup. b) Schematics of a three layer sample used to extract the thermal properties of the $\text{SiO}_2$ layer. c) FDTR phase data and the thermal model best fit for the sample shown in b). . . . .	8
2·2	Sample 1 made out of silver powder and metallo-organic silver paste encased between a doped silicon die (top) and a metal substrate (bottom). a) Optical image, 50X objective. b) The thermal conductivity image shows clear silver migration towards the bottom of the die attach film. . . . .	10
2·3	Sample 2 made out of silver powder, metallo-organic silver paste and OMS particles encased between a doped silicon die (top) and a metal substrate (bottom). a) Optical image, 50X objective. b) The thermal conductivity image shows the OMS micro particles, voids, and silver migration within the matrix. . . . .	11

2·4	Sample 3 made out of silver powder, metallo-organic silver paste and OMS particles encased between a doped silicon die (top) and a metal substrate (bottom). a) Optical image, 50X objective. b) The thermal conductivity image shows the OMS micro particles and silver migration within the matrix. . . . .	11
3·1	a) AFM image of an MoS <sub>2</sub> flake on mica. b) Step height analysis on an MoS <sub>2</sub> flake across the dashed white line in the previous AFM image. c) Optical image of MoS <sub>2</sub> flakes on mica. d) Optical image of MoS <sub>2</sub> flakes on SiO <sub>2</sub> . e) AFM roughness measurement of mica (R <sub>q</sub> = 0.065 nm, R <sub>max</sub> = 0.63nm). f) AFM roughness measurement of SiO <sub>2</sub> (R <sub>q</sub> = 0.165 nm, R <sub>max</sub> =1.51nm). . . . .	14
3·2	Schematics of the multilayer models used to extract the thermal properties of mica and MoS <sub>2</sub> . On top, the samples used to obtain the anisotropic thermal conductivity of bulk MoS <sub>2</sub> and mica. G is the thermal interface conductance, k <sub>in</sub> and k <sub>cr</sub> are the in-plane and cross-plane thermal conductivity, respectively. On the bottom, the mono and few layer MoS <sub>2</sub> samples on SiO <sub>2</sub> and mica, for which G <sub>eff</sub> was measured. . . . .	17
3·3	Top: FDTR data and best model fit for the bulk MoS <sub>2</sub> sample. Bottom: FDTR data and best model fit for the mica substrate. In all cases a model prediction when we vary the fitted values by ± 50% is represented by the dashed lines. . . . .	19
3·4	Uncertainty of G <sub>eff</sub> for a wide range of values. Calculated using Eq. 3.1, it also indicates how sensitive FDTR is to the measurement of G <sub>eff</sub> . .	20

3·5	Effective thermal boundary conductance ( $G_{\text{eff}}$ ) for MoS <sub>2</sub> on SiO <sub>2</sub> and mica. a) shows the full comparison of $G_{\text{eff}}$ between SiO <sub>2</sub> and mica. Error bars for mica are the size of the symbol. b) is a zoomed in view for $G_{\text{eff}} < 25 \text{ MW/m}^2\text{K}$ in order to see the trend and error bars. . . .	22
3·6	Roughness measurements of monolayer and few layer MoS <sub>2</sub> samples carried out with AFM. The measurements were done prior to coating with the metal transducer layer. Samples on SiO <sub>2</sub> show a clear decreasing trend while mica sample remain more constant at a low roughness. . . . .	24
3·7	Hypothesis used in the alternative model. Roughness and MoS <sub>2</sub> dimension are set to scale. . . . .	25
4·1	a) Schematic of finite cylindrical layer model. It includes for an arbitrary number of layers and accounts for thermal interface resistance between layers, as well as a convection boundary on the sides ( $r = b$ ) b) Closer look at the top layer. A Gaussian periodic heat flux is applied to the sample. . . . .	31
4·2	Model prediction of the phase lag, $\phi$ , for particles with different sizes and for infinitely wide layers. . . . .	39
4·3	a) SEM image of several natural diamond particles of the 20 $\mu\text{m}$ size. b) FDTR image of several diamond particles. Some particles present a region oriented perpendicular to the laser beams where it is possible to carry out the measurement. c) Zoomed view of a diamond particle and the spot where the lasers were focused. d) FDTR phase data acquired for multiple frequencies. . . . .	41

4.4	a) SEM images of silicon particles. The size ranged between 30 and 100 $\mu\text{m}$ in diameter. b) FDTR image of silicon particle P1. The arrow points at the spot where the measurement was conducted. The white dash line indicates the particle boundary. c) FDTR phase data acquired for Si particle P1. . . . .	42
4.5	Effect of including the substrate in the model. The value of a thermal interface conductance ( $G_{\text{sub}}$ ) between the particle and the substrate would be under 0.1 MW/m <sup>2</sup> K, which does not affect the phase response at the measurements frequency range. Curves shown for a 10 $\mu\text{m}$ size diamond particle. . . . .	43
4.6	Effect of the convection coefficient on the temperature phase response for multiple size diamond particles. An unreasonably high convection coefficient is necessary to observe any effect at our measurement frequency range. The size is given as the average diameter. . . . .	45
4.7	Effect of the convection coefficient on the temperature phase response for multiple size silicon particles. An unreasonably high convection coefficient is necessary to observe any effect at our measurement frequency range. The size is given as the average diameter. . . . .	46
4.8	Uncertainty of the particle's thermal conductivity for a wide range of thermal conductivities in a three parameter fit ( $b, k, G$ ). For 10 $\mu\text{m}$ size diamond particles, the uncertainty becomes too large and therefore it is not possible to fit the three parameters simultaneously. For silicon particles, a three parameter fit is possible for any of the sizes shown. .	48

4·9	a) Sensitivity curves of parameters $b$ , $d$ , $k$ and $G$ for all four diamond particle sizes measured in this work. Frequency $F_b$ represents the time at which heat reaches the particle boundaries. Frequency $F_{\text{peak}}$ relates to the external time constant used in lumped systems. . . . .	50
4·10	Comparison between $F_{\text{peak}}$ and the lumped system time constant $(\rho c_p V R_{\text{th}})^{-1}$ in diamond particles of different sizes. For diamond, $R_{\text{th}} = 1/(GA)$ since the interface conductance is the dominant resistance to heat transferring in and out of the particle. . . . .	51
4·11	a) FDTR data and thermal model best fits for all four different size diamond particles. The thermal model shows an excellent fit to the measured data. b) FDTR data and thermal model best fits for the silicon particles and silicon bulk sample. . . . .	53
4·12	Temperature phase response for different laser input powers. The curves do not show any significant dependence to input power. . . . .	55
4·13	FDTR measured phase vs. frequency for all diamond particles. . . . .	56
4·14	Thermal conductivity of all diamond particles measured in this thesis. There is not evident trend of a volume dependence. . . . .	56
4·15	FDTR measured phase vs. frequency for the silicon particles. . . . .	57
4·16	Thermal conductivity of all silicon particles measured in this thesis. There is a trend indicating reduced thermal conductivity for smaller particles. This might be due to a higher defect density in the smaller particles introduced during the crushing fabrication process. . . . .	58
4·17	Phase response depending on the shape of the particle for a constant volume. We varied the ratio between the radius ( $b$ ) and depth ( $d$ ) of the particle to show the phase response does not strongly depend on the shape but it does on the volume. . . . .	58

5.1	SEM images of the diamond tin samples fabricated for this work. The particles are diamond and the matrix is tin. . . . .	62
5.2	a) Particle-matrix model. Both the particle and matrix are cylindrical. The matrix cylinder was large enough to be able to assume zero heat flux at the outer boundaries. A gaussian heat flux was applied to the top surface. b) Model geometry used for MATLAB PDE toolbox. Interfaces were modeled as layers with zero heat capacity and thermal conductivity, $k_{int} = G_{int} \cdot th$ , where $G_{int}$ is the thermal interface conductance of the interface and $th$ is the thickness of the interface layer. c) Mesh used to solve the model. Inset: zoomed in view of the area where the lasers were focused showing at least 10 nodes per micron to properly capture heat flux on that important region. . . . .	65
5.3	Thermal penetration depth in tin for a wide range of frequencies. We modeled the matrix material as 30% larger than the thermal penetration depth at the lowest frequency. This way we could correctly assume no heat flux at the matrix outer boundaries. . . . .	66
5.4	Phase response comparison between the current particle-matrix model with $G = 0$ and the model derived in Chapter 4. We did this to see how accurate the numerical solution was. The curves correspond to a $30 \mu m$ diamond particle coated with a metal transducer layer. . . . .	69
5.5	Uncertainty of $G$ for different particle sizes and materials as a function of the matrix thermal conductivity and the $G$ value itself. $G$ values: 0.1, 0.5, 1, 5, 10, 20, 30, 40, 50 MW/m <sup>2</sup> K. Arrow points in the direction of increasing $G$ . . . . .	72

5.6	Sensitivity plot of the fitting parameters $rad$ , $k_p$ , $g$ and, $G$ . The values used for this plot were $10 \mu\text{m}$ , $1200 \text{ W/mK}$ , $165 \text{ MW/m}^2\text{K}$ and $5 \text{ MW/m}^2\text{K}$ respectively. . . . .	73
5.7	Phase response depending on the shape of the particle for a constant volume. We varied the ratio between the radius ( $rad$ ) and depth ( $dep$ ) of the particle to show the phase response does not strongly depend on the shape but it does on the volume. . . . .	74
5.8	a) FDTR data and best fit for a measurement of the tin matrix. The fitted properties were the thermal interface conductance to the transducer layer and the thermal conductivity of tin. It provided a thermal conductivity of $63 \text{ W/mK}$ . b) FDTR data and best fits for diamond particles in tin. The figure on top also shows the model prediction for a $G$ 25% higher and lower than the one obtained for the best fit. . . .	75
5.9	FDTR phase data for diamond particles embedded in tin. . . . .	76
5.10	FDTR phase response for three different thermal models: the solid line represents the particle-matrix model developed in this chapter; the dashed line represents the conventional multilayer model with infinitely wide layers; the dashed-dot line represents the isolated cylindrical layers model ( $h = 0$ ). . . . .	78

## List of Abbreviations

AFM	.....	Atomic Force Microscope
C	.....	Celsius
CTE	.....	Coefficient of Thermal Expansion
FDTR	.....	Frequency Domain Thermoreflectance
MFPs	.....	Mean Free Paths
MoS <sub>2</sub>	.....	Molybdenum Disulfide
OMS	.....	Organically Modified Silicate
SEM	.....	Scanning Electron Microscope
SiO <sub>2</sub>	.....	Silicon Dioxide
TBC	.....	Thermal Boundary Conductance
TDTR	.....	Time Domain Thermoreflectance
TIM	.....	Thermal Interface Material
2D	.....	Two Dimensional

## Chapter 1

# Introduction

Managing the temperature of semiconductor junctions in electronic devices such as computers, phones, displays or micro-controllers is important for a reliable performance. Some studies have shown how an increase in the device temperature implies a significant drop in reliability and lifetime (Mattila et al., 2012; Lakshminarayanan and Sriraam, 2014). For example, according to the Arrhenius model, as the temperature increases by 10 degrees Celsius, the reliability is reduced by almost 50% (Jiang et al., 2013; Lakshminarayanan and Sriraam, 2014). Therefore, it is very important to transfer heat efficiently from the semiconductor junctions to the ambient environment. Typically, the heat generated in the device moves along the following path: from the semiconductor material to a substrate, to a heat spreader, then to a heat sink and finally to the ambient environment. As one may notice, there are a number of interfaces between different materials along such path.

At the scale of microelectronic devices, where material thickness ranges between a few nanometers to a few hundred microns, interfaces play a very important role in heat propagation (Bar-Cohen et al., 2011; Losego et al., 2012). This is due to the fact that the magnitude of the thermal resistance associated to the interface becomes comparable to the conduction thermal resistance within the material layers. Often, the presence of many interfaces or their poor quality, becomes a bottleneck for heat transfer from the active region to the ambient environment. For this reason, it is essential to accurately characterize interfaces so that they can be well accounted for

during the design phase of microelectronic devices.

## 1.1 Two dimensional (2D) materials

2D materials are a class of nanomaterials consisting of a crystalline structure with a thickness between 1 and 3 atoms. Examples of these materials are graphene, boron nitride (BN), germanium selenide (GeSe) and transition metal dichalcogenides (i.e MoS<sub>2</sub>, WS<sub>2</sub>, MoSe<sub>2</sub>). Their excellent electrical and mechanical properties, ultrathin thickness and very high surface to volume ratio have raised a lot of interest for their use as transistors in flexible electronics (Kim et al., 2015; Fiori et al., 2014; Schwierz et al., 2015). From a heat transfer perspective, heat will be generated by these materials as electric charges move through them. This generated heat must be dissipated in order to avoid excessive temperature rise. Therefore, it is important to understand how heat propagates in these materials and which are the thermal resistances along the heat dissipation path.

The most studied 2D material has been graphene. This material has an extremely high in-plane thermal conductivity of  $\sim 3000$  W/mK at room temperature as a suspended layer (Ghosh et al., 2008; Gu and Yang, 2016), although it drastically reduces down to 600 W/mK when it is supported on a substrate (Seol et al., 2010). From a heat transfer point of view, the most important property is the cross-plane thermal conductivity since this would be the heat propagation direction in a real application. There have only been a few attempts to measure heat transport across graphene, one of them executed with Time Domain Thermoreflectance (Koh et al., 2010) and another one with Frequency Domain Thermoreflectance (Yang et al., 2014). In both cases, they could only measure an effective thermal interface conductance, which includes the cross-plane thermal conductivity of graphene and two other interfaces. In this work, we will perform a similar study on another common 2D material: monolayer

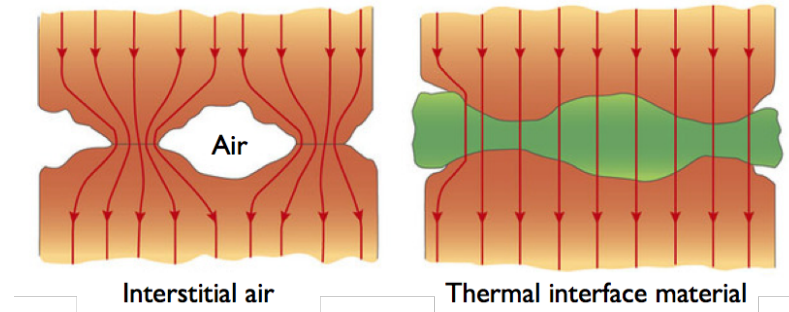


**Figure 1.1:** Thermal interface material (Corporation, 2016)

and few layer  $\text{MoS}_2$ .

## 1.2 Particle enhanced thermal management materials

The contact between two solid surfaces such as that of a central processor unit (CPU) and its heat sink is full of air gaps at the microscopic level due to surface microroughness. Due to the poor thermal conductivity of air ( $0.026 \text{ W/mK}$  at room temperature), this interface presents a large thermal barrier preventing heat transfer from the CPU to the heat sink. In order to avoid this barrier, we can use a thermal interface material (TIM) to fill up the gaps between the two surfaces. Figure 1.1 from (Corporation, 2016) shows a close view of an interface between two solid surfaces and how a TIM would fill in all air gaps to improve heat transfer across the interface. Ideally, the TIM should have a very high thermal conductivity to transfer heat efficiently and mechanical compliance to conform well to both mating surfaces and leave no air gaps. In order to satisfy these requirements, most of the TIMs consist of a polymer matrix filled with thermally conductive particles (Prasher, 2006)(Chung, 2001b).

Similarly, heat sinks are made out of composite materials to satisfy mechanical and thermal requirements. Typical heat sink configurations include tungsten (W), molybdenum (Mo), silicon carbide (SiC) and diamond particles embedded in copper (Cu) or aluminum (Al) (Kidalov and Shakhov, 2009; Abyzov et al., 2012; Jiang et al.,

2013). The particle size usually ranges between 1 and 30  $\mu\text{m}$  and the volume fraction is very high, often above 75%. The particles mostly provide a low coefficient of thermal expansion (CTE) to match that of semiconductors (although in the case of diamond they could also enhance the thermal conductivity) and the matrix provides a high thermal conductivity. Both in TIMs and heat sinks, the particle-matrix interface plays a very important role in the effective thermal conductivity of the composite material (Chu et al., 2010; Xu and Chung, 2000). We characterize this interface by a thermal interface conductance. The thermal interface conductance,  $G$ , is defined as,

$$q = G\Delta T \quad (1.1)$$

where  $q$  is the heat flux across the interface and  $\Delta T$  is the temperature drop across the interface.

Figure 1.2 shows the effective thermal conductivity of a diamond-aluminum composite for different values of the thermal interface conductance ( $G$ ) between the diamond particles and the matrix. These curves were calculated using the Bruggeman model (Pietrak and Winiewski, 2015; Every et al., 1992) for diamond particles of 30  $\mu\text{m}$  size in diameter embedded in an aluminum matrix. We can see how a low interface conductance, caused for instance by poor interfacial bonding, yields a thermal conductivity lower than the aluminum matrix. Therefore, it is very important to study this particle-matrix interface.

### 1.3 Thesis outline

Chapter 2 is a description of the technique used here to carry out all the thermal property measurements. This is an optical pump-probe technique called frequency domain thermoreflectance (FDTR). In principle, the technique is applied to a point on the sample surface and will measure the thermal properties within a small area

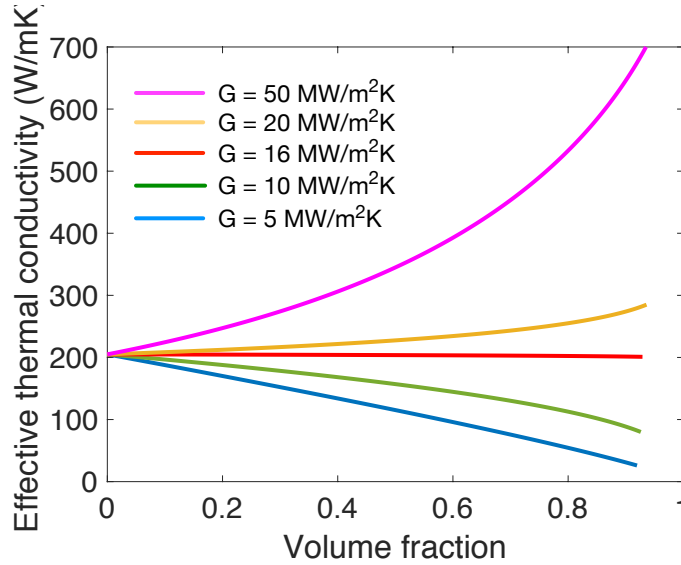


**Figure 1-2:** Effective thermal conductivity of a diamond-aluminum composite for different values of the thermal interface conductance ( $G$ ) between the particles and the matrix. Calculations according to the Bruggeman model (Pietrak and Winiewski, 2015; Every et al., 1992) for a diamond particle size of  $30 \mu\text{m}$  diameter and an aluminum matrix.

(i.e round spot  $3.3 \mu\text{m}$  in diameter). However, by raster scanning the sample and performing a measurement at multiple points, we can obtain thermal property images for any sample. This can be very useful in the case of heterogeneous samples such as composite materials. In this chapter we show multiple thermal conductivity images or maps of several composite samples used a die attach materials.

Chapter 3 presents cross thermal transport measurements on exfoliated monolayer and few layer  $\text{MoS}_2$  samples.  $\text{MoS}_2$  is a 2D material that has attracted attention as a semiconductor due to its large direct bandgap. We deposited  $\text{MoS}_2$  layers on  $\text{SiO}_2$  and Muscovite mica substrates. The number of layers ranged between 1 and 5. We observed higher heat transport across monolayer over few layer  $\text{MoS}_2$ . In addition to measuring heat transport across  $\text{MoS}_2$ , we measured the anisotropic thermal conductivity of bulk  $\text{MoS}_2$  and mica.

Chapter 4 presents a new application for FDTR. FDTR has been typically applied

to layered samples but here we explore the application to micron scale particles. In addition to measuring the thermal conductivity of individual particles, we were able to measure the particles' volume. We developed a new thermal model to extract these properties. We tested the technique with natural diamond and doped silicon particles of multiple sizes ranging between 10 and 60  $\mu\text{m}$  in diameter.

Chapter 5 is an expansion of the previous chapter. Since in real applications the micron scale particles measured before are embedded in a matrix material, we explored the measurements of heat transport across the particle-matrix interface. We found that the sensitivity of the measurement depended on the matrix material thermal conductivity, the particle size and the quality of the interface. In general, high thermal conductivity matrix materials and small particles present higher sensitivity to the measurement of the thermal interface conductance at the particle-matrix interface. We developed a numerical thermal model for this sample configuration and we tested it with diamond micro particles embedded in tin.

Chapter 6 summarizes the work presented in this thesis and explains the main conclusions.

## Chapter 2

# Frequency Domain Thermoreflectance (FDTR)

Frequency domain thermoreflectance (FDTR) is an optical pump-probe technique used to measure material thermal properties at the micro and nano scales (Schmidt et al., 2009; Yang et al., 2013). In addition, it can also measure thermal interface conductances between materials. In this technique a periodically modulated continuous wave laser (red pump beam) provides a periodic heat flux input into the sample while a second continuous wave laser (green probe beam) monitors the sample's surface temperature through a proportional change of surface reflectivity. The wavelength of the red pump beam is 785 nm while that of the green probe beam is 532 nm. Figure 2-1a is a schematic of the setup in our lab. The measured variable is the phase lag between the heat flux input and the surface temperature response. The phase is measured for multiple frequencies via a lock-in amplifier. The unknown thermal properties are extracted by fitting the prediction of a thermal model to the measured phase values (see Fig. 2-1c). Typically, the thermal model is the solution to the heat diffusion equation for a multilayer stack of materials, as depicted in Fig. 2-1b. Each layer in the model is characterized by four parameters: the volumetric heat capacity, the in-plane and cross-plane thermal conductivities and the layer thickness. A thermal interface conductance is considered between the layers.

Since FDTR is an optical technique it requires very smooth surfaces allowing only a microroughness under 200 nm so that enough light is reflected back to the

objective. In addition, all samples must be coated with a metal transducer layer for two main reasons: first, to absorb the laser light and transform it into heat; second, to optimize the thermoreflectance coefficient so that we obtain an acceptable signal to noise ratio. In our case, since we use a 532 nm wavelength probe beam, our metal transducer layer is gold. In order to characterize the thermal properties of this layer we always include a fused silica reference sample during each coating run. Also, we measure the thickness of the transducer layer with an atomic force microscope (AFM).

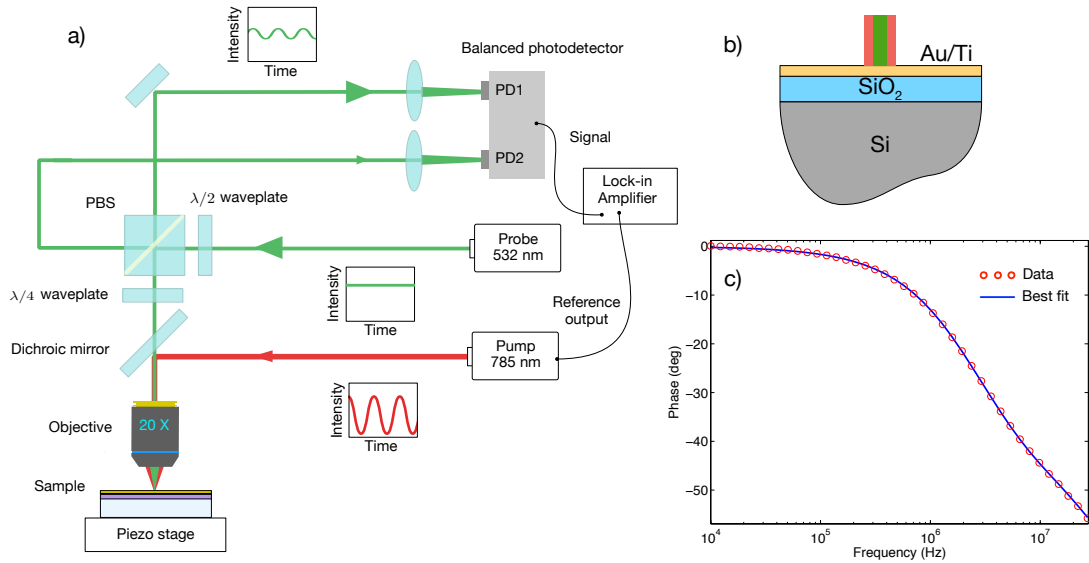


**Figure 2-1:** a) FDTR setup. b) Schematics of a three layer sample used to extract the thermal properties of the  $\text{SiO}_2$  layer. c) FDTR phase data and the thermal model best fit for the sample shown in b).

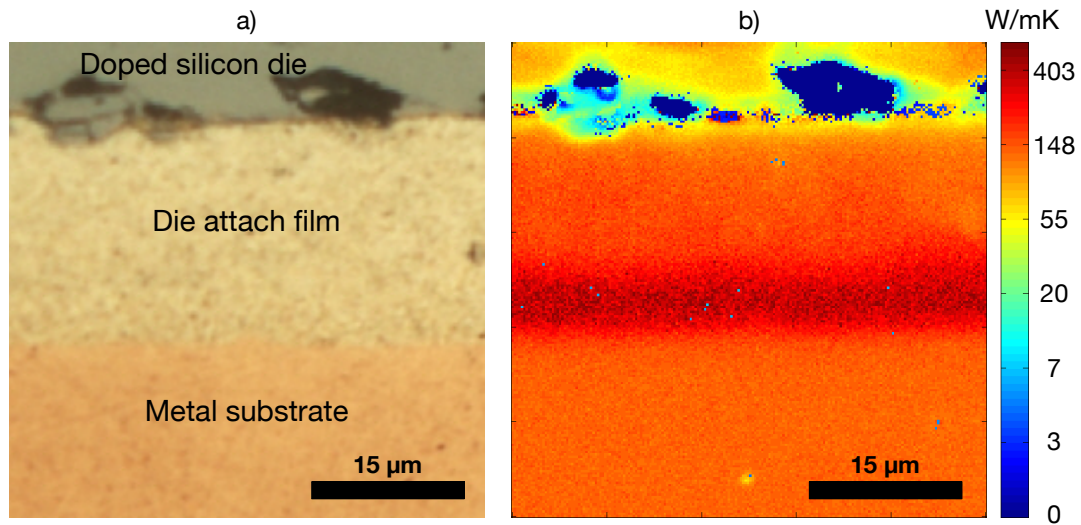
## 2.1 FDTR Imaging

Figure 2-1c shows a thermal property measurement for a specific point on the sample. By raster scanning the sample for multiple points and performing that same measurement at each point, we can form a thermal property image of an area of the sample. Each point where a measurement is performed becomes a pixel in the final thermal property image. This FDTR capability can be very useful to analyze composite mate-

rial samples since we can obtain a high spatial resolution. There are other techniques such as the flash method (Tan et al., 2015; Parker et al., 1961), the transient hotwire technique (Watanabe, 2002) or the transient plane heat source (hot disc) method (Gustavsson et al., 1994) that can measure material thermal conductivity. However, these techniques typically perform the measurement over areas of several  $\text{mm}^2$ , which makes it difficult to pin point micro scale defects or heterogeneities. There has recently been an improvement by Netzsch Nanoflash commercializing a scanning device that can achieve a spatial resolution of 0.1 mm. By using FDTR imaging we can improve this resolution by more than a factor of 30 since our measurement spot size is around 3  $\mu\text{m}$ .

We conducted multiple imaging measurements in some die attach samples provided by our collaborator NAMICS. Die attach are composite materials used to bond components within a microelectronics package. The functions of this material are to absorb mechanical stress caused by temperature gradients and conduct the heat generated in the active region towards the heat sink. For this reason, this composite material is typically made out of a polymeric resin (epoxy, polyimide, polyacrylate) and a metal filler (silver, gold, nickel) (Li and Wong, 2006; Mir and Kumar, 2008). The polymeric resin provides mechanical compliance and the metal filler provides high thermal conductivity. Our collaborator prepared some die attach films consisting of organically modified silicate (OMS) micro particles in silver paste. The die attach films were encased between a doped silicon die and a metal substrate.

Figures 2-2, 2-3 and 2-4 show the thermal conductivity images of the three different samples studied in this work along with an optical image for comparison. The thermal conductivity of the doped silicon die on top of the die attach film was found to be  $110 \pm 12 \text{ W/mK}$ , which is in good agreement with previously reported measurements for this material (Asheghi et al., 2002). All three samples showed a thermal conductivity



**Figure 2-2:** Sample 1 made out of silver powder and metallo-organic silver paste encased between a doped silicon die (top) and a metal substrate (bottom). a) Optical image, 50X objective. b) The thermal conductivity image shows clear silver migration towards the bottom of the die attach film.

gradient in the matrix material. This was due to significant silver migration during the curing process. The maps showed that the thermal conductivity at the bottom of the film is around 420 W/mK, which matches the thermal conductivity of bulk silver (ASM International Staff, 1991). Note how the optical images did not show any signs of this migration but the thermal maps clearly did. In terms of spatial resolution, FDTR imaging provided a resolution close to 3  $\mu\text{m}$  in all thermal conductivity maps presented. The OMS micro spheres in Figures 2-3 and 2-4 as well as the micro scale voids and silver migration in all samples were detected thanks to the high spatial resolution provided by FDTR imaging. This would not have been possible with the conventional techniques mentioned earlier.

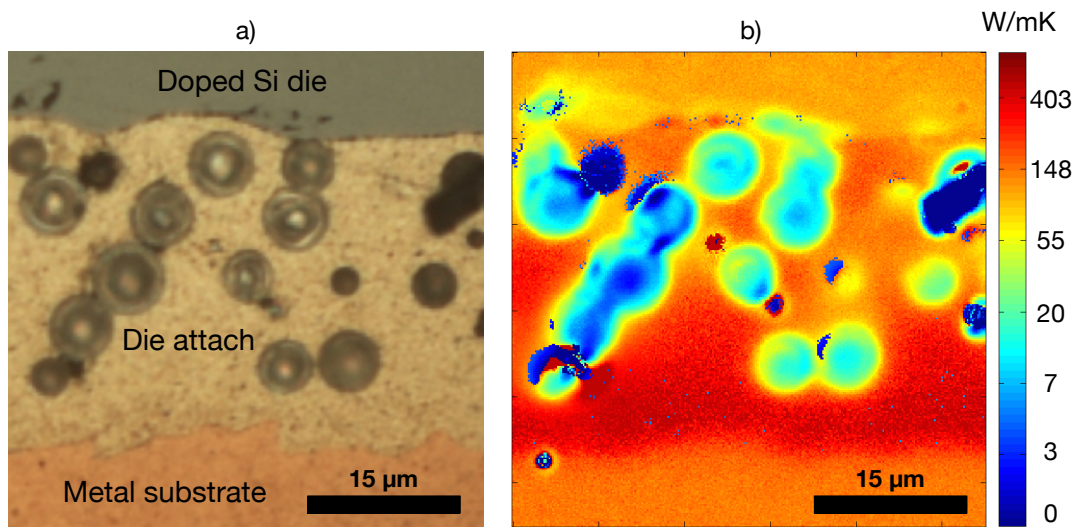


**Figure 2-3:** Sample 2 made out of silver powder, metallo-organic silver paste and OMS particles encased between a doped silicon die (top) and a metal substrate (bottom). a) Optical image, 50X objective. b) The thermal conductivity image shows the OMS micro particles, voids, and silver migration within the matrix.

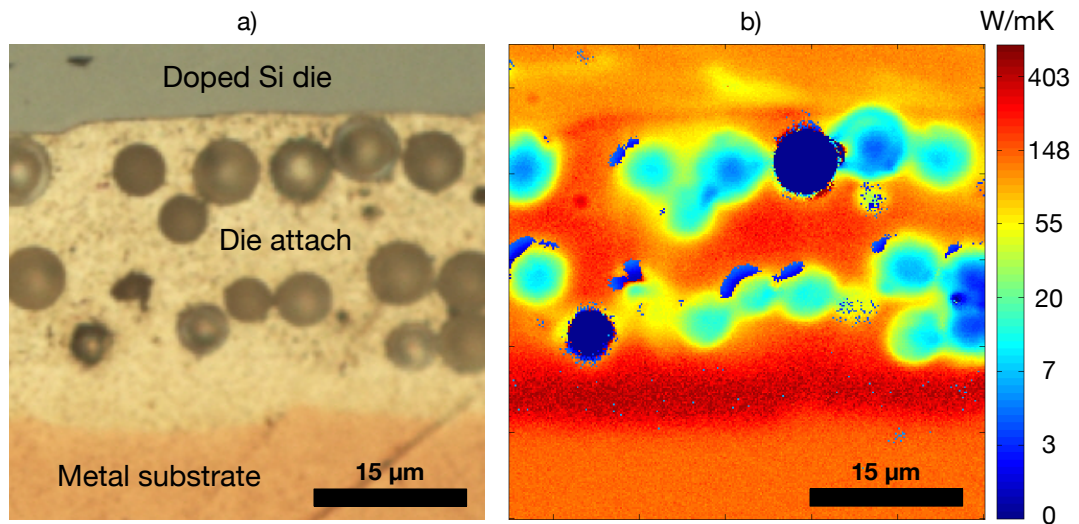


**Figure 2-4:** Sample 3 made out of silver powder, metallo-organic silver paste and OMS particles encased between a doped silicon die (top) and a metal substrate (bottom). a) Optical image, 50X objective. b) The thermal conductivity image shows the OMS micro particles and silver migration within the matrix.

## Chapter 3

# Thermal transport across monolayer and few layer MoS<sub>2</sub>

### 3.1 Introduction

Knowledge of the thermal properties of MoS<sub>2</sub> is important to properly manage heat dissipation in potential electronic device (Wang et al., 2012; Mak et al., 2010) and thermoelectric (Buscema et al., 2013) applications. There have been a number of experimental studies on the in-plane thermal conductivity of suspended (Yan et al., 2014; Sahoo et al., 2013; Zhang et al., 2015) and supported (Zhang et al., 2015; Taube et al., 2015) monolayer and few layer MoS<sub>2</sub>. Raman spectroscopy has been the common technique used in experimental measurements, providing thermal conductivity values between 34.5 and 84 W/mK (Yan et al., 2014; Zhang et al., 2015) for suspended MoS<sub>2</sub> (1 layer) and between 35 and 62 W/mK (Zhang et al., 2015; Taube et al., 2015) for supported MoS<sub>2</sub> (2 and 1 layers respectively). There have only been a few reports of thermal transport in the cross-plane direction for monolayer and few layer MoS<sub>2</sub> (Zhang et al., 2015; Taube et al., 2015). These studies have provided thermal interface conductance values of 1.94 MW/m<sup>2</sup>K for MoS<sub>2</sub> on SiO<sub>2</sub> and 0.44-0.74 MW/m<sup>2</sup>K for MoS<sub>2</sub> on gold. However, there have not been any systematic studies focused on accurately measuring cross-plane heat transport through multilayer MoS<sub>2</sub>, despite the fact that the cross-plane direction is critical in layer structure devices since the largest thermal resistances are found along this way. For instance, in the case of bulk MoS<sub>2</sub>,

the weak van der Waals forces acting between layers contribute to the low thermal conductivity in the cross-plane direction (Liu et al., 2014; Muratore et al., 2014). In addition, for sufficiently thin material layers, the thermal resistances at the interfaces become an important barrier to heat propagation. All these factors make the cross-plane direction the limiting direction for heat transport. In this letter, we provide an experimental investigation in cross-plane thermal transport through monolayer and few layer MoS<sub>2</sub> as well as anisotropic thermal conductivity measurements of bulk MoS<sub>2</sub> and Muscovite mica.

We prepared monolayer and few layer MoS<sub>2</sub> samples on two different substrates: thermally grown SiO<sub>2</sub> on p-type silicon and Muscovite mica. We chose SiO<sub>2</sub> because it is commonly used in MoS<sub>2</sub> transistors where it appears in direct contact with MoS<sub>2</sub> (Wang et al., 2012; Leong et al., 2015; Nipane et al., 2016). We chose mica as the second substrate because of its contrasting properties: atomic flatness and high thermal anisotropy. In addition, it has been shown that mica is a good substrate to grow MoS<sub>2</sub> on due to an excellent lattice matching of the two materials (Ji et al., 2013).

### 3.2 Experimental methods

We prepared MoS<sub>2</sub> samples ranging from 1 to 5 layers on both substrates by mechanical exfoliation (Novoselov et al., 2005). The bulk samples of MoS<sub>2</sub> and Muscovite mica were obtained after cleaving the purchased crystals. From here on all directions contained in the cleavage plane will be called in-plane direction while the direction perpendicular to this plane (*c*-axis) will be called cross-plane direction. The exfoliation on SiO<sub>2</sub> was done right after cleaning the substrate with piranha solution (sulfuric acid and hydrogen peroxide, 3:1) and oxygen plasma ashing. The exfoliation on freshly cleaved mica was done in a dry glove box filled with Argon gas. The water

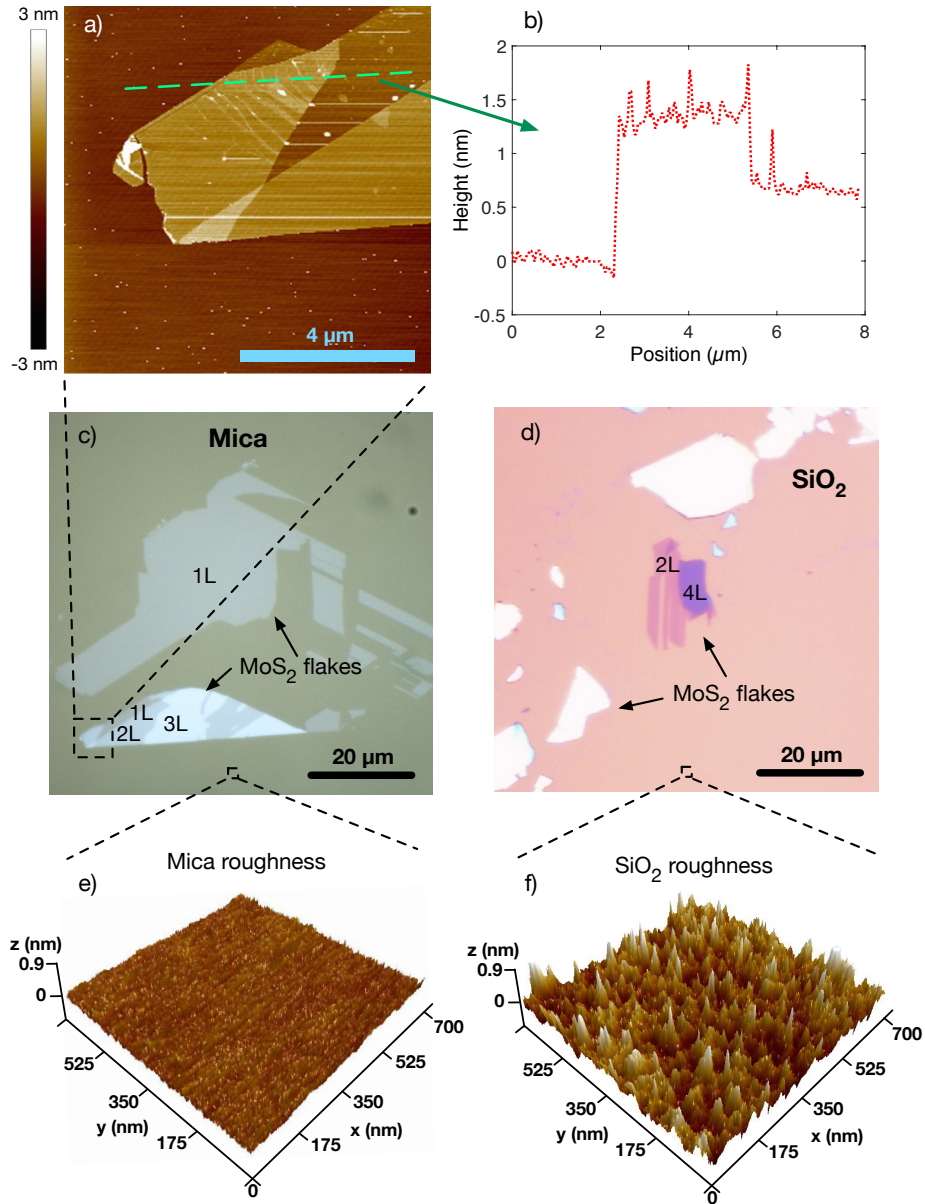


**Figure 3.1:** a) AFM image of an MoS<sub>2</sub> flake on mica. b) Step height analysis on an MoS<sub>2</sub> flake across the dashed white line in the previous AFM image. c) Optical image of MoS<sub>2</sub> flakes on mica. d) Optical image of MoS<sub>2</sub> flakes on SiO<sub>2</sub>. e) AFM roughness measurement of mica ( $R_q = 0.065$  nm,  $R_{max} = 0.63$  nm). f) AFM roughness measurement of SiO<sub>2</sub> ( $R_q = 0.165$  nm,  $R_{max} = 1.51$  nm).

and oxygen level in the glove box during exfoliation were both 0.1 ppm. After exfoliation we used optical contrast and atomic force microscopy (AFM) to characterize all samples. Figure 3.1 illustrates the MoS<sub>2</sub> flake thickness and substrate surface characterization carried out with an optical microscope and AFM. The thickness of the SiO<sub>2</sub> layer was 290 nm to maximize contrast of the number of layers under the optical microscope. A similar optical contrast can also be observed for mica (See Figs. 3.1c and 3.1d). The number of layers for all samples was confirmed by AFM step height measurements as shown in Figs. 3.1a and 3.1b. The thickness measured for an MoS<sub>2</sub> monolayer was  $0.68 \pm 0.02$  nm which is in good agreement with previously reported measurements (Yan et al., 2014; Li et al., 2012a; Yu et al., 2013).

In addition, AFM was used to measure the surface roughness of both substrates. Sample measurements are shown in Figs. 3.1e and 3.1f. The root mean squared roughness,  $R_q$ , was 0.165 and 0.065 nm for SiO<sub>2</sub> and mica respectively. The maximum peak height,  $R_{max}$ , was 1.51 and 0.63 nm for SiO<sub>2</sub> and mica respectively.

Thermal characterization of bulk and few layer MoS<sub>2</sub> as well as bulk mica was conducted through Frequency Domain Thermoreflectance (FDTR) (Schmidt et al., 2009; Yang et al., 2013; Yang et al., 2014). Here a periodically modulated continuous wave laser (pump) is focused to a Gaussian spot of  $3.1 \mu\text{m } 1/e^2$  diameter while a second unmodulated laser monitors the surface temperature. The phase lag between these two signals is recorded with a lock-in amplifier for multiple frequencies. To enable the measurements all samples were coated simultaneously via e-beam evaporation with a metal transducer layer consisting of a 15 nm titanium (Ti) adhesion layer with 60 nm of gold (Au) on top to optimize thermoreflectance. A fused silica reference sample was included in the e-beam evaporation process to later characterize the Au/Ti transducer layer.

In order to extract the unknown thermal properties we fitted the phase data to

a thermal model based on a solution to the heat diffusion equation for a multilayer stack of materials. The thermal model calculates the frequency response of the surface temperature and includes cross-plane and radial transport as well as a thermal interface conductance between the layers. Prior to all measurements, the thermal properties of the Ti/Au transducer layer were obtained by means of the fused silica reference sample. An AFM was used to measure the thickness of this layer ( $75 \pm 2$  nm). The thermal properties of SiO<sub>2</sub> and Si were taken from the literature (Cahill, 1990; Touloukian and Buyco, 1970) as 1.3058 W/mK and 143.35 W/mK for the thermal conductivity and  $1.651 \cdot 10^6$  J/m<sup>3</sup>K and  $1.65 \cdot 10^6$  J/m<sup>3</sup>K for the volumetric heat capacity respectively. For bulk MoS<sub>2</sub> we used a value of  $1.89 \cdot 10^6$  J/m<sup>3</sup>K for the volumetric heat capacity (Kim et al., 2010) while for bulk mica we used a value of  $2.3 \cdot 10^6$  J/m<sup>3</sup>K (Hsieh et al., 2009).

Figure 3.2 shows the final configuration of all measured samples. First, we measured the bulk samples of MoS<sub>2</sub> and mica (Fig. 3.2a). We obtained the anisotropic thermal conductivity of both bulk samples as well as the thermal interface conductance between them and the Au/Ti transducer layer. A total number of at least ten measurements on different locations were taken for each sample. An uncertainty analysis applied to thermoreflectance measurements (Yang et al., 2016) was used to obtain the uncertainty as the  $\pm 1/e$  confidence intervals around the best fit mean values. This uncertainty analysis, which was applied to all measured samples in this letter, accounts for noise, sample variation and uncertainty in the controlled model parameters. The formula used to calculate the uncertainty of multiple unknown parameters is shown in Eq. 3.1.

$$[X_U] = \sqrt{[(J'_U J_U)^{-1} \cdot J'_U([\phi] + J_C[X_C]J'_C)J_U(J'_U J_U)^{-1}]^2 + \sigma_S^2} \quad (3.1)$$

where  $X_U$  is the uncertainty of the unknown parameters,  $J_U$  is the Jacobian ma-

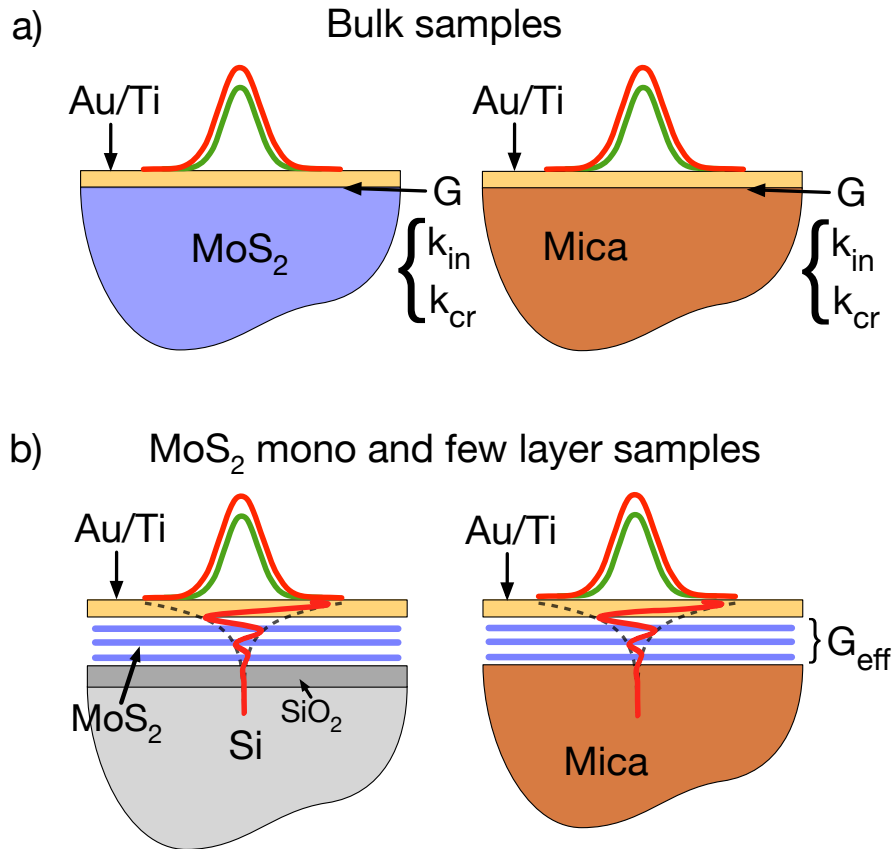


**Figure 3.2:** Schematics of the multilayer models used to extract the thermal properties of mica and MoS<sub>2</sub>. On top, the samples used to obtain the anisotropic thermal conductivity of bulk MoS<sub>2</sub> and mica.  $G$  is the thermal interface conductance,  $k_{in}$  and  $k_{cr}$  are the in-plane and cross-plane thermal conductivity, respectively. On the bottom, the mono and few layer MoS<sub>2</sub> samples on SiO<sub>2</sub> and mica, for which  $G_{eff}$  was measured.

**Table 3.1:** Anisotropic thermal conductivity of bulk MoS<sub>2</sub> and mica and the thermal interface conductance to Au/Ti.  $k_{cr}$  represents cross-plane thermal conductivity,  $k_{in}$  represents in-plane thermal conductivity and  $G$  represents the thermal interface conductance between the transducer layer and the bulk sample.

	$k_{cr}$ (W/mK)	$k_{in}$ (W/mK)	$G$ (MW/m <sup>2</sup> K)
Bulk MoS <sub>2</sub>	$2.2 \pm 0.2$	$91 \pm 4$	$20 \pm 1$
Mica	$0.38 \pm 0.04$	$4.26 \pm 0.45$	$20 \pm 2$

trix of the phase lag with respect to the unknown parameters for each measured frequency,  $J_C$  is the Jacobian matrix of the phase lag with respect to the controlled (known) parameters for each measured frequency,  $\phi$  is a diagonal matrix containing the phase lag noise for each measured frequency,  $X_C$  is a diagonal matrix containing the uncertainty of the controlled parameters for each measured frequency and  $\sigma_S$  is the standard deviation of all measurements taken on a single sample (accounts for sample variation).  $J'_U$  and  $J'_C$  are the transpose matrices of  $J_U$  and  $J_C$ , respectively.

The results of the bulk measurements are shown in Table 3.1 and agree well with previously reported measurements (Liu et al., 2014; Muratore et al., 2014; Gray and Uher, 1977). Figure 3-3 shows an example of FDTR phase data and the best fit curves for the bulk samples measurements. In addition, we plotted the model prediction when we vary the best fit value of the in-plane and cross-plane thermal conductivities by  $\pm 50\%$ . We can clearly see in both cases that the in-plane and cross-plane thermal conductivities are sensitive to different frequency regions. That is why it is possible to fit these two properties simultaneously. Mica shows less sensitivity due to its lower thermal conductivity values.

For the monolayer and few layer MoS<sub>2</sub> samples, we measured two different flakes for each number of layers. Within each flake, we performed a minimum of ten mea-

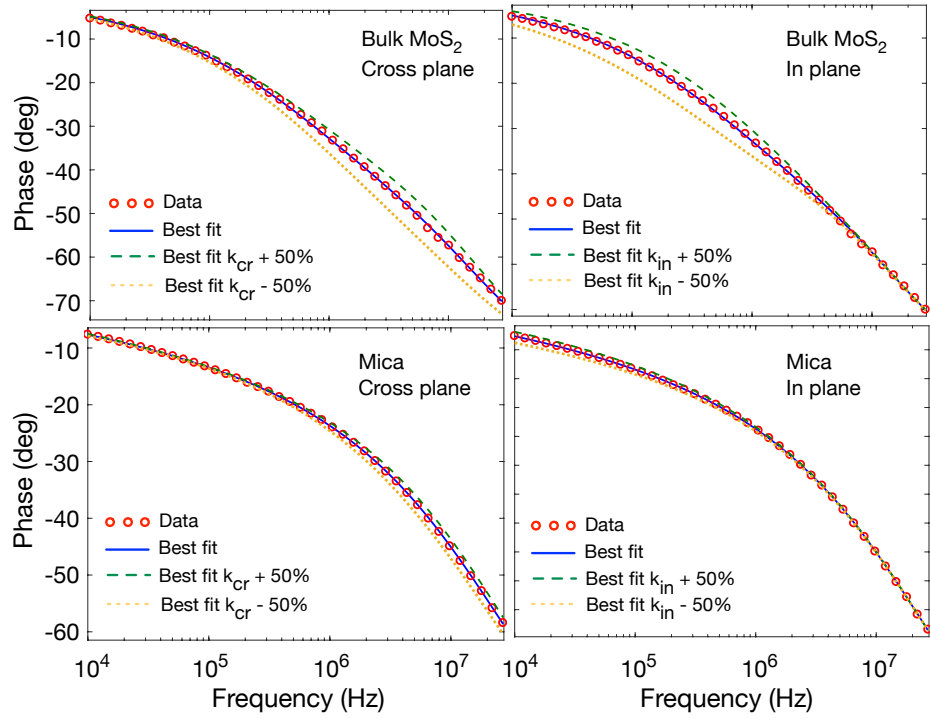


**Figure 3.3:** Top: FDTR data and best model fit for the bulk MoS<sub>2</sub> sample. Bottom: FDTR data and best model fit for the mica substrate. In all cases a model prediction when we vary the fitted values by  $\pm 50\%$  is represented by the dashed lines.

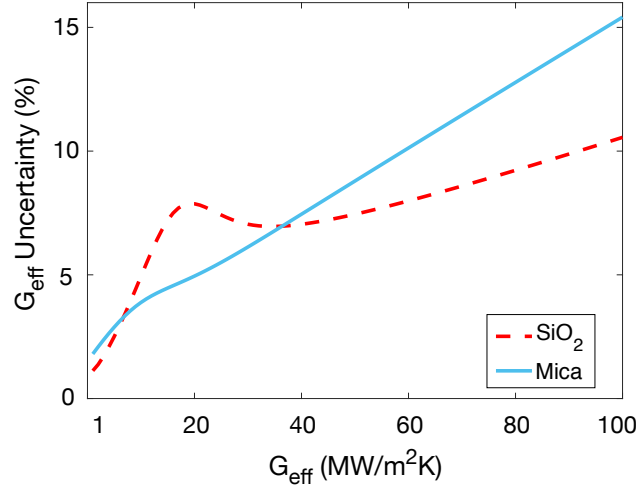


**Figure 3-4:** Uncertainty of  $G_{\text{eff}}$  for a wide range of values. Calculated using Eq. 3.1, it also indicates how sensitive FDTR is to the measurement of  $G_{\text{eff}}$ .

measurements in different locations. We represented thermal transport across MoS<sub>2</sub> by an effective thermal interface conductance,  $G_{\text{eff}}$  (see Fig. 3-2b). This includes the thermal interface conductance between Au/Ti and MoS<sub>2</sub>, the thermal interface conductance between MoS<sub>2</sub> and the substrate, and the cross-plane thermal conductivity of the MoS<sub>2</sub> layer. We neglect the thermal interface conductance between Au and Ti in the transducer layer due to its high value (Gundrum et al., 2005). We can also neglect the heat capacity of the MoS<sub>2</sub> because the time constant of this layer (due to its ultrathin thickness) is on the order of 1.68 GHz, which is a much higher frequency than the ones used for these measurements. For these samples,  $G_{\text{eff}}$  was the only fitted parameter since the rest of the material properties were known. Figure 3-4 shows the uncertainty of this measurement on both substrates according to Eq. 3.1 for a wide range of  $G_{\text{eff}}$  values. Since Eq. 3.1 already contains sensitivity analysis, Fig. 3-4 also provides an idea of how sensitive FDTR is for each value of  $G_{\text{eff}}$ .

### 3.3 Results and discussion

The measured values of the effective thermal interface conductance,  $G_{\text{eff}}$ , of the MoS<sub>2</sub> samples on SiO<sub>2</sub> and mica are summarized in Fig. 3-5. Figure 3-5a shows the full comparison of  $G_{\text{eff}}$  between MoS<sub>2</sub> on SiO<sub>2</sub> and MoS<sub>2</sub> on mica. Figure 3-5b is a zoomed in view of the low  $G_{\text{eff}}$  region in Fig. 3-5a so that the trend and errors of  $G_{\text{eff}}$  on mica can be better appreciated. The zero layer point represents the thermal interface conductance between the Au/Ti layer and the substrates. In the case of SiO<sub>2</sub>, the thermal interface conductance obtained (89 MW/m<sup>2</sup>K) is in good agreement with literature values (Koh et al., 2010). For the case of mica, to the authors best knowledge the thermal interface conductance between Au/Ti and mica has not been measured yet. The value obtained here is about four times lower than that between Au/Ti and SiO<sub>2</sub>. This may be due to a combination of the high thermal anisotropy (Chen et al., 2013) and extremely low cross-plane thermal conductivity of mica. The one layer point shows a very small drop in  $G_{\text{eff}}$  for mica while we see a significant drop for SiO<sub>2</sub>. For both substrates, we see a large drop in  $G_{\text{eff}}$  from the one to the two layer samples, and after two layers,  $G_{\text{eff}}$  decays slowly until it becomes practically constant at the four and five layer samples. The error is larger on the SiO<sub>2</sub> samples due to more variation on different locations of the sample rather than sensitivity to  $G_{\text{eff}}$ .

First, let us consider the four and five layer samples for both substrates. We see in Fig. 3-5b that  $G_{\text{eff}}$  is constant for this number of layers. If we therefore assume that heat transport is dominated by the thermal resistance at the top and bottom interfaces, we can write  $G_{\text{eff}} = (1/G_{\text{top}} + 1/G_{\text{bottom}})^{-1}$ , where  $G_{\text{top}}$  is the thermal interface conductance between Au/Ti and MoS<sub>2</sub> and  $G_{\text{bottom}}$  is the thermal interface conductance between MoS<sub>2</sub> and the substrate. If we further assume  $G_{\text{top}}$  for four or five layers is the same as in the case of bulk MoS<sub>2</sub> (20 MW/m<sup>2</sup>K), then we can

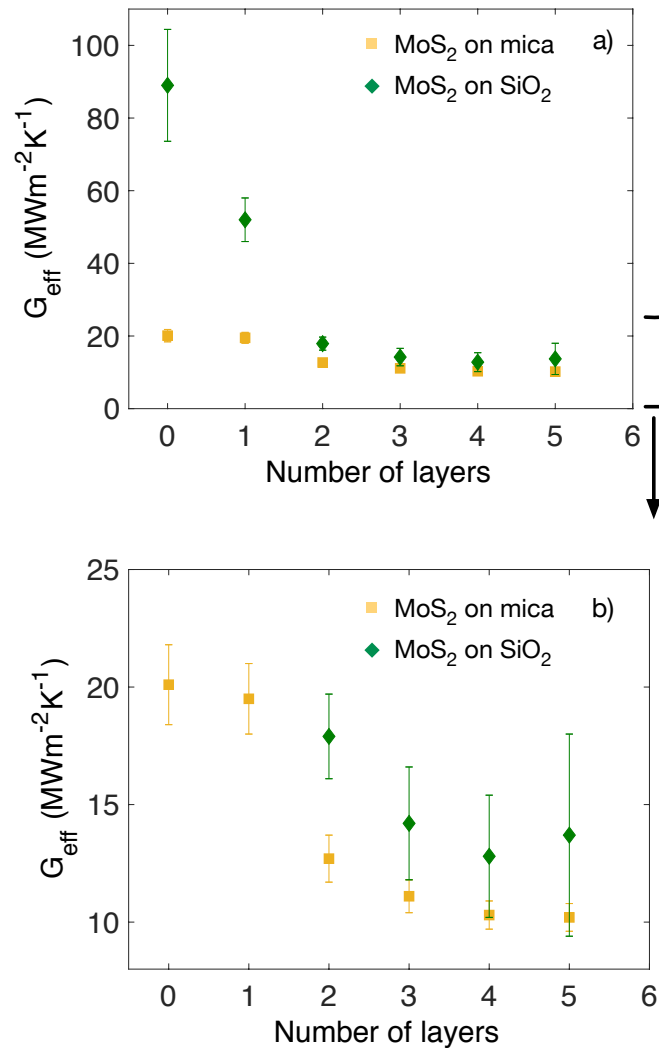


**Figure 3-5:** Effective thermal boundary conductance ( $G_{\text{eff}}$ ) for MoS<sub>2</sub> on SiO<sub>2</sub> and mica. a) shows the full comparison of  $G_{\text{eff}}$  between SiO<sub>2</sub> and mica. Error bars for mica are the size of the symbol. b) is a zoomed in view for  $G_{\text{eff}} < 25$  MW/m<sup>2</sup>K in order to see the trend and error bars.

calculate  $G_{\text{bottom}}$ . This gives a thermal interface conductance of 40 and 21 MW/m<sup>2</sup>K for MoS<sub>2</sub> on SiO<sub>2</sub> and mica respectively. It is important to clarify that these values are conditioned by the assumption that  $G_{\text{top}}$  is the same as in the bulk samples. We believe this is a reasonable assumption only for the four and five layer samples since the surface roughness approaches that of bulk MoS<sub>2</sub> (see Fig. 3-6 and Ref. (Quereda et al., 2014)). The value of the thermal interface conductance for MoS<sub>2</sub> on SiO<sub>2</sub> is about twenty times higher than a previously reported value using Raman spectroscopy, which was 1.94 MW/m<sup>2</sup>K (Taube et al., 2015). Both values are determined by comparing measured data to a diffusion model, but in the case of the Raman technique, the authors assumed that the substrate under the MoS<sub>2</sub> remains constant at the ambient temperature, although the temperature in the substrate increases during the measurement. This could cause a significant error in the extracted value of thermal interface conductance. In our model we solve the heat diffusion equation accounting for anisotropic heat conduction in all layers of the sample. In addition to different models, differences in sample preparation could also contribute to difference in the reported results.

Next we consider the three or fewer layer samples on the mica substrate. We observe a steady increase in  $G_{\text{eff}}$  going from four to two layers and then a significant increasing jump for the one layer sample.  $G_{\text{eff}}$  for one layer is almost the same as the  $G$  between Au/Ti and mica, indicating that almost the same amount of phonons transmits through the MoS<sub>2</sub> monolayer. This is not the case for the bilayer sample, where the drop in  $G_{\text{eff}}$  from one to two layers may be due to phonon scattering at the interface between MoS<sub>2</sub> layers. According to the trend in  $G_{\text{eff}}$  it seems that phonon transmission between MoS<sub>2</sub> layers improves with the number of layers.

Finally, we consider the three or fewer layer samples on the SiO<sub>2</sub> substrate. Here, we observe a slight increase in  $G_{\text{eff}}$  from four to two layers followed by a very large

increase in the one layer sample. In contrast to mica,  $G_{\text{eff}}$  for the one layer sample on  $\text{SiO}_2$  falls in between the interface conductance ( $G$ ) for zero layers and the  $G_{\text{eff}}$  for two layers. One possible cause for this larger drop in  $G_{\text{eff}}$  between the zero and one layer samples may be the surface roughness of  $\text{SiO}_2$ . The AFM measurements presented in Fig. 3-1 show that  $\text{SiO}_2$  has three times the roughness of mica with surface peaks as tall as 1.5 nm, which is approximately the thickness of two  $\text{MoS}_2$  layers. Recent studies have shown how monolayer  $\text{MoS}_2$  partially conforms to  $\text{SiO}_2$  while multiple layer  $\text{MoS}_2$  presents a flat surface similar to that of bulk  $\text{MoS}_2$  or mica (Quereda et al., 2014; Man et al., 2016). Figure 3-6 shows roughness measurements of some of our samples prior to the transducer layer coating. There is a clear decreasing trend in roughness with the number of layers on the  $\text{SiO}_2$  substrate indicating less conformation to  $\text{SiO}_2$  with more layers. In contrast, mica shows less dependency with the number of layers. Therefore, the partial conformation of  $\text{MoS}_2$  to  $\text{SiO}_2$  contributes to the large drop in  $G_{\text{eff}}$  observed between the zero and one layer samples. Then, reduced conformation (worse  $\text{MoS}_2$ - $\text{SiO}_2$  interface) and phonon scattering at the  $\text{MoS}_2$  layers interface contribute to the next drop in  $G_{\text{eff}}$  between the one and two layer samples. Similar to the mica case, the trend in  $G_{\text{eff}}$  suggests that phonon transmission between  $\text{MoS}_2$  layers improves with the number of layers.

We can try quantifying the thermal interface conductance between  $\text{MoS}_2$  layers by treating each  $\text{MoS}_2$  layer as a material layer with a known thickness and known thermal properties, instead of treating them as an interface. Given  $\text{MoS}_2$  2D nature, we can assume a very large cross-plane thermal conductivity and an in-plane thermal conductivity equal to the in-plane thermal conductivity of the bulk sample (91 W/mK). Similarly, we assume a heat capacity of 1.89 MJ/m<sup>3</sup>K for each  $\text{MoS}_2$  layer. Finally, we consider different thermal interface conductances between  $\text{MoS}_2$  layers.

Since the structural configuration of the  $\text{MoS}_2$  layers is not clearly known, two

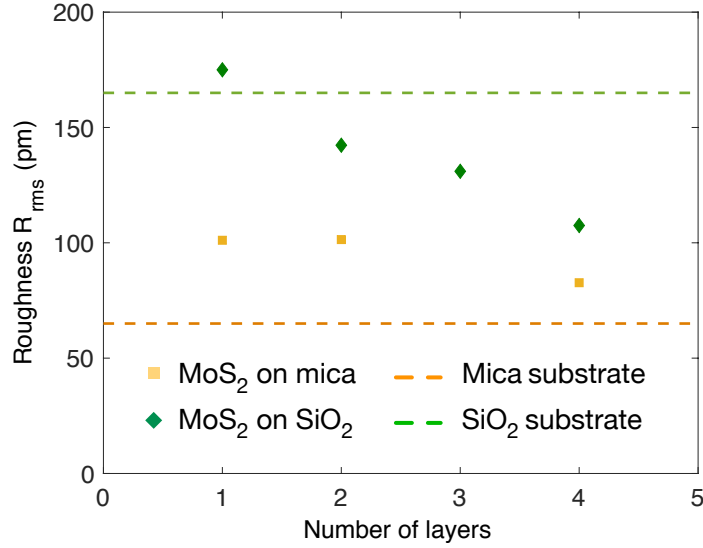


**Figure 3-6:** Roughness measurements of monolayer and few layer MoS<sub>2</sub> samples carried out with AFM. The measurements were done prior to coating with the metal transducer layer. Samples on SiO<sub>2</sub> show a clear decreasing trend while mica sample remain more constant at a low roughness.

hypothesis are considered for this model. We will call them A and B and they are represented in Fig. 3-7. In both cases, monolayer MoS<sub>2</sub> is assumed to conform to the substrate surface profile based on reported roughness measurements (Quereda et al., 2014; Man et al., 2016) as well as on the measurements presented in Fig. 3-6. In contrast, bilayer and few layer MoS<sub>2</sub> show a significant decrease in surface roughness (Quereda et al., 2014; Man et al., 2016). The difference between hypothesis A and B is the behavior of the bottom layer for multiple layer samples. As shown in Fig. 3-7, hypothesis A assumes that for multilayer samples, all layers sit flat on top of the substrate. On the other hand, hypothesis B assumes the first layer always conforms to the substrate regardless of the number of layers on top. In this case, the second MoS<sub>2</sub> layer separates from the first and stays flat.

For both hypothesis, the monolayer samples yield a thermal interface conductance,  $G_S$ , consisting of the following two thermal interface conductances: Au/Ti transducer

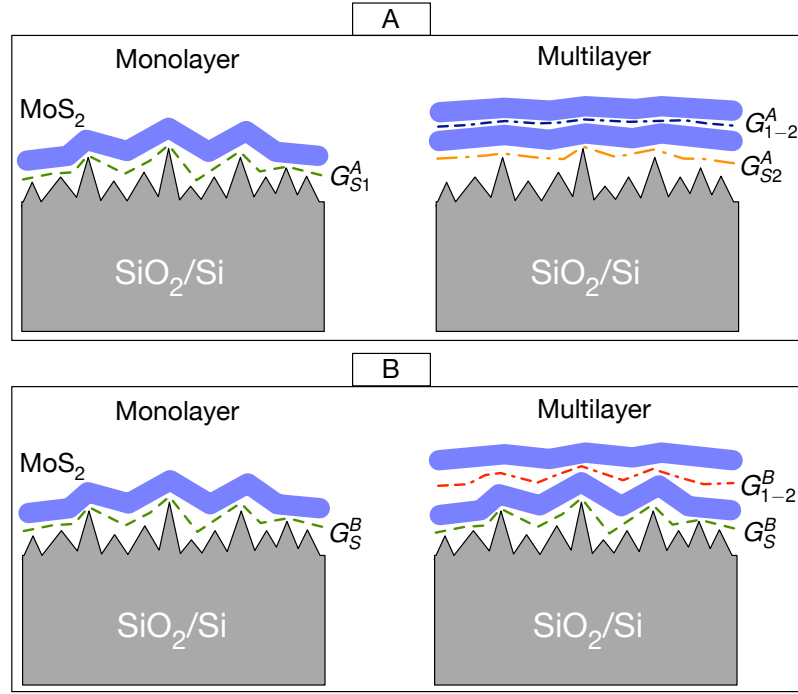


**Figure 3-7:** Hypothesis used in the alternative model. Roughness and MoS<sub>2</sub> dimension are set to scale.

layer - MoS<sub>2</sub> and MoS<sub>2</sub> - substrate. We cannot obtain each of these thermal interface conductances separately because they are strongly correlated and the fitting algorithm cannot distinguish them. We then move onto the bilayer samples. Here we introduce one more thermal interface conductance with respect to the monolayer samples, which is the thermal interface conductance between the two MoS<sub>2</sub> layers. We assume that the thermal interface conductances to the transducer layer and the substrate are represented by  $G_S$  so that we only fit the thermal interface conductance between the MoS<sub>2</sub> layers. Similarly, we proceed in order with the other samples to obtain the rest of the thermal interface conductances between MoS<sub>2</sub> layers. All the results obtained with this model are summarized in Tables 3.2 and 3.3. Here  $G_{i-j}$  represents the thermal interface conductance between the  $i$ -th and  $j$ -th MoS<sub>2</sub> layers. Note how for hypothesis A,  $G_S$  changes from the monolayer to the bilayer sample and it cannot be obtained for the bilayer sample due to its strong correlation with  $G_{1-2}$ . After three

layers of MoS<sub>2</sub> only a lower bound is provided due to a lack of sensitivity. In other words, the lower magnitude interface conductances near the substrate dominate the thermal response.

The results obtained with hypothesis A show that the change between  $G_{S1}$  and  $G_{S2}$  is much larger on the SiO<sub>2</sub> substrate than on mica. This larger change is attributed to the surface roughness of the SiO<sub>2</sub>, which is almost three times the roughness of mica (see Fig. 3·1). Indeed, according to this hypothesis, a larger substrate roughness will imply a larger separation between the MoS<sub>2</sub> and the substrate in multilayer samples. This is detrimental to heat transport across the interface and therefore it leads to a lower thermal interface conductance. According to hypothesis B, there is a very low thermal interface conductance between the first and second MoS<sub>2</sub> layers ( $G_{1-2}$ ) in the SiO<sub>2</sub> case. Similar to hypothesis A, the effect of the substrate roughness on the interlayer separation between the first and second MoS<sub>2</sub> layers is much greater on the SiO<sub>2</sub> case, which yields a much lower thermal interface conductance in comparison to the mica case. In addition, it is interesting to observe an increasing trend on the MoS<sub>2</sub> thermal interface conductances. This is both expected and necessary in order to reach the 2 W/mK of the cross-plane thermal conductivity in bulk MoS<sub>2</sub>. Both hypothesis can explain the measurements provided in Fig. 3·5. In the case of SiO<sub>2</sub>, the large drop in  $G_{\text{eff}}$  between the monolayer and bilayer samples is due to the low magnitude of  $G_{S2}$  (hypothesis A) or  $G_{1-2}$  (hypothesis B). This low thermal interface conductance becomes the dominating factor in the overall thermal response on these samples, which explains the practically constant  $G_{\text{eff}}$  value seen in the multilayer samples. In the case of mica, the lack of a clearly dominating thermal interface conductance provides a smoother decay in  $G_{\text{eff}}$ .

**Table 3.2:** Thermal interface conductance values according to hypothesis A.

Hypothesis A	SiO <sub>2</sub>	Mica
$G_{S1}$ (MW/m <sup>2</sup> K)	$52 \pm 6$	$19.5 \pm 1.5$
$G_{S2}+G_{1-2}$ (MW/m <sup>2</sup> K)	$18 \pm 2$	$13 \pm 1$
$G_{2-3}$ (MW/m <sup>2</sup> K)	$81 \pm 10$	$67 \pm 9$
$G_{>3}$ (MW/m <sup>2</sup> K)	$\geq 81$	$\geq 67$

**Table 3.3:** Thermal interface conductance values according to hypothesis B.

Hypothesis B	SiO <sub>2</sub>	Mica
$G_S$ (MW/m <sup>2</sup> K)	$52 \pm 6$	$19.5 \pm 1.5$
$G_{1-2}$ (MW/m <sup>2</sup> K)	$24 \pm 3$	$40 \pm 5$
$G_{2-3}$ (MW/m <sup>2</sup> K)	$80 \pm 11$	$55 \pm 9$
$G_{>3}$ (MW/m <sup>2</sup> K)	$\geq 80$	$\geq 77$

### 3.4 Conclusions

In conclusion, we investigated cross-plane thermal transport in encased exfoliated monolayer and few layer MoS<sub>2</sub> via FDTR measurements on SiO<sub>2</sub> and mica substrates. In addition, we measured the anisotropic thermal conductivities of bulk MoS<sub>2</sub> and mica with FDTR to confirm previously reported measurements conducted with other techniques (Liu et al., 2014; Gray and Uher, 1977). We represented heat transfer through monolayer and few layer MoS<sub>2</sub> by an effective thermal interface conductance ( $G_{\text{eff}}$ ). We used the samples with the highest number of layers to estimate the thermal interface conductance between MoS<sub>2</sub> and the substrates, assuming the thermal interface conductance between Au/Ti and MoS<sub>2</sub> is the one obtained for the bulk case. The thermal interface conductance values between MoS<sub>2</sub> and the SiO<sub>2</sub> and mica substrates were 40 and 21 MW/m<sup>2</sup>K respectively. We observed a significant improvement in heat transport through monolayer over few layer MoS<sub>2</sub>. For MoS<sub>2</sub> on SiO<sub>2</sub>,  $G_{\text{eff}}$  is over three times better if a monolayer is used. For MoS<sub>2</sub> on mica,  $G_{\text{eff}}$  is approximately two times better for monolayer MoS<sub>2</sub>. This implies that monolayer MoS<sub>2</sub> has superior thermal properties for its use in electronic devices where it is often encased between metals and dielectric materials.

## Chapter 4

# Measuring individual micro particles with FDTR

### 4.1 Introduction

Knowledge of the thermal properties of micron scale particles is important for engineering composite materials widely used in the microelectronics industry. Some examples of these composite materials are die attach materials used to bond different electronic components or advanced heat sinks capable of dissipating the large amounts of heat generated in today's high power devices. Materials used in microelectronics packaging are often required to have high thermal conductivity in order to effectively transfer heat while simultaneously possessing a low coefficient of thermal expansion (CTE) to match that of semiconductor chips (Jiang et al., 2013). To control and optimize these two properties, high thermal conductivity particles can be embedded in metals such as aluminum (Al) and copper (Cu) (Jiang et al., 2013; Chung, 2001a; Abyzov et al., 2012; Davis and Artz, 1995; Molina et al., 2008), or in polymeric materials (Tekce et al., 2007; Xu and Chung, 2000).

Commonly used particle materials are silicon carbide (SiC), tungsten (W), aluminum nitride (AlN) or diamond. The thermal conductivity of these materials can deviate substantially from their bulk counterparts and can vary depending on crystallinity, dopants, and impurities. For example, the thermal conductivity of SiC at room temperature can vary between 100 and 340 W/mK depending on the concentra-

tion of nitrogen (N) or aluminum (Al) and, in the case of polycrystalline SiC, grain size (Slack, 1964; Burgemeister et al., 1979; Collins et al., 1990; Crocombette and Gelebart, 2009). Similarly, the thermal conductivity of diamond at room temperature can vary between 1200 and 2500 W/mK depending on the degree of crystallinity, nitrogen (N) concentration and carbon (C) isotopes concentration (Barman and Srivastava, 2007; Olson et al., 1993; Yamamoto et al., 1997; Ruch et al., 2006; Slack, 1964). When it comes to predicting the effective thermal conductivity of a composite material containing such particles, it would therefore be useful to have accurate thermal conductivity measurements of a representative selection of the individual particles. It would also be useful to measure the thermal interface conductance between the particles and other materials since sometimes these particles are coated to improve mechanical bonding. And for small enough particle sizes, this interface can become an important thermal resistance and have a significant impact on the effective thermal conductivity of the composite material (Pietrak and Winiewski, 2015; Davis and Artz, 1995; Tavangar and Weber, 2012).

In this chapter, we present an optical method based on frequency domain thermoreflectance (FDTR) (Schmidt et al., 2009; Yang et al., 2013) to measure the thermal conductivity of individual micron scale particles. The technique uses one focused laser beam to provide a heat flux into the particle while a second focused beam monitors particle's surface temperature. The surface temperature is compared with a diffusive thermal model to extract the particle's thermal conductivity and other physical properties. We first present the theory of this technique as applied to finite particles and then present our experiments on particles of diamond and silicon with dimensions on the order of 10 – 60  $\mu\text{m}$ .

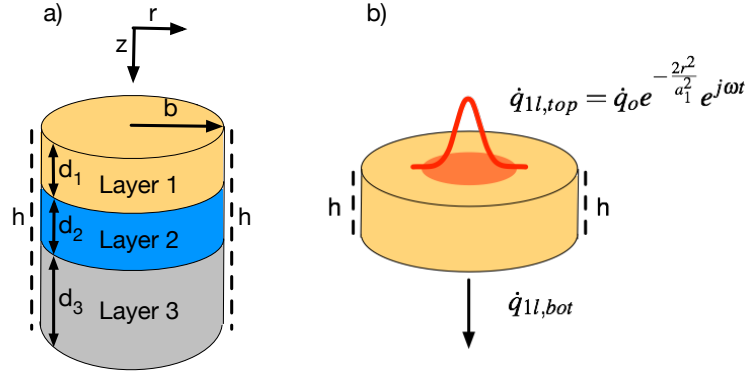


**Figure 4.1:** a) Schematic of finite cylindrical layer model. It includes for an arbitrary number of layers and accounts for thermal interface resistance between layers, as well as a convection boundary on the sides ( $r = b$ ). b) Closer look at the top layer. A Gaussian periodic heat flux is applied to the sample.

## 4.2 Theory

We model the particle as a finite cylinder and add cylindrical layers to account for other materials placed on top and/or under the particle. Figure 4.1a shows the schematics of this cylindrical layer model. The focused laser heat source is modeled as a Gaussian heat flux on the top surface. The model includes a thermal interface conductance between each cylindrical layer and convective heat transfer on the side boundaries, as indicated by  $h$  in Fig. 4.1.

The thermal model presented here only considers diffusive heat transport and shares similarities to the infinite layer model typically used for the time- and frequency-domain thermoreflectance (FDTR) techniques (Schmidt et al., 2009; Yang et al., 2013). A periodically modulated continuous wave laser (pump) is focused to a Gaussian spot to provide the heat flux while a second unmodulated laser (probe) monitors the surface temperature. The phase lag,  $\phi$ , between these two signals is recorded with a lock-in amplifier for multiple frequencies and is compared to the phase lag predicted by the thermal model. The modeled signal from the lock-in amplifier is a complex

number,  $Z(\omega)$ :

$$Z(\omega) = \beta H(\omega) \quad (4.1)$$

where  $\beta$  is a constant and  $H(\omega)$  is the frequency response to the surface temperature of the sample. The constant  $\beta$  is given by

$$\beta = G_{\text{det}} P_{\text{pump}} P_{\text{probe}} (1 - R_{\text{pump}}) R_{\text{probe}} \left( \frac{dR}{dT} \right)_{\text{probe}} \quad (4.2)$$

where  $G_{\text{det}}$  is a constant that encompasses the gain of the photodetector and power reduction from optical components,  $P_{\text{pump}}$ ,  $P_{\text{probe}}$ ,  $R_{\text{pump}}$  and  $R_{\text{probe}}$  are the powers and reflectivities of the pump and probe lasers, respectively, and  $\left( \frac{dR}{dT} \right)_{\text{probe}}$  is the thermoreflectance coefficient at the probe wavelength.  $H(\omega)$  is the frequency response of the particle surface temperature in the diffusion model and is described in the next section.

#### 4.2.1 Model derivation

We start by considering a single layer with a Gaussian periodic heat source on top as shown in Fig. 4-1b. Once a solution for the surface temperature is found, we will extend the analysis to multiple layers. The heat diffusion equation for a single layer is

$$\frac{\partial^2 T}{\partial r^2} + \frac{1}{r} \frac{\partial T}{\partial r} + \frac{\partial^2 T}{\partial z^2} = \frac{1}{\alpha} \frac{\partial T}{\partial t} \quad (4.3)$$

where  $T = T(r, z, t)$  is the temperature field,  $\alpha$  is the material's thermal diffusivity,  $t$  is time and  $r, z$  are the spatial coordinates as shown in 4-1a. The boundary conditions

are given by

$$-k \frac{\partial T}{\partial z} \Big|_{z=0} = \dot{q}_{1l,\text{top}} = P(t) e^{-\frac{2r^2}{a_1^2}} \quad (4.3a)$$

$$-k \frac{\partial T}{\partial z} \Big|_{z=d} = \dot{q}_{1l,\text{bot}} \quad (4.3b)$$

$$k \frac{\partial T}{\partial r} + hT = 0 \Big|_{r=b} \quad (4.3c)$$

where  $k$  is the thermal conductivity,  $d$  is the layer thickness,  $h$  is the convection coefficient on the sides,  $P(t)$  is the total input heat flux as a function of time,  $a_1$  is the  $1/e^2$  laser spot radius, and  $\dot{q}_{1l,\text{bot}}$  is the heat flux at the bottom of the cylindrical layer.

First we apply the Fourier transform,  $F(\omega) = \int_{-\infty}^{\infty} f(t) e^{-j\omega t} dt$ , to the heat equation and boundary conditions and obtain:

$$\frac{\partial^2 \bar{T}}{\partial^2 r} + \frac{1}{r} \frac{\partial \bar{T}}{\partial r} + \frac{\partial^2 \bar{T}}{\partial^2 z} = \frac{1}{\alpha} j\omega \bar{T} \quad (4.4)$$

$$-k \frac{\partial \bar{T}}{\partial z} \Big|_{z=0} = \bar{q}_{1l,\text{top}} \quad (4.4a)$$

$$-k \frac{\partial \bar{T}}{\partial z} \Big|_{z=d} = \bar{q}_{1l,\text{bot}} \quad (4.4b)$$

$$k \frac{\partial \bar{T}}{\partial r} + h\bar{T} = 0 \Big|_{r=b} \quad (4.4c)$$

where  $\bar{T}(r, z, \omega)$  is the Fourier transform of  $T(r, z, t)$ . Likewise with  $\bar{q}$  and  $\dot{q}$ . Next we apply the following Hankel transform:

$$\bar{\bar{T}}(\beta, z, \omega) = \int_0^b r \cdot K_o(\beta, r) \cdot \bar{T}(r, z, \omega) dr \quad (4.5)$$

where  $K_o$  is the set of normalized eigenfunctions that solve the following auxiliary problem:

$$\frac{d^2X}{dr^2} + \frac{1}{r} \frac{dX}{dr} + \beta^2 X = 0 \quad \text{in } 0 \leq r \leq b \quad (4.6a)$$

$$k \frac{dX}{dr} + hX = 0 \quad \text{at } r = b \quad (4.6b)$$

The solution,  $X(r)$ , to this auxiliary problem is the Bessel function of order zero  $J_0(\beta r)$ . Introducing this solution in Eq. 4.6b we can determine parameter  $\beta$ ,

$$k\beta J_1(\beta b) + hJ_0(\beta b) = 0 \quad (4.7)$$

Equation 4.7 has multiple solutions so from here on  $\beta$  becomes  $\beta_m$  where  $m$  indicates the  $m$ -th solution. Therefore, there are also multiple solutions,  $X_m(r) = J_0(\beta_m r)$ , to the auxiliary problem in Eq. 4.6a. This auxiliary problem in Eq. 4.6 is a particular case of a Sturm-Liouville problem (Arfken et al., 2013) with a weight function  $w(r) = r$ . In a Sturm-Liouville problem,  $X_m(r)$  are called the eigenfunctions and they are each associated to an eigenvalue  $\beta_m^2$ . For a boundary condition like the one in Eq. 4.6b, the eigenfunctions  $X_m(r)$  become orthogonal with respect to the weight function  $w(r) = r$  (see (Arfken et al., 2013)). Therefore, we have,

$$\int_0^b r X_m(r) X_n(r) dr = \begin{cases} 0 & \text{for } m \neq n \\ \text{number} & \text{for } m = n \end{cases} \quad (4.8)$$

Since we have a set of orthogonal eigenfunctions we can express an arbitrary function  $F(r)$  in the form,

$$F(r) = \sum_{m=1}^{\infty} c_m X_m(r) \quad (4.9)$$

where  $c_m$  are real number coefficients. By using the orthogonality of the  $X_m$  eigenfunctions, we can write,

$$\int_0^b r X_m(r) F(r) dr = \int_0^b r X_m(r) [c_1 X_1 + c_2 X_2 + \dots + c_m X_m + \dots + c_\infty X_\infty] dr = c_m N \quad (4.10)$$

where  $N$  is the norm and it is given by,

$$N = \int_0^b r X_m^2(r) dr \quad (4.11)$$

From Eq. 4.10 we have that,

$$c_m = \frac{1}{N} \int_0^b r X_m(r) F(r) dr \quad (4.12)$$

Substituting  $c_m$  in Eq. 4.9 yields,

$$F(r) = \sum_{m=1}^{\infty} \frac{X_m(r)}{\sqrt{N}} \int_0^b r' \frac{X_m(r')}{\sqrt{N}} F(r') dr' \quad (4.13)$$

If we now define  $K_o(\beta_m, r) = X_m/\sqrt{N}$ , we can quickly observe how Eq. 4.13 represents the inversion formula to the Hankel transform previously defined in Eq. 4.5. Applying this result to our temperature function, the inversion formula for the Hankel transform in Eq. 4.5 takes the form,

$$\bar{T}(r, z, \omega) = \sum_{m=1}^{\infty} K_o(\beta_m, r) \cdot \bar{\bar{T}}(\beta_m, z, \omega) \quad (4.14)$$

Finally, calculating the norm,  $N$ , for  $X_m(r) = J_0(\beta_m r)$  we obtain an expression for  $K_o(\beta_m, r)$  (Ozisik, 2013).

$$K_o(\beta_m, r) = \frac{\sqrt{2}}{b} \frac{\beta_m}{\sqrt{\left(\frac{h}{k}\right)^2 + \beta_m^2}} \frac{J_0(\beta_m r)}{J_0(\beta_m b)} \quad (4.15)$$

Applying the Hankel transform defined in Eq. 4.5 to the left hand side of Eq. 4.4 and using Green's theorem, we have

$$\int_0^b r K_o(\beta_m, r) \left[ \frac{\partial^2 \bar{T}}{\partial r^2} + \frac{1}{r} \frac{\partial \bar{T}}{\partial r} \right] dr = \int_0^b r \bar{T} \left[ \frac{\partial^2 K_o}{\partial r^2} + \frac{1}{r} \frac{\partial K_o}{\partial r} \right] dr + \int_S \left[ K_o \frac{\partial \bar{T}}{\partial r} - \bar{T} \frac{\partial K_o}{\partial r} \right] dS \quad (4.16)$$

where  $S$  is the surface of the cylinder at  $r = b$ . By definition,

$$\frac{\partial^2 K_o}{\partial r^2} + \frac{1}{r} \frac{\partial K_o}{\partial r} = -\beta_m^2 K_o \quad (4.17a)$$

$$k \frac{\partial K_o}{\partial r} + h K_o = 0 \rightarrow h = -k \frac{\partial K_o}{\partial r} \frac{1}{K_o} \quad (4.17b)$$

Substituting  $h$  from Eq. 4.17b into Eq. 4.4c,

$$k \frac{\partial \bar{T}}{\partial r} + h \bar{T} = 0 \rightarrow K_o \frac{\partial \bar{T}}{\partial r} - \bar{T} \frac{\partial K_o}{\partial r} = 0 \quad (4.18)$$

Implementing these results in Eq. 4.16 we get,

$$\int_0^b r K_o(\beta_m, r) \left[ \frac{\partial^2 \bar{T}}{\partial r^2} + \frac{1}{r} \frac{\partial \bar{T}}{\partial r} \right] dr = \int_0^b -r \bar{T} \beta_m^2 K_o(\beta_m, r) dr = -\beta_m^2 \bar{\bar{T}}(\beta_m, z, \omega) \quad (4.19)$$

Thus, the heat diffusion equation (Eq. 4.3) becomes,

$$\frac{\partial^2 \bar{\bar{T}}}{\partial z^2} - (\beta_m^2 + \frac{j\omega}{\alpha}) \bar{\bar{T}} = 0 \quad (4.20)$$

where we define  $\lambda_m = \sqrt{\beta_m^2 + \frac{j\omega}{\alpha}}$ .

Equation. 4.20 has the same form as the transformed heat diffusion equation used to solve the case of a multilayer stack of materials (Schmidt et al., 2009). The only difference is the parameter  $\lambda$ . In the case of the multilayer stack analyzed in

Ref. (Schmidt et al., 2009),  $\lambda$  is given by  $\lambda = \sqrt{\frac{j\omega}{\alpha}}$ . Solving Eq. 4.20 and focusing on the top and bottom surfaces, Schmidt et al. (Schmidt et al., 2009) showed that each layer is characterized by a matrix  $M$  as,

$$\begin{bmatrix} \bar{\bar{T}}_{l,\text{bot}} \\ \bar{\bar{q}}_{l,\text{bot}} \end{bmatrix} = [M] \begin{bmatrix} \bar{\bar{T}}_{l,\text{top}} \\ \bar{\bar{q}}_{l,\text{top}} \end{bmatrix} = \begin{bmatrix} \cosh \lambda d & -\frac{1}{k\lambda} \sinh \lambda d \\ -k\lambda \sinh \lambda d & \cosh \lambda d \end{bmatrix} \begin{bmatrix} \bar{\bar{T}}_{l,\text{top}} \\ \bar{\bar{q}}_{l,\text{top}} \end{bmatrix} \quad (4.21)$$

where  $\lambda = \sqrt{\frac{j\omega}{\alpha}}$  and  $\bar{\bar{T}}_l$  and  $\bar{\bar{q}}_l$  represent the temperature and heat flux at the bottom (bot) and top (top) of a single layer, respectively. In the case of the cylindrical layer model,  $\lambda$  becomes  $\lambda_m = \sqrt{\beta_m^2 + \frac{j\omega}{\alpha}}$ . For a given number of layers,  $n$ , we extend Eq. 4.21 by multiplying the layer matrices as follows,

$$\begin{bmatrix} \bar{\bar{T}}_{\text{bot}} \\ \bar{\bar{q}}_{\text{bot}} \end{bmatrix} = M_n \cdots M_2 M_1 \begin{bmatrix} \bar{\bar{T}}_{\text{top}} \\ \bar{\bar{q}}_{\text{top}} \end{bmatrix} = \begin{bmatrix} A & B \\ C & D \end{bmatrix} \begin{bmatrix} \bar{\bar{T}}_{\text{top}} \\ \bar{\bar{q}}_{\text{top}} \end{bmatrix} \quad (4.22)$$

where 1 is the top layer receiving heat flux,  $n$  is the bottom layer,  $\bar{\bar{T}}$  and  $\bar{\bar{q}}$  represent temperature and heat flux at the bottom (bot) and top (top) surfaces of the layer stack, respectively. This relationship also applies to our cylindrical layer stack. Assuming  $\bar{\bar{q}}_{\text{bot}} = 0$  in Eq. 4.22, a direct relationship between the surface temperature,  $\bar{\bar{T}}_{\text{top}}$ , and the input heat flux,  $\bar{\bar{q}}_{\text{top}}$ , can be obtained:

$$\bar{\bar{T}}_{\text{top}} = -\frac{D}{C} \bar{\bar{q}}_{\text{top}} \quad (4.23)$$

where  $D$  and  $C$  are the elements of the second row of the resulting matrix after multiplying all layer matrices. We now need to obtain the final transform of the Gaussian periodic heat flux ( $\dot{q}_{1l,\text{top}}$ ) introduced in Eq. 4.3a. Applying the previously defined Fourier and Hankel transforms to  $\dot{q}_{1l,\text{top}}$  we get,

$$\bar{\bar{q}}_{1l,\text{top}} = \bar{\bar{q}}_{\text{top}}(\beta_m, \omega) = \bar{P}(\omega) \int_0^b r K_0(\beta_m, r) e^{-\frac{2r^2}{a_1^2}} dr \quad (4.24)$$

Thus, using Eq. 4.23 the temperature at the surface in the transformed space is given by

$$\bar{T}_{\text{top}}(\beta_m, \omega) = -\frac{D}{C} \bar{P}(\omega) \int_0^b r K_o(\beta_m, r) e^{-\frac{2r^2}{a_1^2}} dr \quad (4.25)$$

In order to go back to  $r$  space we apply the inversion formula (Eq. 4.14) and we obtain

$$\bar{T}_{\text{top}}(r, \omega) = \sum_{m=1}^{\infty} K_o(\beta_m, r) \cdot \left(-\frac{D}{C}\right) \bar{P}(\omega) \int_0^b r K_o(\beta_m, r) e^{-\frac{2r^2}{a_1^2}} dr \quad (4.26)$$

Finally we add the effect of the probe beam intensity distribution on the measured signal. The measured surface temperature is an average of the surface temperature distribution weighted by the intensity distribution of the probe beam. Similar to the pump beam, the probe also has a Gaussian spot with  $a_2$  being the  $1/e^2$  radius. Consequently, the final expression for the surface temperature is,

$$\begin{aligned} \bar{T}_{\text{total}}(\omega) &= \int_0^{\infty} \frac{2}{\pi a_2^2} e^{-\frac{2r^2}{a_2^2}} 2\pi r \bar{T}_{\text{top}}(r, \omega) dr = \\ &= \int_0^{\infty} \frac{2}{\pi a_2^2} e^{-\frac{2r^2}{a_2^2}} 2\pi r dr \cdot \sum_{m=1}^{\infty} K_o(\beta_m, r) \cdot \left(-\frac{D}{C}\right) \bar{P}(\omega) \int_0^b r K_o(\beta_m, r) e^{-\frac{2r^2}{a_1^2}} dr = \quad (4.27) \\ &= \sum_{m=1}^{\infty} \frac{\sqrt{2}}{b} \frac{\beta_m}{\sqrt{\left(\frac{h}{k}\right)^2 + \beta_m^2}} \frac{1}{J_0(\beta_m b)} \left(-\frac{D}{C}\right) e^{-\frac{\beta_m^2 a_2^2}{8}} \bar{P}(\omega) \int_0^b r K_o(\beta_m, r) e^{-\frac{2r^2}{a_1^2}} dr \end{aligned}$$

The sample frequency response,  $H(\omega)$ , which goes in Eq. 4.1, is given by  $H(\omega) = \bar{T}_{\text{total}}(\omega)/\bar{P}(\omega)$ . The thermal model  $Z(\omega)$  defined in Eq. 4.1 is a complex number. The phase,  $\phi$ , of this complex number represents the phase lag between the sample surface temperature and the input heat flux. In other words,  $\phi$  is the phase lag between the probe and pump laser, which is what we record with the lock in amplifier. Thus, we

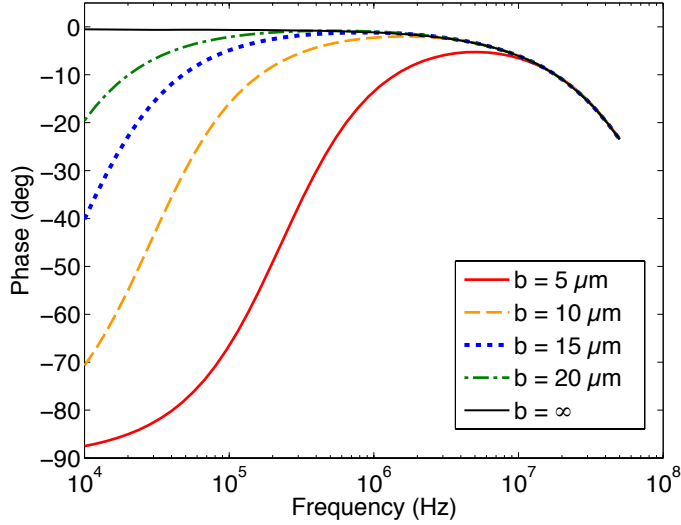


**Figure 4.2:** Model prediction of the phase lag,  $\phi$ , for particles with different sizes and for infinitely wide layers.

will compare the lock in recorded phase to the phase predicted by the model  $Z(\omega)$  in order to extract the unknown properties of our samples.

We can plot the frequency response of the phase,  $\phi$ , for different particle sizes and compare them to the case in which the cylindrical layers have an infinite radius (model in Ref. (Schmidt et al., 2009)). This is shown in Fig. 4.2. Convection losses are neglected in this figure. The curves' peaks represent the frequency at which heat reaches the particle boundary ( $r = b$ ). They drift towards the lower frequencies as the particle radius increases. The bigger the particle the lower the frequency at which the thermal wave reaches the lateral boundary since heat needs more time to travel further. On the other end, for sufficiently high frequencies all curves present the same phase lag. This is because at high frequencies the input heat never reaches the boundaries and therefore the particle behaves as an infinitely wide medium, as shown in Fig. 4.2. Also, the fact that all curves superimpose at high frequencies indicates the model was derived correctly.

### 4.3 Experimental methods

In order to test the model, we prepared several samples with diamond and silicon particles. The diamond particles were purchased from Advanced Abrasives corporation under the category of natural diamond powder in four different sizes: 10, 20, 30 and 50  $\mu\text{m}$  nominal average diameter. The silicon particles were obtained by crushing a piece of a silicon wafer. This silicon wafer was purchased from University Wafer. Particle size for silicon ranged from 30 to 100  $\mu\text{m}$  in diameter. The silicon wafer (ID 783) was P type, doped with boron (B). The doping level was between  $1.34 \times 10^{15}$  and  $1.46 \times 10^{16} \text{ cm}^{-3}$ . Part of this wafer was also used to measure its bulk thermal conductivity. Figures 4-3a and 4-4a show SEM images of several diamond and silicon particles. Most particles presented flat regions that enabled our measurements when positioned on the right orientation. We used a micropipette to spread the particles on 10x10 mm silicon chips so that every particle was sitting directly on top of the chip. To enable the FDTR measurements, all particles were coated with a metal transducer layer. In the case of diamond, it consisted of a 5 nm titanium (Ti) adhesion layer with 95 nm of gold (Au) on top to optimize thermorefectance. Prior to the coating, the diamond particles underwent a plasma ashing treatment with oxygen to form a layer of oxygen terminations on the diamond's surface and therefore improve heat transfer from the transducer layer into the diamond (Collins et al., 2010). In the case of silicon, the transducer layer did not require an adhesion layer and therefore it consisted of 100 nm of gold (Au). A fused silica reference sample was coated during each run to later obtain the thermal properties of the metal transducer layer. We chose the Gaussian laser spot sizes of the pump and probe lasers to be 3.3  $\mu\text{m}$  and 2.6  $\mu\text{m}$  in  $1/e^2$  diameter respectively so that we could fully focus them on the 10  $\mu\text{m}$  size particles. For particles smaller than 10  $\mu\text{m}$ , it was difficult to find regions large enough to fit the laser beams inside.

We used FDTR imaging (Yang et al., 2014) to find particles in the right orientation to reflect the laser beam back to the objective. Figures 4.3b and 4.4b each show an image that accounts for the signal amplitude reflected off a sample with multiple diamond and silicon particles, respectively. Most of the particles showed zero signal amplitude because their surface was not perpendicular to the laser beams and hence they deflected the beam away from the objective. However, some particles presented regions with the right orientation and here is where we performed our measurements. Figure 4.3c shows a zoomed view of one of the diamond particles along with the spot where the lasers were focused. At this point we performed the measurement of the phase for multiple frequencies, as shown in Figs. 4.3d and 4.4c. The frequency range used to carry out the particle measurements was 100 kHz - 50 MHz, except for the silicon particles and 50  $\mu\text{m}$  diamond particles, which was extended to 10 kHz - 50 MHz to adjust to the large size and capture enough points when heat has reached the boundaries. The lower bound had to be low enough to have sensitivity to all particle properties (including size) while avoiding excessive heating on the particle. The upper bound was limited by our lock-in amplifier.

### 4.3.1 Particles modeling

We represented the coated particles by two cylindrical layers. Layer 1 consisted of the metal transducer layer, for which all properties were known by means of the reference sample. Layer 2 consisted of diamond or silicon. A thermal interface conductance was also considered between the two layers. We did not include the substrate on which the particles rest as a third layer in the model because the thermal interface conductance between the particles and the substrate,  $G_{\text{sub}}$ , was very low. Figure 4.5 shows the phase response for different  $G_{\text{sub}}$  values applied to a 10  $\mu\text{m}$  size diamond particle. We found that  $G_{\text{sub}}$  was approximately 0.1 MW/m<sup>2</sup>K. For this value or under, all substrate properties did not have any effect in the phase response at the

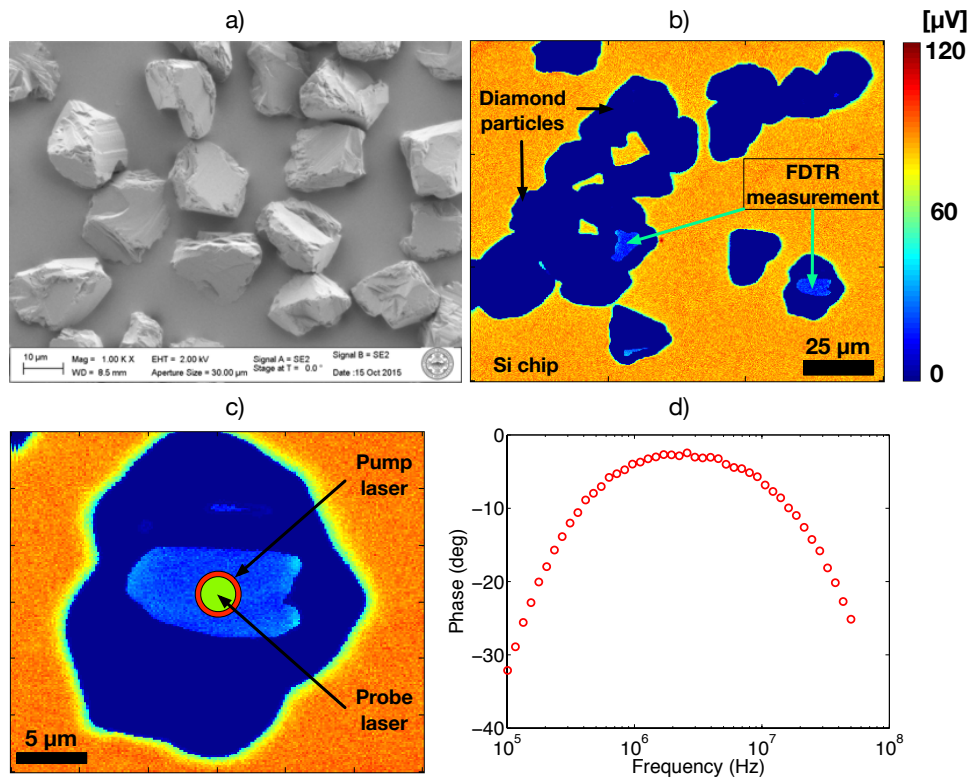


**Figure 4-3:** a) SEM image of several natural diamond particles of the 20  $\mu\text{m}$  size. b) FDTR image of several diamond particles. Some particles present a region oriented perpendicular to the laser beams where it is possible to carry out the measurement. c) Zoomed view of a diamond particle and the spot where the lasers were focused. d) FDTR phase data acquired for multiple frequencies.

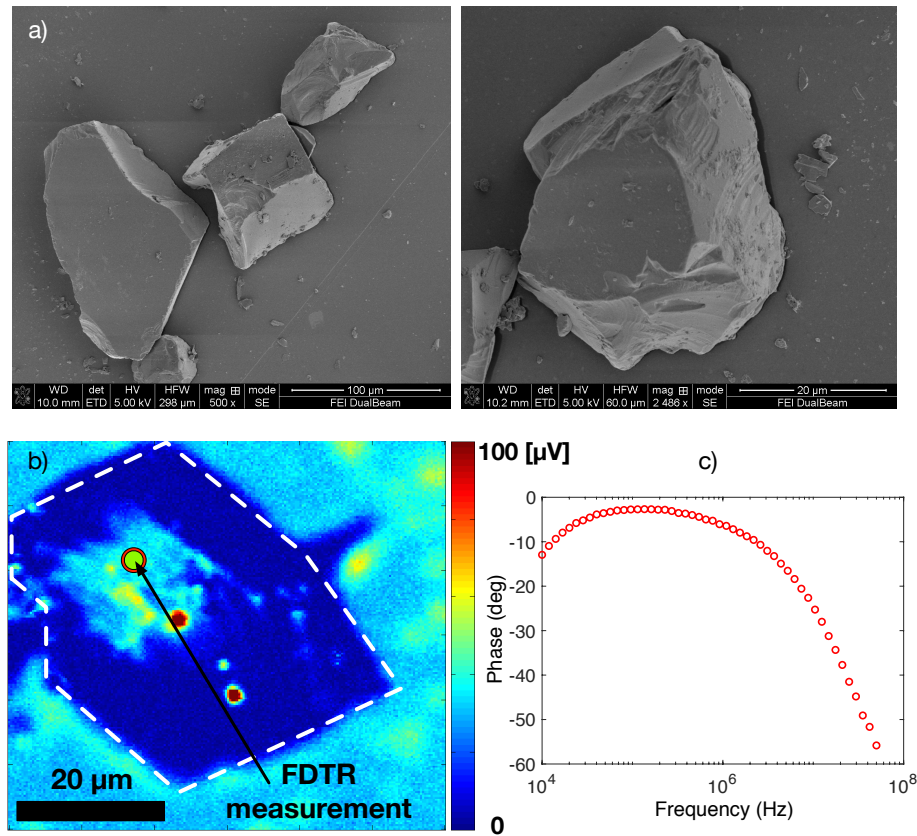


**Figure 4-4:** a) SEM images of silicon particles. The size ranged between 30 and 100  $\mu\text{m}$  in diameter. b) FDTR image of silicon particle P1. The arrow points at the spot where the measurement was conducted. The white dash line indicates the particle boundary. c) FDTR phase data acquired for Si particle P1.

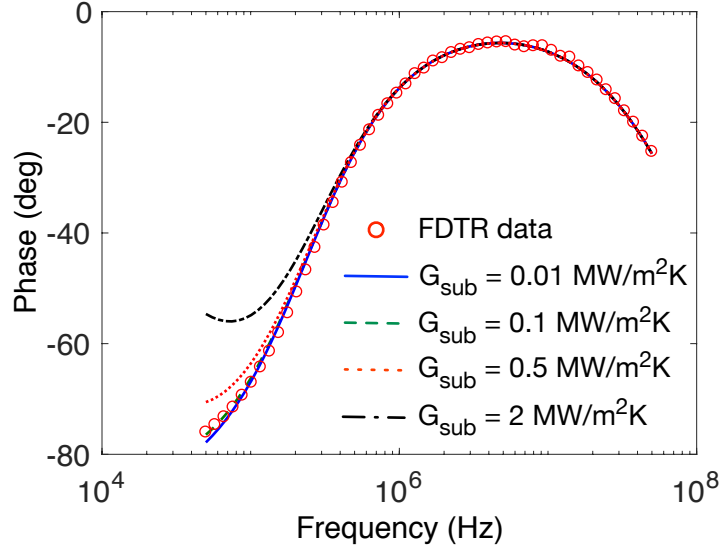


**Figure 4-5:** Effect of including the substrate in the model. The value of a thermal interface conductance ( $G_{\text{sub}}$ ) between the particle and the substrate would be under  $0.1 \text{ MW/m}^2\text{K}$ , which does not affect the phase response at the measurements frequency range. Curves shown for a  $10 \mu\text{m}$  size diamond particle.

measurement frequency range, as shown in Fig. 4-5. For larger diamond particles, these effects would take place at even lower frequencies far from the measurement frequency range. Similarly, the phase response was insensitive to the substrate for the sizes of silicon particles measured in this work. Therefore, it was not necessary to consider a third layer in the model for any of the particle types.

It is also important to address the effect of the convection boundary condition on the phase response. Figures 4-6 and 4-7 show the phase response of different size diamond and silicon particles, respectively, with and without a convection boundary condition. This boundary condition only applies to the side walls of the cylindrical layers, as indicated in Fig. 4-1. We found that a convection boundary condition did not affect our measurement frequency range until the convection coefficient would reach a value of approximately  $80000 \text{ W/m}^2\text{K}$ . Even though it has been reported that natural convection coefficients are much higher at the micro scale due to pure

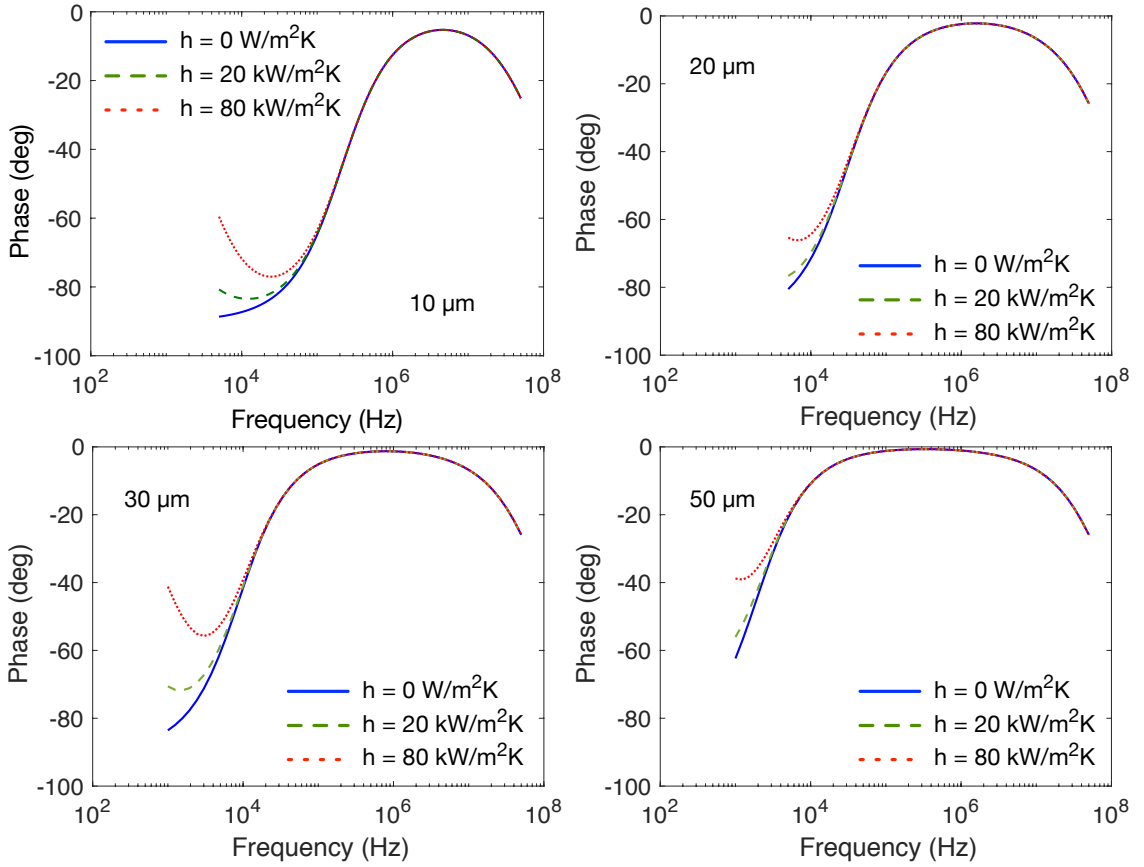


**Figure 4-6:** Effect of the convection coefficient on the temperature phase response for multiple size diamond particles. An unreasonably high convection coefficient is necessary to observe any effect at our measurement frequency range. The size is given as the average diameter.

heat conduction from the object to air, these reported values ( $\sim 1000 \text{ W/m}^2\text{K}$ ) are still more than an order of magnitude lower than the  $80,000 \text{ W/m}^2\text{K}$  minimum (Alam et al., 2013; Guan et al., 2014; Hu et al., 2008). Therefore, we neglected this boundary condition during our analysis and kept  $h = 0$  in the model for all particles measured.

### 4.3.2 Fitting procedure and uncertainty of the fit

We extracted the unknown physical parameters using a non linear least squares function in MATLAB to fit the model's prediction to the measured FDTR data. The unknown parameters in this two layer model were the particle radius,  $b$ , the parti-

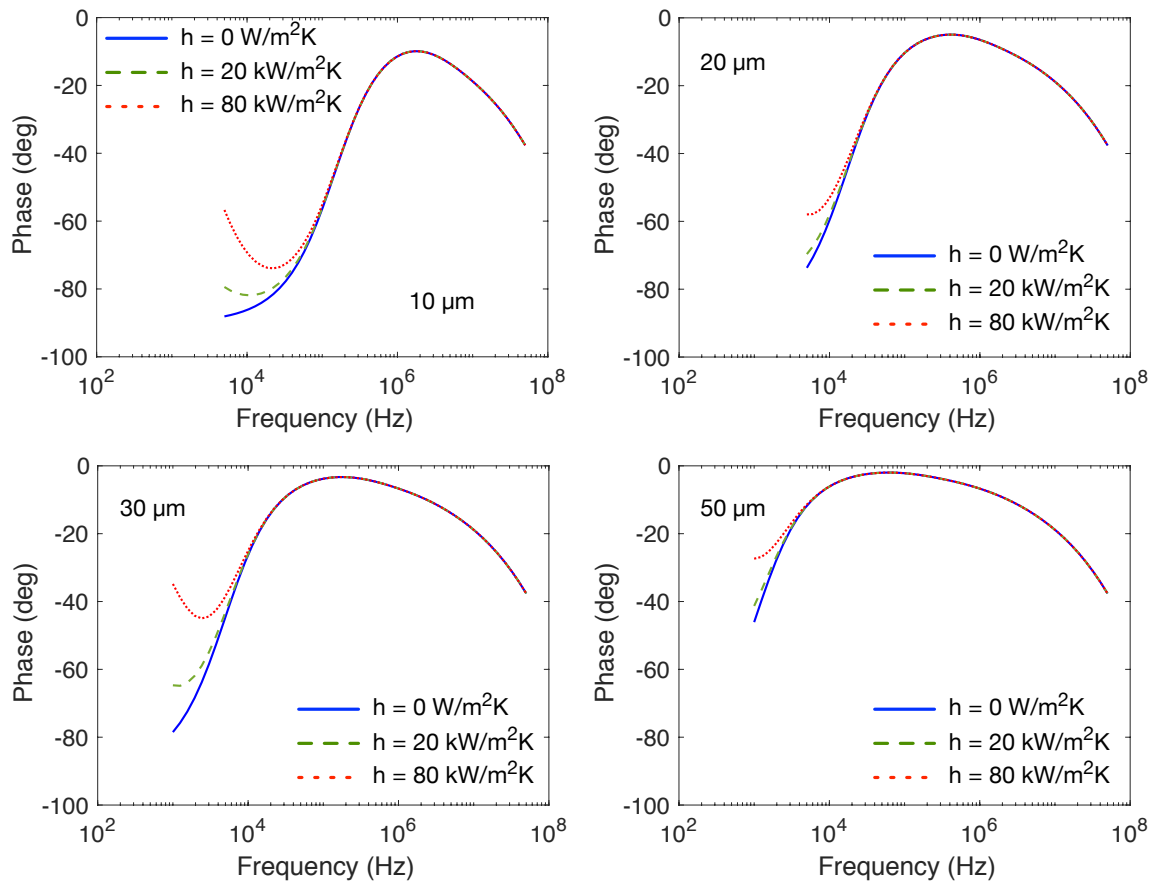


**Figure 4-7:** Effect of the convection coefficient on the temperature phase response for multiple size silicon particles. An unreasonably high convection coefficient is necessary to observe any effect at our measurement frequency range. The size is given as the average diameter.

cle layer thickness,  $d$ , the particle thermal conductivity,  $k$ , and the thermal interface conductance,  $G$ , between the metal transducer layer and the particle. In order to see if these four unknown parameters could be fit simultaneously, we used the following equation (Yang et al., 2016):

$$X_U = (J'_U J_U)^{-1} J'_U (\phi_n + J_C X_C J'_C) J_U (J'_U J_U)^{-1} \quad (4.28)$$

Equation 4.28 calculates uncertainty for the unknown parameters as the  $\pm 1/e$  confidence intervals around the best fit mean values. It accounts for noise, uncertainty in the known (also called controlled) model parameters, and correlation effects in the unknown parameters as well as in the controlled parameters and their uncertainties. The uncertainty values obtained with this equation are similar to those obtained with the Monte Carlo method. In Eq. 4.28  $X_U$  is a vector containing the uncertainty of the unknown parameters,  $J_U$  is the Jacobian matrix of the phase lag with respect to the unknown parameters for each measured frequency,  $\phi_n$  is a diagonal matrix containing the phase lag noise for each measured frequency,  $J_C$  is the Jacobian matrix of the phase lag with respect to the controlled (known) parameters for each measured frequency and,  $X_C$  is a diagonal matrix containing the uncertainty of the controlled parameters.  $J'_U$  and  $J'_C$  are the transpose matrices of  $J_U$  and  $J_C$ , respectively. These Jacobian matrices represent the sensitivity of the measurement to each physical parameter in the model.

If we set  $X_C$  to zero in Eq. 4.28, that is, if we neglect uncertainty in the controlled parameters, we can study the uncertainty of the fit alone. In other words, we can determine which combinations of unknown parameters can be fit simultaneously for a given amount of measurement noise. Since there were four unknowns in the model, we started by considering a four parameter fit ( $b, d, k, G$ ). First, we calculated the uncertainties of parameters  $b$  and  $d$  using Eq. 4.28 with  $X_C = 0$ . For both diamond

and silicon, the uncertainties obtained for  $b$  and  $d$  were several orders of magnitude larger than the particle sizes, indicating that these two parameters could not be fit simultaneously. Since  $b$  and  $d$  could not be fit together, we fixed parameter  $d$  to the laser focus distance between the particle and the substrate it was resting on. We then fit  $b$ ,  $k$  and  $G$ . This worked for all particles except the 10  $\mu\text{m}$  diamond ones. Figure 4-8 shows the uncertainty of the particle's thermal conductivity  $k$  in a three parameter fit ( $b, k, G$ ) for different particle sizes as a function of the particle's thermal conductivity. The uncertainty in Fig. 4-8 is uncertainty of the fit, that is, the uncertainty obtained with Eq. 4.28 when we set  $X_C$  to zero. For a thermal conductivity close to diamond's, the uncertainty is well over 50% for the 10  $\mu\text{m}$  particle size, indicating that a three parameter fit was not possible for this size. Thus, for these diamond particles, we fixed the interface conductance  $G$  to the average value obtained for the other sizes and fit the radius  $b$  and the thermal conductivity  $k$ . In the case of the silicon particles, a three parameter fit ( $b, k, G$ ) was possible in all sizes. For the bulk silicon sample, the multilayer stack model described in Ref. (Schmidt et al., 2009) was used to fit  $G$  and  $k$  of the silicon.

Another way to gain insight about how many parameters can be fit simultaneously is by looking at sensitivity curves. Figures 4-9 shows the measurement sensitivity to the particle's dimensions, thermal conductivity and thermal interface conductance as a function of frequency for different size diamond particles. We do this by considering the phase difference after changing parameter  $x$  by a  $\pm 20\%$  tolerance as follows:  $S_{x,20\%}(\omega) = \phi|_{1.2x}(\omega) - \phi|_{0.8x}(\omega)$  where  $S_x$  is the sensitivity of parameter  $x$ ,  $\omega$  represents the pump frequency and  $\phi$  is the phase lag. Parameters  $b$  and  $d$  show very similar curves and are sensitive in the same frequency range. Therefore, we could expect high uncertainties if fit simultaneously, as confirmed by Eq. 4.28.

In addition, Figs. 4-9 present features that can be interpreted in terms of two

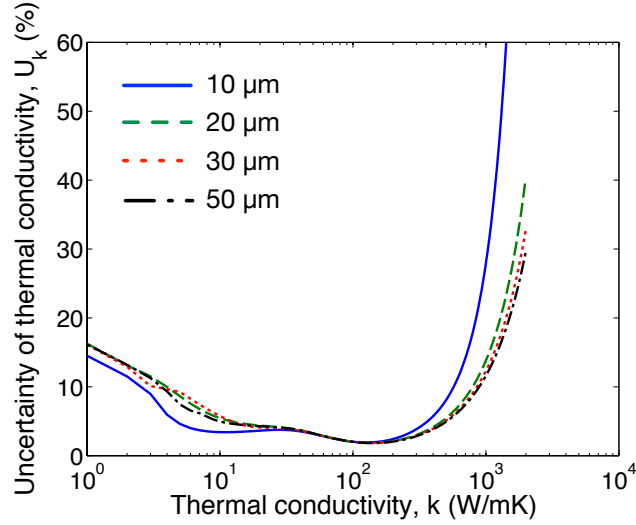


**Figure 4-8:** Uncertainty of the particle’s thermal conductivity for a wide range of thermal conductivities in a three parameter fit ( $b, k, G$ ). For 10  $\mu\text{m}$  size diamond particles, the uncertainty becomes too large and therefore it is not possible to fit the three parameters simultaneously. For silicon particles, a three parameter fit is possible for any of the sizes shown.

characteristic frequencies. The first is a frequency at which all parameters approach zero sensitivity. We refer to this frequency as  $F_b$ . It is related to the time it takes heat to reach the particle’s lateral boundaries and is given by  $\alpha/L_c$ , where  $\alpha$  represents the particle’s thermal diffusivity and  $L_c$  is a characteristic length. This is basically the thermal Fourier number without the time variable (Lienhard IV and Lienhard V, 2012). In the case of our particles,  $L_c$  is  $b$  or  $d$ , depending on which boundary we consider.

The second characteristic frequency, which we call  $F_{\text{peak}}$ , corresponds to the frequency of peak sensitivity in Figs. 4-9. This frequency is related to the external thermal time constant used to model lumped thermal systems. It can be expressed as  $F_{\text{peak}} = (\rho c_p V R_{\text{th}})^{-1}$  where  $\rho$  is the particle density,  $c_p$  is the particle specific heat,  $V$  is the particle volume, and  $R_{\text{th}}$  is the thermal resistance to heat leaving or entering the particle. In the case of coated diamond,  $R_{\text{th}}$  is dominated by the ther-

mal interface resistance ( $1/G$ ) between the transducer layer and the particle and it is therefore given by  $R_{\text{th}} = 1/(GA)$  where  $G$  is the thermal interface conductance between the transducer layer and the particle, and  $A$  is an effective laser spot area. We can calculate  $F_{\text{peak}}$  for different particle sizes and compare the values to those observed in the sensitivity curves. Figure 4-10 shows this comparison. The frequencies derived through the thermal time constant expression capture the correct trend with particle size indicating the particle behaves somewhat like a lumped system at such frequencies. The best fit was obtained for a spot size of  $0.56 \mu\text{m}$ , which is slightly below the  $1/e$  spot size used in our measurements. For other particle materials with a lower thermal conductivity than diamond,  $R_{\text{th}}$  should include a conduction thermal resistance ( $R_{\text{conduction}}$ ) associated with the particle material. In this case,  $R_{\text{th}}$  would be given by,  $R_{\text{th}} = 1/(GA) + R_{\text{conduction}}$ .

#### 4.4 Results and discussion

Figure 4-11 shows FDTR data and the model best fits for several diamond and silicon particles as well as for the bulk silicon sample. For both materials, the cylindrical layer model provided an excellent fit to the measured data. As predicted by the model (see Fig. 4-1b), the data show how the thermal response is independent of size for high frequencies where heat never reaches a particle's lateral boundaries. Also, the curves' peaks shift left towards lower frequencies with increasing particle size. The parameter values obtained with each fit are shown in Table 4.1. Instead of showing parameter  $b$  values, we report an effective volume ( $V_{\text{eff}}$ ) given by  $V_{\text{eff}} = \pi b^2 d$  since this is a more value for determining the characteristic thermal response time of a particle. The thermal conductivity values for the diamond particles are within the range of reported values (Barman and Srivastava, 2007; Olson et al., 1993; Yamamoto et al.,

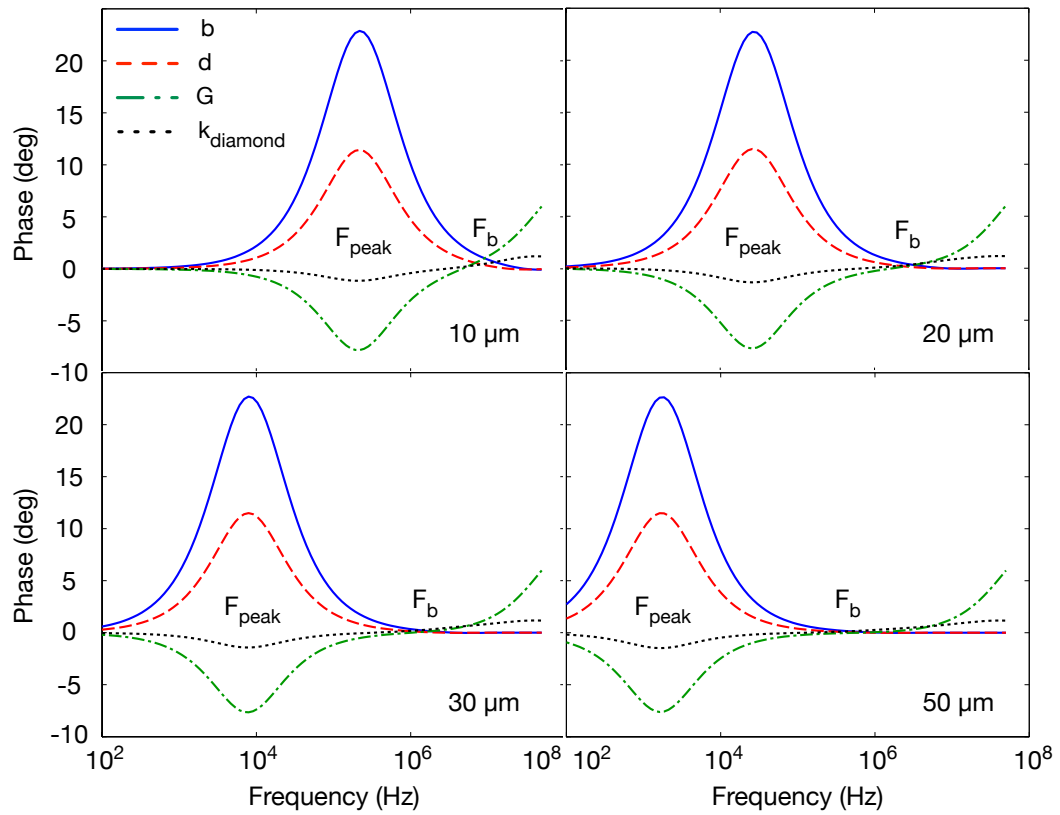


**Figure 4-9:** a) Sensitivity curves of parameters  $b$ ,  $d$ ,  $k$  and  $G$  for all four diamond particle sizes measured in this work. Frequency  $F_b$  represents the time at which heat reaches the particle boundaries. Frequency  $F_{\text{peak}}$  relates to the external time constant used in lumped systems.

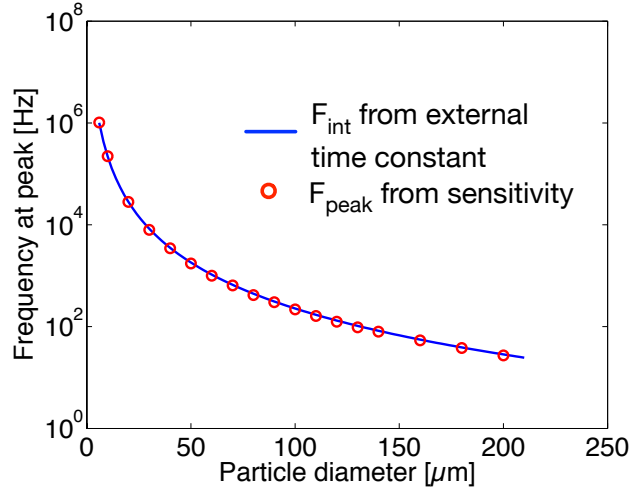


**Figure 4-10:** Comparison between  $F_{\text{peak}}$  and the lumped system time constant  $(\rho c_p V R_{\text{th}})^{-1}$  in diamond particles of different sizes. For diamond,  $R_{\text{th}} = 1/(GA)$  since the interface conductance is the dominant resistance to heat transferring in and out of the particle.

1997; Ruch et al., 2006; Slack, 1964). In the case of silicon, the bulk sample’s thermal conductivity is within experimental error compared to literature values reported (135 W/mK) for silicon with a similar doping level (Asheghi et al., 2002; Lee and Hwang, 2012). The silicon particles showed about a 25% lower thermal conductivity than the bulk sample. This could be caused by a significant increase in defect density introduced during the crushing process.

The uncertainty of the fit parameters shown in Table 4.1 was calculated using Eq. 4.28, including phase noise from the measurement and the uncertainties of the controlled model parameters. For the 10  $\mu\text{m}$  size,  $G$  was treated as a controlled parameter with an assigned tolerance as  $160 \pm 15 \text{ MW/m}^2\text{K}$ . In the case of diamond, the uncertainty of  $G$  is lower than that of  $k$  because  $G$  represents the largest thermal resistance to heat flow. Therefore, the measurement is more sensitive to the thermal interface conductance. In the case of silicon, the measurement is almost equally sensitive to  $k$  and  $G$  and hence the low uncertainty obtained for both properties.

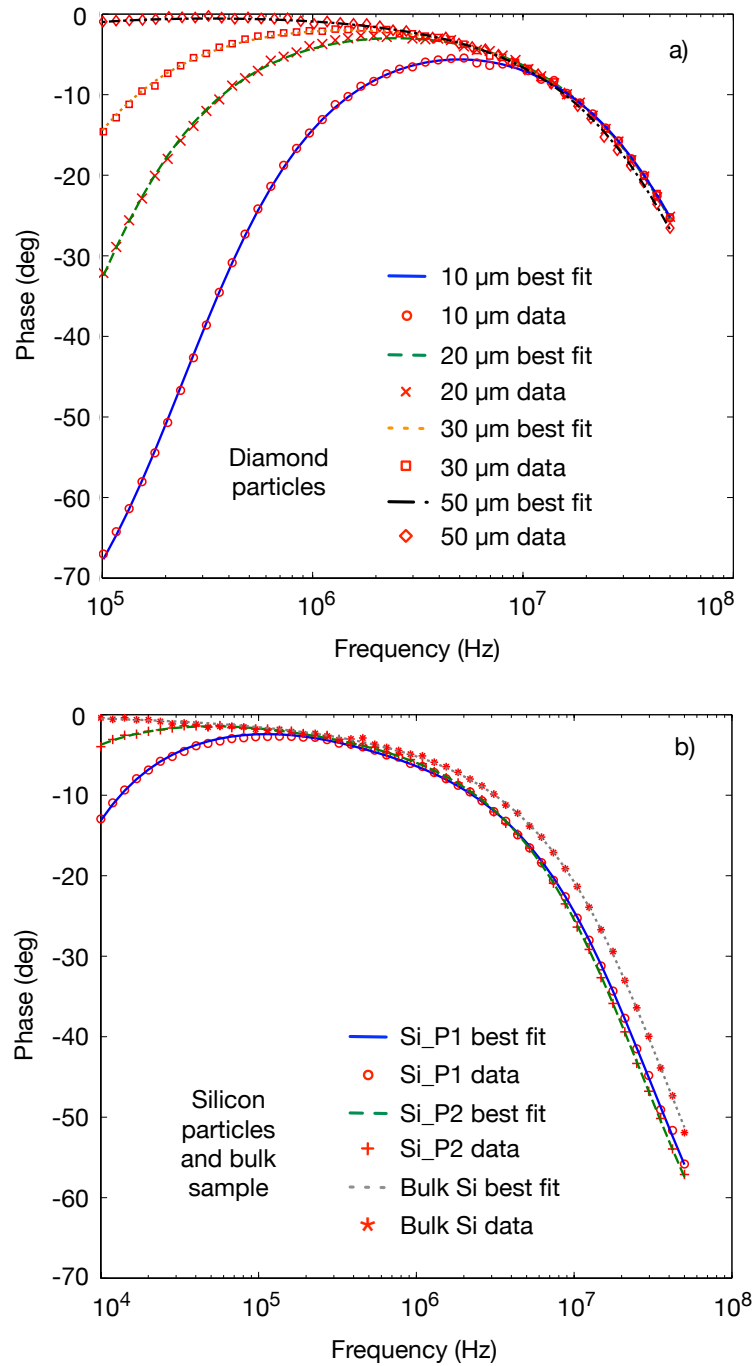


**Figure 4-11:** a) FDTR data and thermal model best fits for all four different size diamond particles. The thermal model shows an excellent fit to the measured data. b) FDTR data and thermal model best fits for the silicon particles and silicon bulk sample.

**Table 4.1:** Fitting parameter values for the best fit of each diamond and silicon particle size shown in Fig. 4.11 as well as the silicon bulk sample. D stands for diamond and Si for silicon.

	$V_{\text{eff}} (\mu\text{m}^3)$	Equivalent cube side ( $\mu\text{m}$ )	$k (\text{Wm}^{-1}\text{K}^{-1})$	$G (\text{MWm}^{-2}\text{K}^{-1})$
D (10 $\mu\text{m}$ )	$343 \pm 74$ (23%)	7	$1289 \pm 363$ (28.2%)	-
D (20 $\mu\text{m}$ )	$1279 \pm 241$ (18%)	11	$1352 \pm 284$ (21%)	$160 \pm 10$ (6%)
D (30 $\mu\text{m}$ )	$3251 \pm 404$ (13%)	15	$1157 \pm 151$ (13%)	$168 \pm 9$ (5%)
D (50 $\mu\text{m}$ )	$49695 \pm 2943$ (6%)	37	$1418 \pm 220$ (16%)	$146 \pm 7$ (5%)
Si P1	$11345 \pm 1124$ (10%)	22	$88 \pm 4$ (5%)	$28 \pm 1$ (4%)
Si P2	$39741 \pm 5175$ (13%)	34	$98 \pm 4$ (4%)	$24 \pm 1$ (4%)
Si (bulk)	-	-	$128 \pm 4$ (3%)	$36 \pm 1$ (3%)

#### 4.4.1 Spot size effects

Since the spot size used for these measurements is small (3.3  $\mu\text{m}$ ), it could introduce an error on the thermal conductivity values obtained through the thermal model. For silicon in particular, the distribution of phonons contributing to heat transport is quite broad, with most of the phonon mean free paths (MFPs) falling within a 0.3 - 8  $\mu\text{m}$  window (Regner et al., 2013). However, measurements on silicon with line heaters carried out by Zeng et al. showed that heater widths larger than 2  $\mu\text{m}$  returned a thermal conductivity very close to bulk value, indicating diffusive thermal transport (Zeng et al., 2015). Since our spot size is 3.3  $\mu\text{m}$ , our measurements should be dominated by diffusive heat transport. In the case of diamond, the MFPs span a narrower range of 0.5 - 3.5  $\mu\text{m}$  (Li et al., 2012b) and so should be less sensitive to size effects than silicon.

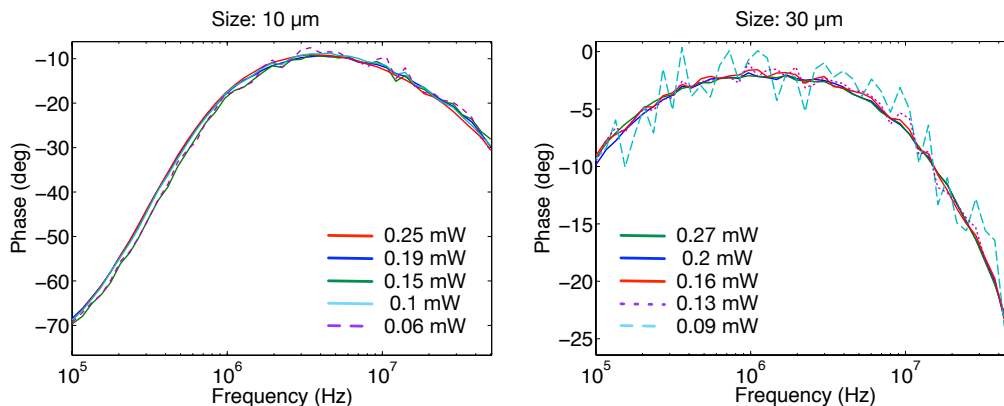


**Figure 4-12:** Temperature phase response for different laser input powers. The curves do not show any significant dependence to input power.

#### 4.4.2 Heating effects

Given the small size of the particles, it is important to consider the steady-state temperature rise due to the integrated heat flux from the pump and probe lasers. In order to test whether there was a significant temperature rise, we conducted a series of FDTR measurements on the same particle with different power levels. Figure 4-12 shows these measurements on two different diamond particles, one being  $10\ \mu\text{m}$  and the other one  $30\ \mu\text{m}$  in diameter. In both cases, the highest power tested is at least three times the lowest power. The thermal conductivity values extracted out of each measurement were within the uncertainty of the fit in both particles. If the temperature rise due to steady heating were significant, then the particle thermal property values should have changed for the different power levels. Since this was not the case, we can conclude that steady-state heating did not have significant effects on the thermal conductivity values obtained.

#### 4.4.3 Thermal conductivity of all particles measured

Figures 4-13 and 4-14 show the raw FDTR phase data and thermal conductivity measured and obtained for all diamond particles characterized in this work, respectively.

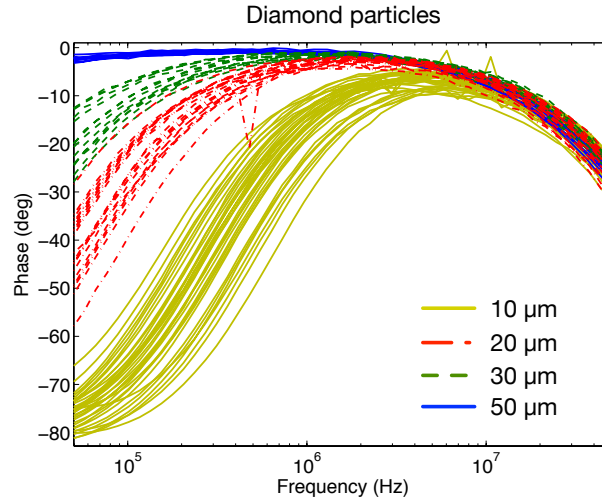


**Figure 4-13:** FDTR measured phase vs. frequency for all diamond particles.

We can see a wide range of scattered thermal conductivity values for all sizes, especially for the smaller particles. While it is true that the measurement uncertainty for the smaller values is considerable (21-28%), it can not explain by itself the large variation encountered for different particles with similar size. Since all particles were obtained from the same manufacturer, we assume the composition of them to be very similar. Thus, the large variation in thermal conductivity observed is probably due to different defect densities or defect sizes within each particle. This is only a hypothesis since we were not able to perform any XRD analysis on individual particles to compare defect densities or defect sizes.

Figures 4-15 and 4-16 show the raw FDTR phase data and thermal conductivity measured and obtained for all silicon particles characterized in this work, respectively. Similar to the diamond case, here there is also significant variation in the measured thermal conductivity values. In addition, there is a slight trend indicating lower thermal conductivity for smaller particles. This is probably due to a higher defect density in the smaller particles since they were formed after a longer crushing process. We do not think this is a size effect since all the silicon particles measured were larger

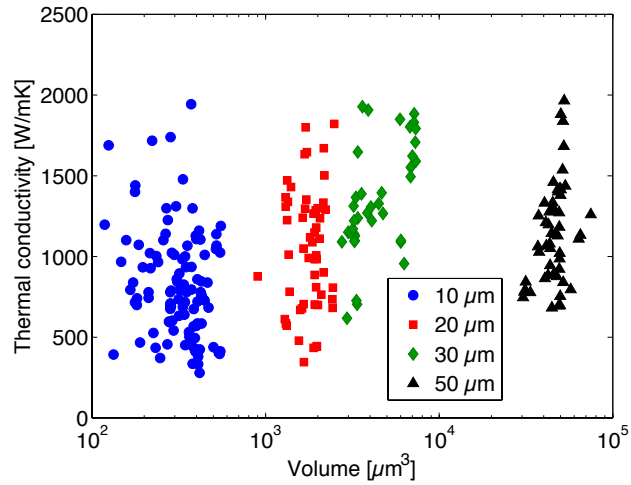


**Figure 4-14:** Thermal conductivity of all diamond particles measured in this thesis. There is not evident trend of a volume dependence.

than 10  $\mu\text{m}$ , which exceeds the phonon mean free path range for silicon (0.3 - 8  $\mu\text{m}$  (Regner et al., 2013)).

#### 4.4.4 Particle shape dependence

Figure 4-17 shows the phase response for a 15  $\mu\text{m}$  size diamond particle for multiple combinations of the radius  $b$  and the depth  $d$  while keeping the volume constant. We can see how the phase response changes significantly only for extreme shapes but it is very similar for ratios ( $b/d$ ) between 0.3 and 3, which encompasses the shape of all particles used in this work. This shows how the phase response of the particles is much more dependent on the volume rather than the shape.

## 4.5 Conclusion

In this work, we developed a thermal model for frequency domain thermoreflectance that can be applied to the measurement of the thermal properties of micron scale particles. The model considers the particles as layers of finite cylinders, with a thermal interface conductance between layers. In addition, the model includes a convection

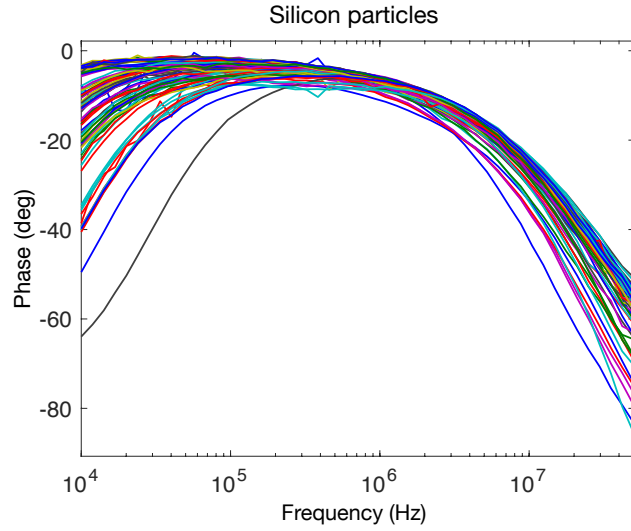


**Figure 4-15:** FDTR measured phase vs. frequency for the silicon particles.

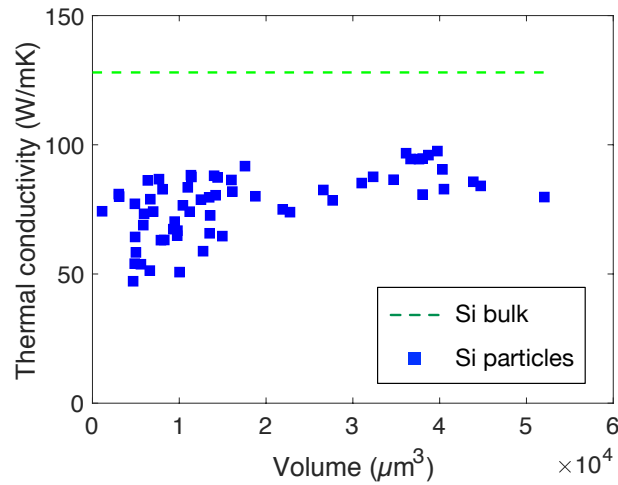


**Figure 4-16:** Thermal conductivity of all silicon particles measured in this thesis. There is a trend indicating reduced thermal conductivity for smaller particles. This might be due to a higher defect density in the smaller particles introduced during the crushing fabrication process.

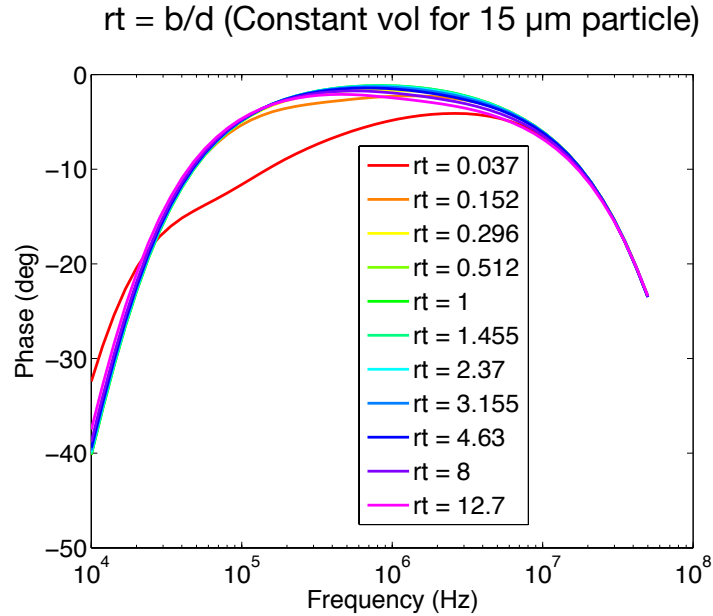


**Figure 4-17:** Phase response depending on the shape of the particle for a constant volume. We varied the ratio between the radius ( $b$ ) and depth ( $d$ ) of the particle to show the phase response does not strongly depend on the shape but it does on the volume.

boundary on the side of the cylindrical layers (see Fig. 4-1a), although in practice boundary convection can be largely ignored. Using this model in conjunction with FDTR imaging, we were able to measure the thermal properties of individual particles smaller than 10  $\mu\text{m}$ . We tested the model with multiple diamond and silicon particles of different sizes and found excellent agreement between the FDTR data and the model prediction. Thermal conductivity values obtained were within the range of previously reported values. The technique described in this paper can be used to characterize the thermal properties of micron scale particles embedded in a host medium or loosely distributed onto a flat surface, and could be useful for a wide variety of industrial applications, as well as for studying new materials that can only be synthesized in small sizes.

## Chapter 5

# Measuring particle-matrix interfaces with FDTR

### 5.1 Introduction

Particle reinforced composites can be a solution to satisfy thermal requirements in the microelectronics packaging industry. They can be tailored to match the low CTE of semiconductors and at the same time provide the necessary thermal conductivity to avoid device overheating (Jiang et al., 2013; Tong, 2011; Sarvar et al., 2006). High thermal conductivity particles such as diamond or SiC particles are embedded in metals like Al, Ag or Cu to obtain a high thermal conductivity material (Jiang et al., 2013; Ruch et al., 2006; Tavangar and Weber, 2012). The high particle volume fraction used in these composites as well as the small size of the particles (micron scale) generate a lot of particle-matrix interfaces, which can be detrimental to heat propagation (Nan et al., 1997; Every et al., 1992), as shown in Chapter 1.

These interfaces can play an important role in the overall thermal conductivity of the composite (Nan et al., 1997; Every et al., 1992). It is very difficult to predict the value of the thermal interface conductance due to lack of accurate theories and precise knowledge of the interfacial bonding between the particle and the matrix. For this reason, we investigate the possibility of using frequency domain thermoreflectance (FDTR) to measure in situ the thermal interface conductance between a particle and the matrix in a composite material. We do so by introducing heat directly into the

particle and let it diffuse from the particle into the matrix. Depending on particle size, particle thermal conductivity and the actual thermal interface conductance, we show it is possible to obtain an approximate value for the thermal interface conductance between the particles and the matrix material. As a proof of concept, we show measurements of the thermal interface conductance in a composite material consisting of diamond particles embedded in tin.

## 5.2 Experimental methods

### 5.2.1 Sample preparation

We prepared samples consisting of diamond particles in a tin matrix. The diamond particles were purchased from Advanced Abrasives and their size was around  $30\ \mu\text{m}$  in diameter. We obtained tin from Kurt J. Lesker in the shape of 3.2x3.2 mm pellets with a 99.998-99.999% purity. First, we deposited diamond particles dispersedly on a 20x20mm silicon chip. We then placed the chip on a hot plate with a few tin pellets on top. We increased the temperature until the tin pellets melted and pressed them down over the particles. After that, we removed the silicon chip so that we could measure the particles embedded at the surface. Figure 5-1 shows some SEM images of diamond particles in the tin matrix. The SEM images showed imperfect interfaces due to partial wetting on the side boundaries of the particle. Finally, to enable the FDTR measurements, the samples were coated with a metal transducer layer consisting of 5 nm of titanium with 95nm of gold on top via e-beam evaporation. A fused silica reference sample was coated in the same run to later obtain the thermal properties of the metal transducer layer.

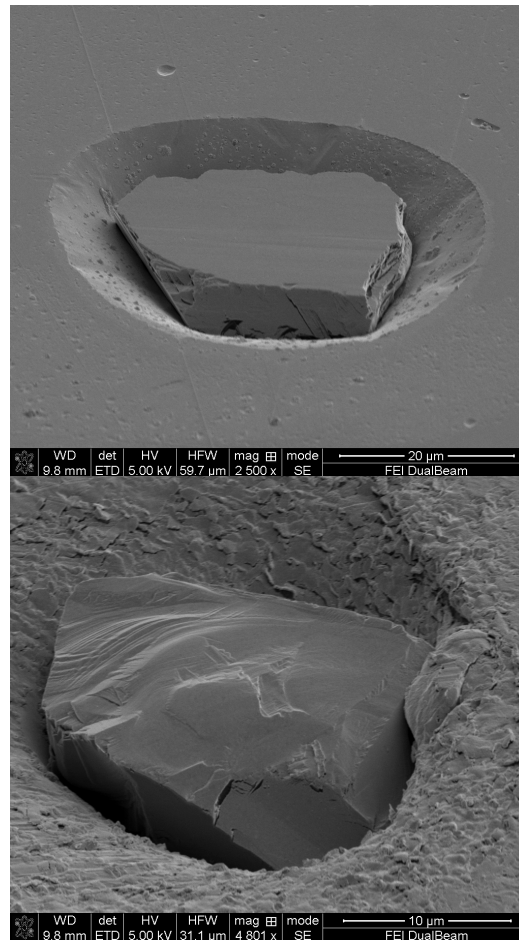


**Figure 5.1:** SEM images of the diamond tin samples fabricated for this work. The particles are diamond and the matrix is tin.

### 5.2.2 Frequency Domain Thermoreflectance (FDTR)

We used frequency domain thermoreflectance to carry out the measurements on the diamond tin samples (Schmidt et al., 2009; Yang et al., 2013; Yang et al., 2014). Here a periodically modulated continuous wave laser (pump) is focused to a Gaussian spot to provide the heat flux while a second unmodulated laser (probe) monitors the surface temperature. The phase lag,  $\phi$ , between these two signals is recorded with a lock-in amplifier for multiple frequencies and is compared to the phase lag predicted by a thermal model. We chose the Gaussian laser spot sizes of the pump and probe lasers to be  $3.3 \mu\text{m}$  and  $2.6 \mu\text{m}$  in  $1/e^2$  diameter, respectively, so that they could be fully focused on the particles.

### 5.3 Thermal model

The modeled signal from the lock-in amplifier is a complex number  $Z(\omega)$ :

$$Z(\omega) = \beta H(\omega) \quad (5.1)$$

where  $\beta$  is a constant and  $H(\omega)$  is the frequency response to the surface temperature of the sample. The constant  $\beta$  is given by

$$\beta = G_{\text{det}} P_{\text{pump}} P_{\text{probe}} (1 - R_{\text{pump}}) R_{\text{probe}} \left( \frac{dR}{dT} \right)_{\text{probe}} \quad (5.2)$$

where  $G_{\text{det}}$  is a constant that encompasses the gain of the photodetector and power reduction from optical components,  $P_{\text{pump}}$ ,  $P_{\text{probe}}$ ,  $R_{\text{pump}}$  and  $R_{\text{probe}}$  are the powers and reflectivities of the pump and probe lasers, respectively, and  $\left( \frac{dR}{dT} \right)_{\text{probe}}$  is the thermoreflectance coefficient at the probe wavelength. To find  $H(\omega)$ , we consider isotropic diffusive heat transport and therefore we solve the following heat equation in the frequency domain.

$$k \frac{\partial^2 T}{\partial r^2} + \frac{k}{r} \frac{\partial T}{\partial r} + k \frac{\partial^2 T}{\partial z^2} = j\omega CT \quad (5.3)$$

where  $k$  represents thermal conductivity,  $C$  represents volumetric heat capacity,  $\omega$  is angular frequency,  $j$  is the imaginary unit and  $T$  is the unknown temperature field.

We modeled the particles as finite cylinders surrounded by a large concentric cylinder which represents the matrix. Figure 5-2a shows a schematic of the particle-matrix model used for this study. We considered a thermal interface conductance ( $G$ ) acting over the entire interface between the particle and matrix cylinders. The focused laser heat source was modeled as a Gaussian heat flux on top of the particle surface aligned with the cylinder axis, as shown in Fig. 5-2a. This condition was given by,

$$-k \frac{\partial T}{\partial z} \Big|_{z=0} = \dot{q}_{1l, \text{top}} = Pe^{-\frac{2r^2}{a_1^2}} \quad (5.4)$$

where  $P$  is the input laser power and  $a_1$  is the  $1/e^2$  pump beam radius.

We modeled the matrix cylinder as a semi-infinite medium by assigning dimensions 30% longer than the thermal penetration depth in the material. Therefore, we could assume no heat flux at the outer boundaries. Figure 5-3 shows the thermal penetration depth in tin for the frequency range used in our measurements. We can see how the matrix must be drawn much larger than the particle in order to appropriately consider no heat flux at the outer boundaries. We solved the temperature field numerically using the MATLAB PDE toolbox. Figures 5-2b and 5-2c show a schematic of the model geometry used in MATLAB and the mesh used for the numerical calculations, respectively. As we can see, we used a 2D axisymmetric geometry. We modeled the interfaces as layers with a given thickness,  $th$ , having zero heat capacity and a thermal conductivity,  $k_{int} = G_{int} \cdot th$ , where  $G_{int}$  is the thermal interface conductance of the interface.

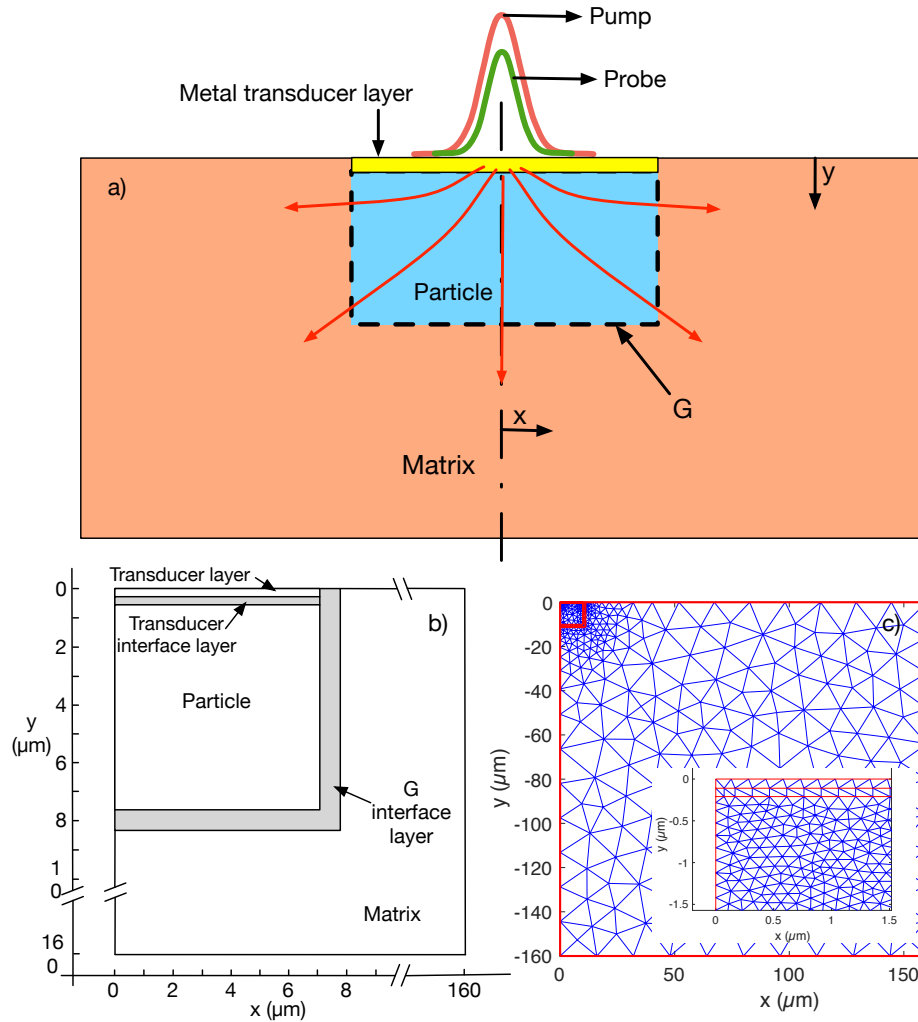


**Figure 5.2:** a) Particle-matrix model. Both the particle and matrix are cylindrical. The matrix cylinder was large enough to be able to assume zero heat flux at the outer boundaries. A gaussian heat flux was applied to the top surface. b) Model geometry used for MATLAB PDE toolbox. Interfaces were modeled as layers with zero heat capacity and thermal conductivity,  $k_{int} = G_{int} \cdot th$ , where  $G_{int}$  is the thermal interface conductance of the interface and  $th$  is the thickness of the interface layer. c) Mesh used to solve the model. Inset: zoomed in view of the area where the lasers were focused showing at least 10 nodes per micron to properly capture heat flux on that important region.

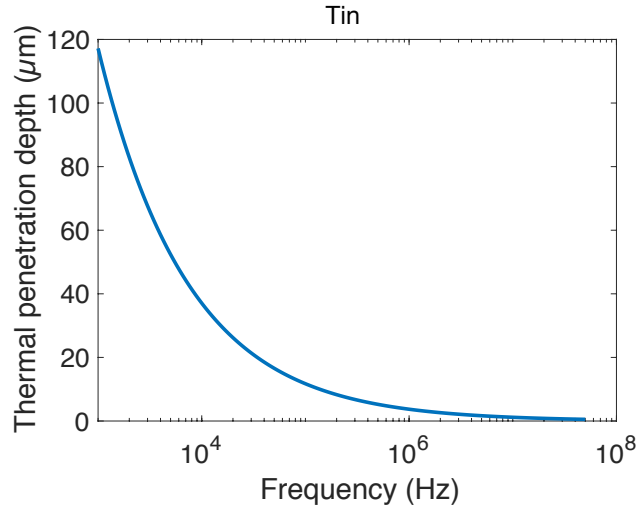


**Figure 5-3:** Thermal penetration depth in tin for a wide range of frequencies. We modeled the matrix material as 30% larger than the thermal penetration depth at the lowest frequency. This way we could correctly assume no heat flux at the matrix outer boundaries.

The MATLAB PDE toolbox is designed to solve partial differential equations that fit with the following format:

$$m \frac{\partial^2 u}{\partial t^2} + d \frac{\partial u}{\partial t} - \nabla \cdot (c \nabla u) + au = f \quad (5.5)$$

where  $m$ ,  $d$ ,  $c$ ,  $a$  and  $f$  are coefficients that can be functions of space. In some cases, they can also be functions of the solution  $u$  and its gradient.

In addition, there are two choices for boundary conditions on the edges of the 2D geometry.

1. Dirichlet condition:

$$hu = r \quad (5.6)$$

where  $h$  and  $r$  can be solutions of space, the solution  $u$  and time.

2. Neumann condition:

$$\vec{n} \cdot (c \nabla u) + qu = s \quad (5.7)$$

where  $\vec{n}$  is the outward unit normal at the edge,  $q$  and  $s$  can be functions of space, the solution  $u$  and time.

We can adapt Eq. 5.5 to our heat equation, Eq. 5.3, by assigning the following values to the coefficients:

- $m = 0$
- $d = 0$
- $c = kr$
- $a = j\omega Cr$
- $f = 0$

where  $k$  is thermal conductivity,  $C$  is volumetric heat capacity,  $\omega$  is angular frequency,  $j$  is the imaginary unit and  $r$  represent the radial spatial coordinate in a typical cylindrical coordinate system.

Note how both coefficients  $c$  and  $a$  depend on the spatial variable  $r$ . This would not be the case if we were trying to solve the heat equation in cartesian coordinates. The explanation to this is that MATLAB PDE solver is only prepared to work with cartesian coordinates. In other words, the  $\nabla$  operator is fixed to the cartesian coordinate system. For this reason, we had to include the variable  $r$  in those coefficients so that ultimately we solve the heat equation in cylindrical coordinates. Special attention to this must also be paid when defining the boundary conditions. In the case of the Gaussian heat flux present on top of the particle (Eq. 5.4), we use the Neumann boundary condition in the following manner:

$$\vec{n} \cdot (c\nabla u) = s = r \cdot Pe^{-\frac{2r^2}{a^2}} \quad (5.8)$$

The variable  $r$  located in front of the right hand side term is not in Eq. 5.4. However, we had to include it in coefficient  $s$  so that it cancels out the variable  $r$  introduced in coefficient  $c$ .

Once we obtained the temperature field, we selected the nodes at the top surface and then interpolated over 100 temperature values between them. Finally, we added the effect of the probe beam. The measured signal is an average of the surface temperature distribution weighted by the intensity distribution of the probe beam. Since the probe beam has a Gaussian spot we find  $H(\omega)$  to be,

$$H(\omega) = \int_0^{\infty} P_{\text{probe}} e^{-\frac{2r^2}{a_2^2}} 2\pi r T_{\text{top}}(r) dr \quad (5.9)$$

where  $P_{\text{probe}}$  is the probe power,  $a_2$  is the probe beam  $1/e^2$  spot radius and  $T_{\text{top}}$  is the temperature at the sample surface provided by MATLAB. We computed this integral numerically through the trapezoidal rule. We fitted the phase of  $H(\omega)$  to the phase of the measured signal  $Z(\omega)$  to extract the unknown thermal properties of our samples.

In order to make sure we used the right mesh size and implemented the PDE toolbox correctly, we compared the numerical model developed in this chapter to the thermal model derived in Chapter 4 under the conditions of an isolated particle. We did this by setting the thermal interface conductance between the particle and the matrix to zero ( $G = 0$ ). As for the model derived in Chapter 4 we set the convection coefficient  $h$  to zero ( $h = 0$ ). Figure 5-4 shows the phase curve obtained for both cases. We can see a perfect agreement between the two phase curves indicating we chose the right mesh size for our numerical model and the solution is accurate.

Once the numerical model was validated, we studied the sensitivity of the technique to the thermal interface conductance ( $G$ ) between the particle and the matrix. We did this by calculating the uncertainty of this thermal interface conductance according to the following formula, which in general accounts for noise, uncertainty in

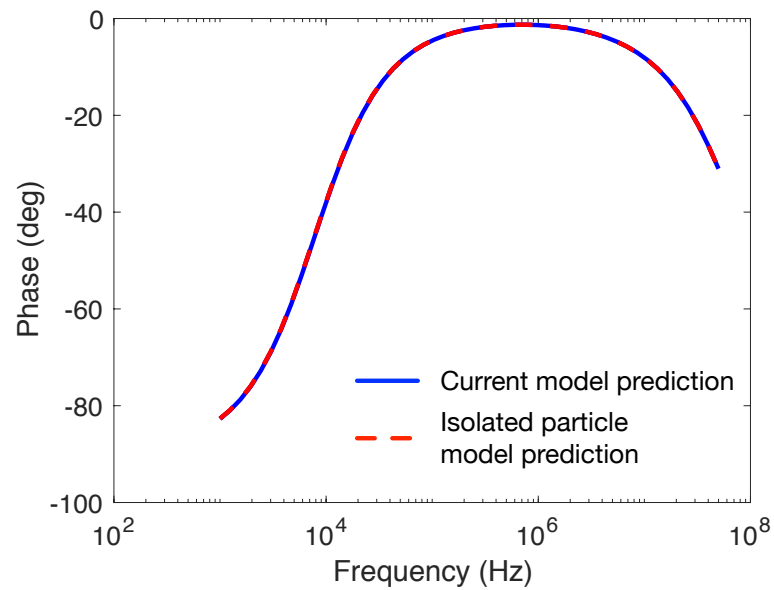


**Figure 5-4:** Phase response comparison between the current particle-matrix model with  $G = 0$  and the model derived in Chapter 4. We did this to see how accurate the numerical solution was. The curves correspond to a  $30 \mu\text{m}$  diamond particle coated with a metal transducer layer.

the known (also called controlled) model parameters, and correlation effects in the unknown parameters as well as in the controlled parameters and their uncertainties (Yang et al., 2016).

$$X_U = (J'_U J_U)^{-1} J'_U (\phi_n + J_C X_C J'_C) J_U (J'_U J_U)^{-1} \quad (5.10)$$

Equation 5.10, used in problems where a model is fitted to measured data, calculates uncertainty for the unknown parameters as the  $\pm 1/e$  confidence intervals around the best fit mean values and it provides similar values to those obtained with the Monte Carlo method. In Eq. 5.10  $X_U$  is a vector containing the uncertainty of the unknown parameters,  $J_U$  is the Jacobian matrix of the phase lag with respect to the unknown parameters for each measured frequency,  $\phi_n$  is a diagonal matrix containing the phase lag noise for each measured frequency,  $J_C$  is the Jacobian matrix of the phase lag with respect to the controlled (known) parameters for each measured frequency and,  $X_C$  is a diagonal matrix containing the uncertainty of the controlled parameters.  $J'_U$  and  $J'_C$  are the transpose matrices of  $J_U$  and  $J_C$ , respectively. These Jacobian matrices represent the sensitivity of the measurement to each physical parameter in the model. Since we were only interested in seeing if the measurement of  $G$  was possible we ignored the uncertainty of the controlled parameters and set  $X_C = 0$ . We calculated the uncertainty of  $G$  depending on the thermal conductivity of the matrix material for different particle materials and sizes as well as different values of  $G$ . Figure 5-5 summarizes these calculations. We can quickly observe two trends: the uncertainty in  $G$  increases with increasing particle size as well as with decreasing matrix thermal conductivity. If the matrix has a low thermal conductivity, the thermal resistance at the particle-matrix interface becomes negligible comparing to the matrix thermal resistance and therefore it will not be possible to measure  $G$ . Similarly, as the particle size increases the thermal resistance in the particle becomes

much larger than the thermal resistance at the interface and therefore we lose sensitivity to  $G$ . Likewise, for certain values of  $G$ , the thermal resistance at the interface will be negligible comparing to the rest and this technique will not be able to detect it. For instance, if we have  $30\ \mu\text{m}$  size diamond particles embedded in a matrix with a thermal conductivity higher than  $100\ \text{W/mK}$ , the technique will only measure  $G$  if its value is equal or lower than  $20\ \text{MW/m}^2\text{K}$  approximately. Otherwise, the uncertainty of  $G$  becomes too large. If we then increase the size of the particles to  $60\ \mu\text{m}$ , the technique will only detect thermal interface conductances lower than  $5\ \text{MW/m}^2\text{K}$ .

## 5.4 Sample results

In order to test the technique we fabricated samples consisting of diamond micro particles embedded in tin. We chose diamond particles because of the interest in them for advanced thermal management materials and tin because of its relatively high thermal conductivity ( $\sim 66\ \text{W/mK}$ ) and low melting point, which facilitated the sample fabrication. The unknown model parameters for these samples were: the particle radius ( $rad$ ), the particle depth ( $dep$ ), the particle thermal conductivity ( $k_p$ ), the thermal interface conductance between the transducer layer and the particle ( $g$ ), the particle-matrix thermal interface conductance ( $G$ ) and the matrix thermal conductivity ( $k_m$ ). We used Eq. 5.10 to see how many unknown parameters we could fit simultaneously. We found that it was possible to fit  $rad$ ,  $k_p$ ,  $g$  and,  $G$ . Figure 5-6 shows the sensitivity curve for the fitting parameters. We calculated the sensitivity the same way we did in Chapter 4. We can see how  $G$  and  $rad$  are not sensitive at the high frequencies because heat does not reach the particle boundaries. Therefore, the high frequencies determine the values of  $g$  and  $k_p$  while the low frequencies determine the particle size and the particle-matrix thermal interface conductance ( $G$ ). For all parameters the sensitivity is well above the 0.2-0.3 degree noise floor of our FDTR

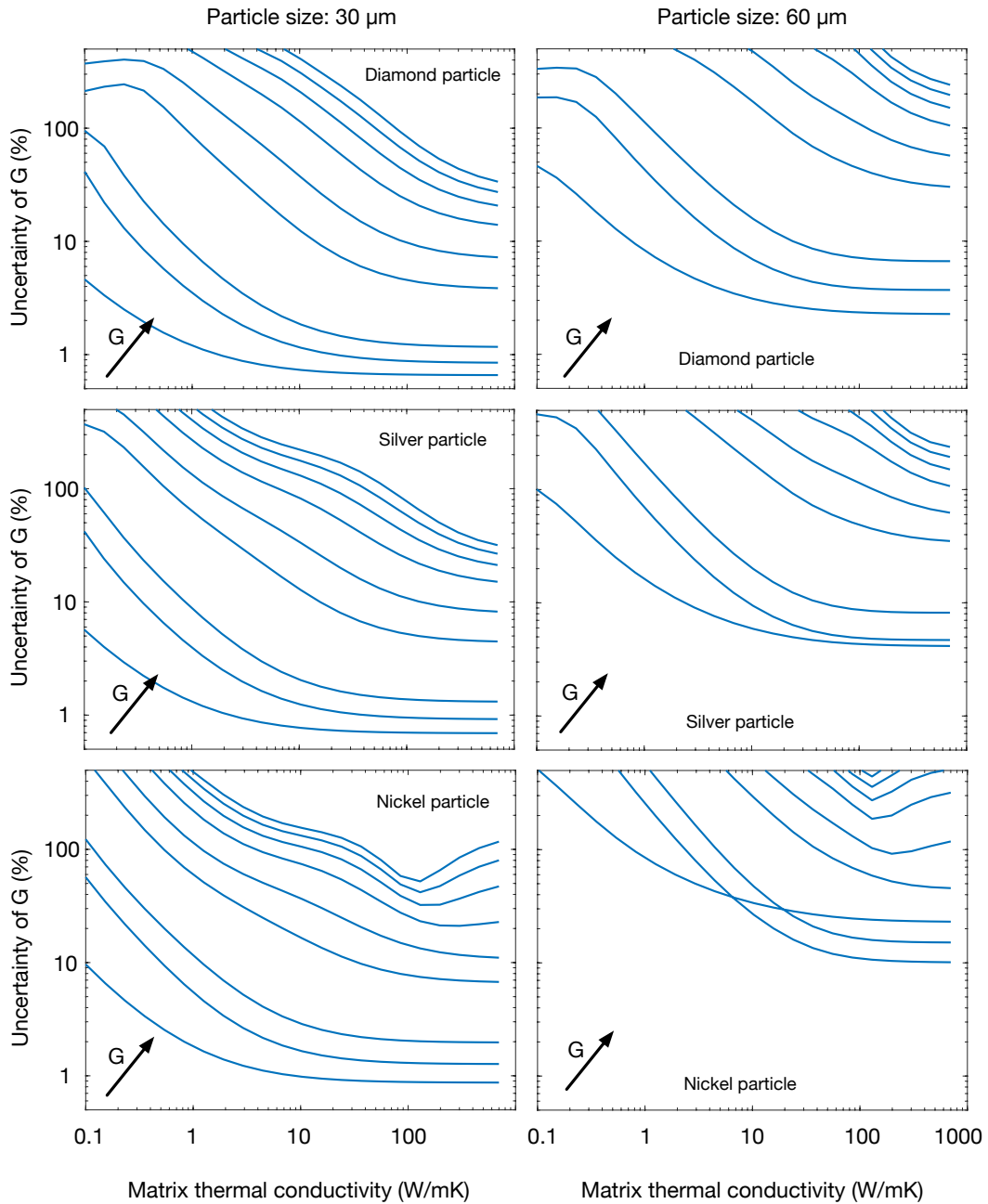


**Figure 5-5:** Uncertainty of  $G$  for different particle sizes and materials as a function of the matrix thermal conductivity and the  $G$  value itself.  $G$  values: 0.1, 0.5, 1, 5, 10, 20, 30, 40, 50 MW/m<sup>2</sup>K. Arrow points in the direction of increasing  $G$ .

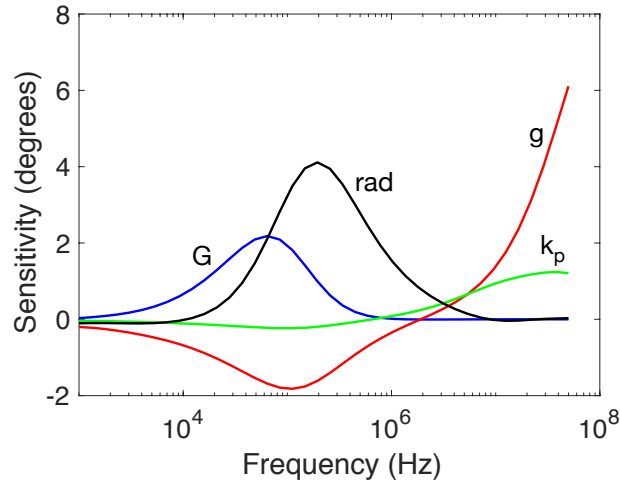


**Figure 5-6:** Sensitivity plot of the fitting parameters  $rad$ ,  $k_p$ ,  $g$  and,  $G$ . The values used for this plot were  $10\ \mu\text{m}$ ,  $1200\ \text{W/mK}$ ,  $165\ \text{MW/m}^2\text{K}$  and  $5\ \text{MW/m}^2\text{K}$  respectively.

system.

We considered the particle depth ( $dep$ ) to be equal to the radius ( $rad$ ) since the phase response is more dependent on the particle volume than the shape. Figure 5-7 shows the phase response for several particles with the same volume but different shapes (radius to depth ratio). We can see how all curves are within 0.3 degrees, which does not significantly change the values of the fitted parameters. Since we were not fitting the thermal conductivity of the matrix ( $k_m$ ), we measured it at multiple locations near the particle (around  $40\ \mu\text{m}$  away from the particle's edge). Figure 5-8a shows FDTR data and the best fit curve for a matrix measurement. The thermal conductivity obtained was  $63 \pm 4\ \text{W/mK}$ , which agrees with reported measurements for pure tin (ASM International Staff, 1991). In order to use the model described earlier, we performed measurements on single particles far enough from other particles to avoid any kind of thermal interaction among them. Figure 5-8b shows FDTR data and the best fit curve for several diamond particles in tin. We can see how the model accurately matches the thermal response of the sample. Table 5.1 contains the

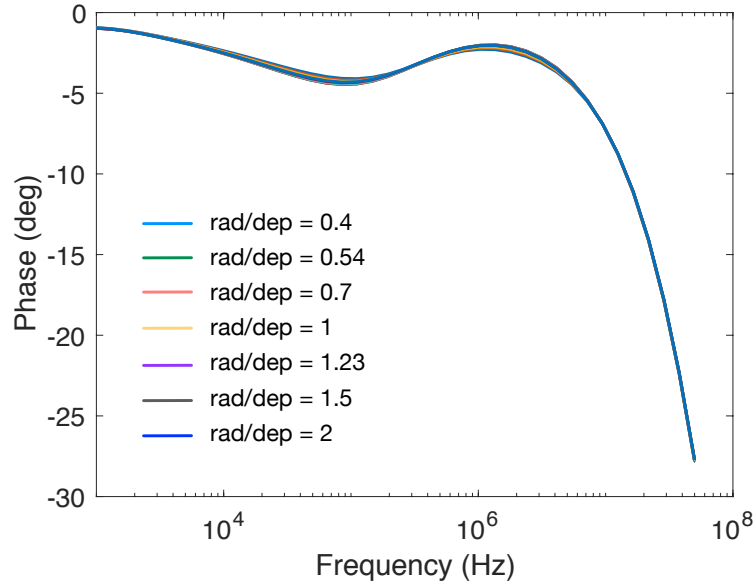


**Figure 5.7:** Phase response depending on the shape of the particle for a constant volume. We varied the ratio between the radius (*rad*) and depth (*dep*) of the particle to show the phase response does not strongly depend on the shape but it does on the volume.

values for  $rad$ ,  $k_p$ ,  $g$  and  $G$  for several particles. The low values obtained for  $G$  are reasonable if we look at Fig. 5.1, which shows partial bonding between the particle and the matrix. In addition, this  $G$  is affected by the geometry chosen for the model since in reality our particles do not have a cylindrical shape. A more realistic value would be given by the following equation:  $G_{\text{real}} = G(2\pi \cdot rad^2 + \pi \cdot rad^2)/A_{\text{real}}$ , where  $A_{\text{real}}$  is the real surface area of the interface between the particle and the matrix. The values obtained for the thermal conductivity of diamond agree well with previously reported measurements (Barman and Srivastava, 2007; Olson et al., 1993; Yamamoto et al., 1997).

Figure 5.9 shows the measured FDTR phase curves for many different diamond particles in the tin matrix.

Table 5.2 contains the fitted properties for the rest of the diamond particles measured and shown in Fig. 5.9.

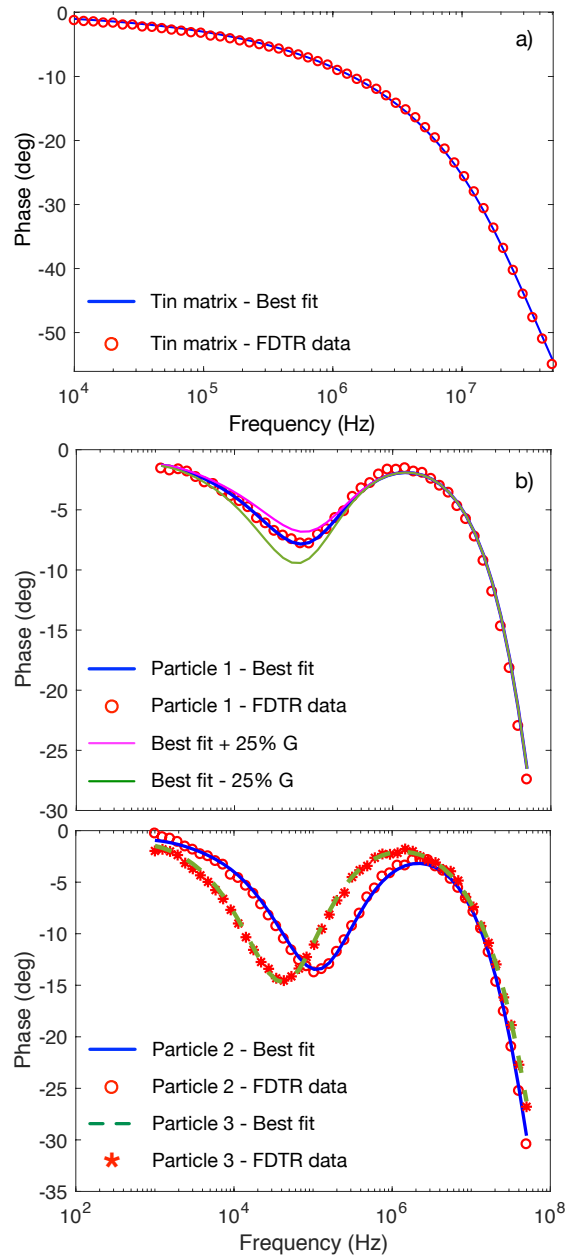


**Figure 5.8:** a) FDTR data and best fit for a measurement of the tin matrix. The fitted properties were the thermal interface conductance to the transducer layer and the thermal conductivity of tin. It provided a thermal conductivity of 63 W/mK. b) FDTR data and best fits for diamond particles in tin. The figure on top also shows the model prediction for a  $G$  25% higher and lower than the one obtained for the best fit.

**Table 5.1:** Fitted parameter values for the best fits of the three diamond particles shown in Fig. 5.8.

	$g$ (MW/m <sup>2</sup> K)	$rad$ ( $\mu m$ )	$k_p$ (W/mK)	$G$ (MW/m <sup>2</sup> K)
Particle 1	$150 \pm 9$	$10.9 \pm 0.2$	$1700 \pm 460$	$4.2 \pm 0.25$
Particle 2	$132 \pm 8$	$7.8 \pm 0.1$	$1280 \pm 310$	$3.2 \pm 0.1$
Particle 3	$167 \pm 9$	$11.1 \pm 0.1$	$1080 \pm 139$	$1.6 \pm 0.05$
Tin matrix	$43 \pm 2$	-	$63 \pm 4$	-

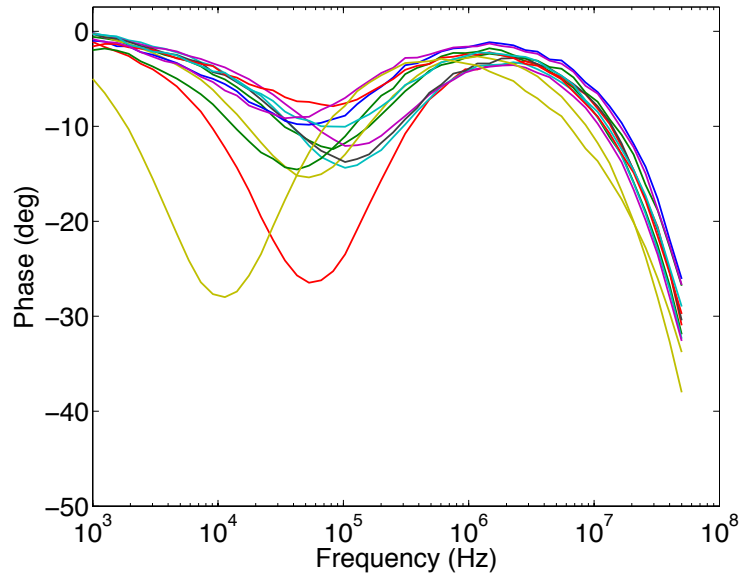


**Figure 5.9:** FDTR phase data for diamond particles embedded in tin.

**Table 5.2:** Fitted parameter values for the best fits of all diamond-tin particles measured.

	$g$ (MW/m <sup>2</sup> K)	$rad$ ( $\mu m$ )	$k_p$ (W/mK)	$G$ (MW/m <sup>2</sup> K)
Particle 4	128	7.7	1290	1.1
Particle 5	120	9	1200	2.6
Particle 6	120	7.5	1000	2.9
Particle 7	124	7.5	800	3.8
Particle 8	93	8.8	700	1.5
Particle 9	160	11.5	2000	2.8
Particle 10	150	10.4	850	4.3
Particle 11	151	9.6	950	3.3
Particle 12	151	12.6	2000	2.5
Particle 13	111	12.5	1530	2.4
Particle 14	99	11.4	750	3.5

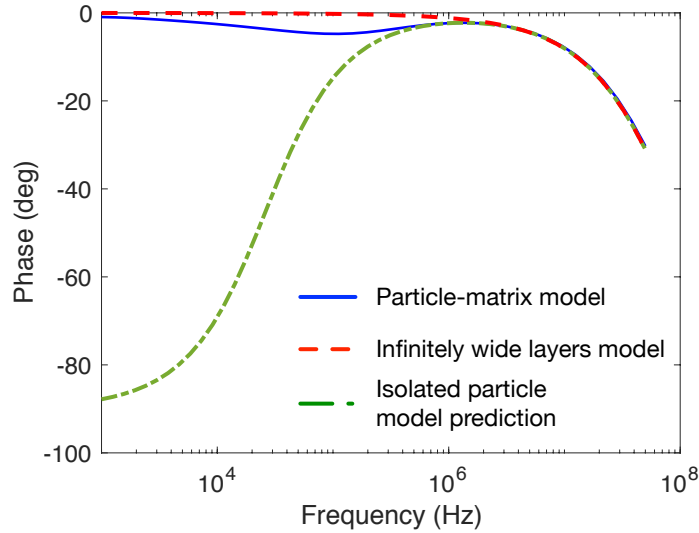


**Figure 5-10:** FDTR phase response for three different thermal models: the solid line represents the particle-matrix model developed in this chapter; the dashed line represents the conventional multilayer model with infinitely wide layers; the dashed-dot line represents the isolated cylindrical layers model ( $h = 0$ ).

Finally, we can also compare the three different models used in this thesis to carry out FDTR measurements. In Chapter 3 we used the conventional multilayer stack model. Here each layer is assumed to be infinitely wide in the in-plane direction. In Chapter 4 we used a cylindrical layer model with a convection boundary condition on the side walls and in this chapter we developed a model for cylindrical layers embedded in a concentric matrix material. Figure 5-10 shows the phase response for these three models considering a diamond layer, an isolated diamond particle and a diamond particle embedded in tin, respectively.

## 5.5 Conclusion

We present a technique with the potential to measure in situ the thermal interface conductance ( $G$ ) between a particle and its matrix in a particle reinforced composite material. The technique is based on frequency domain thermorefectance. It focuses

two lasers on top of the particle and introduces heat that will diffuse into the matrix material. The sensitivity of the measurement to the particle-matrix thermal interface conductance will depend on the matrix material, the particle size and the actual value of the thermal interface conductance. In general, high thermal conductivity matrix materials and small particles will have a wider range of thermal interface conductance measurable values. We use a numerically solved thermal model to extract  $G$  and other unknown properties such as the thermal conductivity of the particles. We tested the technique with some diamond-tin samples and obtained results for the thermal interface conductance between the diamond particles and the tin matrix. This technique could be useful for a wide variety of industrial applications, especially for those developing high thermal conductivity composite materials via particle reinforcement since it would allow them to approximately characterize the particle interfaces.

## Chapter 6

# Conclusions

### 6.1 Summary of the thesis

We conducted a series of experimental studies in heat transport across nano and micro scale materials. At the nano scale, we studied heat transport across exfoliated monolayer and few layer MoS<sub>2</sub>. We deposited all MoS<sub>2</sub> samples on SiO<sub>2</sub> and mica substrates and we coated them with a metal transducer layer on top in order to enable the measurement. For these reasons, we treated MoS<sub>2</sub> as an interface and we measured an effective thermal interface conductance that encompassed the interface between the transducer layer and the MoS<sub>2</sub>, the MoS<sub>2</sub> layer(s) and the interface between the MoS<sub>2</sub> and the substrate. It was not possible to obtain a measurement of only the MoS<sub>2</sub> layer(s) since our technique lacks sensitivity for that. We found that heat transport across MoS<sub>2</sub> decreased with the number of layers, especially from monolayer MoS<sub>2</sub> to three layer. In case of the SiO<sub>2</sub> substrate, heat transfer was 3 times better for monolayer MoS<sub>2</sub> while in the case of mica, heat transfer was 2 times better for monolayer in comparison to few layer MoS<sub>2</sub>.

At the micro scale, we developed a model to measure thermal properties of individual micro particles. We realized that we could also use FDTR to measure the dimensions or size of these particles, which is a novelty since so far FDTR has been used to measure thermal properties of thin films. We found that the thermal model developed for the particle case predicted the phase response with accuracy. We conducted several measurements on diamond and silicon particles with sizes ranging

between 10 and 60  $\mu\text{m}$  in diameter. In both cases, we were able to obtain the thermal conductivity of each particle and its volume.

We then extended this model to include a second material surrounding the particle. This model can be used to represent particles embedded in a matrix material as it happens in particle reinforced composite materials. The purpose of this model was to measure the thermal interface conductance between a particle and the matrix material in real conditions. We solved the model numerically via MATLAB's PDE toolbox. We investigated the cases in which FDTR would be sensitive to the particle-matrix thermal interface conductance ( $G$ ). We found that high thermal conductivity matrix materials and small particles increase the sensitivity to  $G$ . We tested the model by fabricating and measuring samples consisting of diamond micro particles (20-30  $\mu\text{m}$ ) embedded in pure tin. To the author's best knowledge, this is the first time a measurement of this type has been done. We think it could be useful for those sectors in industry developing composite materials for thermal management purposes.

## References

- Abyzov, A. M., Kidalov, S. V., and Shakhov, F. M. (2012). High thermal conductivity composite of diamond particles with tungsten coating in a copper matrix for heat sink application. *Applied Thermal Engineering*, 48:72–80.
- Alam, M., Raghu, A., Haque, M., Muratore, C., and Voevodin, A. (2013). Structural size and temperature dependence of solid to air heat transfer. *International Journal of Thermal Sciences*, 73:1–7.
- Arfken, G. B., Weber, H. J., and Harris, F. E. (2013). Sturm-Liouville Theory. In *Mathematical Methods for Physicists*, pages 381–399. Elsevier.
- Asheghi, M., Kurabayashi, K., Kasnavi, R., and Goodson, K. E. (2002). Thermal conduction in doped single-crystal silicon films. *Journal of Applied Physics*, 91(8):5079–5088.
- ASM International Staff (1991). ASM Handbook: Vol. 2 Properties and Selection: Nonferrous Alloys and Special-Purpose Materials.
- Bar-Cohen, A., Albrecht, J. D., and Maurer, J. J. (2011). Near-Junction Thermal Management for Wide Bandgap Devices. In *2011 IEEE Compound Semiconductor Integrated Circuit Symposium (CSICS)*, pages 1–5. IEEE.
- Barman, S. and Srivastava, G. P. (2007). Temperature dependence of the thermal conductivity of different forms of diamond. *Journal of Applied Physics*, 101(12):123507.
- Burgemeister, E. A., von Muench, W., and Pettenpaul, E. (1979). Thermal conductivity and electrical properties of 6 H silicon carbide. *Journal of Applied Physics*, 50(9):5790–5794.
- Buscema, M., Barkelid, M., Zwiller, V., Van Der Zant, H. S. J., Steele, G. A., and Castellanos-Gomez, A. (2013). Large and tunable photothermoelectric effect in single-layer MoS<sub>2</sub>. *Nano Letters*, 13(2):358–363.
- Cahill, D. G. (1990). Thermal conductivity measurement from 30 to 750 K: The  $3\omega$  method. *Review of Scientific Instruments*, 61(2):802–808.
- Chen, J., Zhang, G., and Li, B. (2013). Substrate coupling suppresses size dependence of thermal conductivity in supported graphene. *Nanoscale*, 5(2):532–536.

- Chu, K., Liu, Z., Jia, C., Chen, H., Liang, X., Gao, W., Tian, W., and Guo, H. (2010). Thermal conductivity of SPS consolidated Cu/diamond composites with Cr-coated diamond particles. *Journal of Alloys and Compounds*, 490(1-2):453–458.
- Chung, D. (2001a). Materials for thermal conduction. *Applied Thermal Engineering*, 21:1593–1605.
- Chung, D. (2001b). Thermal Interface Materials. *Journal of Materials Engineering and Performance*, 10(1):56–59.
- Collins, A. K., Pickering, M. A., and Taylor, R. L. (1990). Grain-Size Dependence of the Thermal-Conductivity of Polycrystalline Chemical Vapor-Deposited Beta-SiC at Low-Temperatures. *Journal of Applied Physics*, 68(12):6510–6512.
- Collins, K. C., Chen, S., and Chen, G. (2010). Effects of surface chemistry on thermal conductance at aluminum-diamond interfaces. *Applied Physics Letters*, 97(8):1–4.
- Corporation, G. T. (2016). Goushou technology corporation. <http://goushou-tech.com.tw/Products/Thermal-Management/Thermal-Interface-Materials.php>.
- Crocombette, J.-P. and Gelebart, L. (2009). Multiscale modeling of the thermal conductivity of polycrystalline silicon carbide. *Journal of Applied Physics*, 106(8):083520.
- Davis, L. C. and Artz, B. E. (1995). Thermal conductivity of metalmatrix composites. *Journal of Applied Physics*, 77(10):4954–4960.
- Every, A. G., Tzou, Y., Hasselman, D. P., and Raj, R. (1992). The effect of particle size on the thermal conductivity of ZnS/diamond composites. *Acta Metallurgica Et Materialia*, 40(1):123–129.
- Fiori, G., Bonaccorso, F., Iannaccone, G., Palacios, T., Neumaier, D., Seabaugh, A., Banerjee, S. K., and Colombo, L. (2014). Electronics based on two-dimensional materials. *Nature Nanotechnology*, 9(10):768–779.
- Ghosh, S., Calizo, I., Teweldebrhan, D., Pokatilov, E. P., Nika, D. L., Balandin, A. A., Bao, W., Miao, F., and Lau, C. N. (2008). Extremely high thermal conductivity of graphene: Prospects for thermal management applications in nanoelectronic circuits. *Applied Physics Letters*, 92(15):151911.
- Gray, A. S. and Uher, C. (1977). Thermal conductivity of mica at low temperatures. *Journal of Materials Science*, 12(5):959–965.
- Gu, X. and Yang, R. (2016). Phonon transport and thermal conductivity in two-dimensional materials. *Annual Review of Heat Transfer*.

- Guan, N., Liu, Z., Zhang, C., and Jiang, G. (2014). Natural convection heat transfer on surfaces of copper micro-wires. *Heat and Mass Transfer*, 50(2):275–284.
- Gundrum, B. C., Cahill, D. G., and Averback, R. S. (2005). Thermal conductance of metal-metal interfaces. *Physical Review B*, 72(24):245426.
- Gustavsson, M., Karawacki, E., and Gustafsson, S. E. (1994). Thermal conductivity, thermal diffusivity, and specific heat of thin samples from transient measurements with hot disk sensors. *Review of Scientific Instruments*, 65(12):3856–3859.
- Hsieh, W.-P., Chen, B., Li, J., Koblinski, P., and Cahill, D. G. (2009). Pressure tuning of the thermal conductivity of the layered muscovite crystal. *Physical Review B*, 80(18):180302.
- Hu, X. J., Jain, A., and Goodson, K. E. (2008). Investigation of the natural convection boundary condition in microfabricated structures. *International Journal of Thermal Sciences*, 47(7):820–824.
- Ji, Q., Zhang, Y., Gao, T., Zhang, Y., Ma, D., Liu, M., Chen, Y., Qiao, X., Tan, P. H., Kan, M., Feng, J., Sun, Q., and Liu, Z. (2013). Epitaxial monolayer MoS<sub>2</sub> on mica with novel photoluminescence. *Nano Letters*, 13(8):3870–3877.
- Jiang, G., Diao, L., and Kuang, K. (2013). *Advanced Thermal Management Materials*. Springer New York, NY.
- Kidalov, S. and Shakhov, F. (2009). Thermal Conductivity of Diamond Composites. *Materials*, 2(4):2467–2495.
- Kim, J. Y., Choi, S. M., Seo, W. S., and Cho, W. S. (2010). Thermal and electronic properties of exfoliated metal chalcogenides. *Bulletin of the Korean Chemical Society*, 31(11):3225–3227.
- Kim, S. J., Choi, K., Lee, B., Kim, Y., and Hong, B. H. (2015). Materials for Flexible, Stretchable Electronics: Graphene and 2D Materials. *Annual Review of Materials Research*, 45(1):63–84.
- Koh, Y. K., Bae, M.-H., Cahill, D. G., and Pop, E. (2010). Heat Conduction across Monolayer and Few-Layer Graphenes. *Nano Letters*, 10(11):4363–4368.
- Lakshminarayanan, V. and Sriraam, N. (2014). The effect of temperature on the reliability of electronic components. In *2014 IEEE International Conference on Electronics, Computing and Communication Technologies (CONECCT)*, pages 1–6. IEEE.
- Lee, Y. and Hwang, G. S. (2012). Mechanism of thermal conductivity suppression in doped silicon studied with nonequilibrium molecular dynamics. *Physical Review B*, 86(7):075202.

- Leong, W. S., Luo, X., Li, Y., Khoo, K. H., Quek, S. Y., and Thong, J. T. L. (2015). Low resistance metal contacts to MoS<sub>2</sub> devices with nickel-etched-graphene electrodes. *ACS Nano*, 9(1):869–877.
- Li, H., Zhang, Q., Yap, C. C. R., Tay, B. K., Edwin, T. H. T., Olivier, A., and Baillargeat, D. (2012a). From Bulk to Monolayer MoS<sub>2</sub>: Evolution of Raman Scattering. *Advanced Functional Materials*, 22(7):1385–1390.
- Li, W., Mingo, N., Lindsay, L., Broido, D. A., Stewart, D. A., and Katcho, N. A. (2012b). Thermal conductivity of diamond nanowires from first principles. *Physical Review B*, 85(19):195436.
- Li, Y. and Wong, C. (2006). Recent advances of conductive adhesives as a lead-free alternative in electronic packaging: Materials, processing, reliability and applications. *Materials Science and Engineering: R: Reports*, 51(1-3):1–35.
- Lienhard IV, J. H. and Lienhard V, J. H. (2012). *A HEAT TRANSFER TEXTBOOK fourth edition*.
- Liu, J., Choi, G.-m., and Cahill, D. G. (2014). Measurement of the anisotropic thermal conductivity of molybdenum disulfide by the time-resolved magneto-optic Kerr effect. *Journal of Applied Physics*, 116(23):233107.
- Losego, M. D., Grady, M. E., Sottos, N. R., Cahill, D. G., and Braun, P. V. (2012). Effects of chemical bonding on heat transport across interfaces. *Nature Materials*, 11(6):502–506.
- Mak, K. F., Lee, C., Hone, J., Shan, J., and Heinz, T. F. (2010). Atomically thin MoS<sub>2</sub>: A new direct-gap semiconductor. *Physical Review Letters*, 105(13):136805.
- Man, M. K. L., Deckoff-Jones, S., Winchester, A., Shi, G., Gupta, G., Mohite, A. D., Kar, S., Kioupakis, E., Talapatra, S., and Dani, K. M. (2016). Protecting the properties of monolayer MoS<sub>2</sub> on silicon based substrates with an atomically thin buffer. *Scientific Reports*, 6(1):20890.
- Mattila, T., Li, J., and Kivilahti, J. (2012). On the effects of temperature on the drop reliability of electronic component boards. *Microelectronics Reliability*, 52(1):165–179.
- Mir, I. and Kumar, D. (2008). Recent advances in isotropic conductive adhesives for electronics packaging applications. *International Journal of Adhesion and Adhesives*, 28(7):362–371.
- Molina, J. M., Narciso, J., Weber, L., Mortensen, A., and Louis, E. (2008). Thermal conductivity of Al-SiC composites with monomodal and bimodal particle size distribution. *Materials Science and Engineering A*, 480(1-2):483–488.

- Muratore, C., Varshney, V., Gengler, J. J., Hu, J., Bultman, J. E., Roy, A. K., Farmer, B. L., and Voevodin, A. a. (2014). Thermal anisotropy in nano-crystalline MoS<sub>2</sub> thin films. *Physical Chemistry Chemical Physics*, 16(3):1008–1014.
- Nan, C.-W., Birringer, R., Clarke, D. R., and Gleiter, H. (1997). Effective thermal conductivity of particulate composites with interfacial thermal resistance. *Journal of Applied Physics*, 81(10):6692–6699.
- Nipane, A., Karmakar, D., Kaushik, N., Karande, S., and Lodha, S. (2016). Few-Layer MoS<sub>2</sub> p-Type Devices Enabled by Selective Doping Using Low Energy Phosphorus Implantation. *ACS Nano*, 10(2):2128–2137.
- Novoselov, K. S., Jiang, D., Schedin, F., Booth, T. J., Khotkevich, V. V., Morozov, S. V., and Geim, A. K. (2005). Two-dimensional atomic crystals. *Proceedings of the National Academy of Sciences of the United States of America*, 102(30):10451–10453.
- Olson, J. R., Pohl, R. O., Vandersande, J. W., Zoltan, A., Anthony, T. R., and Banholzer, W. F. (1993). Thermal conductivity of diamond between 170 and 1200 K and the isotope effect. *Physical Review B*, 47(22):14850–14856.
- Ozisik, M. (2013). *Boundary Value Problems of Heat Conduction*. Dover Publications.
- Parker, W. J., Jenkins, R. J., Butler, C. P., and Abbott, G. L. (1961). Flash method of determining thermal diffusivity, heat capacity, and thermal conductivity. *Journal of Applied Physics*, 32(9):1679–1684.
- Pietrak, K. and Winiewski, T. S. (2015). A review of models for effective thermal conductivity of composite materials. *Open Access Journal Journal of Power Technologies*, 95(1):14–24.
- Prasher, R. (2006). Thermal Interface Materials: Historical Perspective, Status, and Future Directions. *Proceedings of the IEEE*, 94(8):1571–1586.
- Quereda, J., Castellanos-Gomez, A., Agrait, N., and Rubio-Bollinger, G. (2014). Single-layer MoS<sub>2</sub> roughness and sliding friction quenching by interaction with atomically flat substrates. *Applied Physics Letters*, 105(5):2012–2017.
- Regner, K. T., Sellan, D. P., Su, Z., Amon, C. H., McGaughey, A. J., and Malen, J. A. (2013). Broadband phonon mean free path contributions to thermal conductivity measured using frequency domain thermoreflectance. *Nature Communications*, 4:1640.
- Ruch, P. W., Beffort, O., Kleiner, S., Weber, L., and Uggowitzer, P. J. (2006). Selective interfacial bonding in Al(Si)-diamond composites and its effect on thermal conductivity. *Composites Science and Technology*, 66(15):2677–2685.

- Sahoo, S., Gaur, A. P. S., Ahmadi, M., Guinel, M. J.-F., and Katiyar, R. S. (2013). Temperature-Dependent Raman Studies and Thermal Conductivity of Few-Layer MoS<sub>2</sub>. *The Journal of Physical Chemistry C*, 117(17):9042–9047.
- Sarvar, F., Whalley, D., and Conway, P. (2006). Thermal Interface Materials - A Review of the State of the Art. *2006 1st Electronic Systemintegration Technology Conference*, 2:1292–1302.
- Schmidt, A. J., Cheaito, R., and Chiesa, M. (2009). A frequency-domain thermoreflectance method for the characterization of thermal properties. *The Review of scientific instruments*, 80(9):094901.
- Schwierz, F., Pezoldt, J., and Granzner, R. (2015). Two-dimensional materials and their prospects in transistor electronics. *Nanoscale*, 7(18):8261–8283.
- Seol, J. H., Jo, I., Moore, A. L., Lindsay, L., Aitken, Z. H., Pettes, M. T., Li, X., Yao, Z., Huang, R., Broido, D., Mingo, N., Ruoff, R. S., and Shi, L. (2010). Two-Dimensional Phonon Transport in Supported Graphene. *Science*, 328(5975):213–216.
- Slack, G. A. (1964). Thermal conductivity of pure and impure silicon, silicon carbide, and diamond. *Journal of Applied Physics*, 35(12):3460–3466.
- Tan, K. S., Wong, Y. H., and Cheong, K. Y. (2015). Thermal characteristic of sintered Ag–Cu nanopaste for high-temperature die-attach application. *International Journal of Thermal Sciences*, 87:169–177.
- Taube, A., Judek, J., Lapińska, A., and Zdrojek, M. (2015). Temperature-Dependent Thermal Properties of Supported MoS<sub>2</sub> Monolayers. *ACS Applied Materials & Interfaces*, 7(9):5061–5065.
- Tavangar, R. and Weber, L. (2012). Silver-based diamond composites with highest thermal conductivity. *Emerging Materials Research*, 1(2):67–74.
- Tekce, H. S., Kumlutas, D., and Tavman, I. H. (2007). Effect of Particle Shape on Thermal Conductivity of Copper Reinforced Polymer Composites. *Journal of Reinforced Plastics and Composites*, 26(1):113–121.
- Tong, X. C. (2011). *Advanced Materials for Thermal Management of Electronic Packaging*. Springer-Verlag New York.
- Touloukian, Y. S. and Buyco, E. H. (1970). *The Thermophysical Properties of Matter: The TPRC Data Series*. Plenum, New York.
- Wang, Q. H., Kalantar-Zadeh, K., Kis, A., Coleman, J. N., and Strano, M. S. (2012). Electronics and optoelectronics of two-dimensional transition metal dichalcogenides. *Nature Nanotechnology*, 7(11):699–712.

- Watanabe, H. (2002). Further examination of the transient hot-wire method for the simultaneous measurement of thermal conductivity and thermal diffusivity. *Metrologia*, 39(1):65–81.
- Xu, Y. and Chung, D. D. L. (2000). Increasing the thermal conductivity of boron nitride and aluminum nitride particle epoxy-matrix composites by particle surface treatments. *Composite Interfaces*, 7(4):243–256.
- Yamamoto, Y., Imai, T., Tanabe, K., Tsuno, T., Kumazawa, Y., and Fujimori, N. (1997). The measurement of thermal properties of diamond. *Diamond and Related Materials*, 6(96):1057–1061.
- Yan, R., Simpson, J. R., Bertolazzi, S., Brivio, J., Watson, M., Wu, X., Kis, A., Luo, T., Hight Walker, A. R., and Xing, H. G. (2014). Thermal Conductivity of Monolayer Molybdenum Disulfide Obtained from Temperature-Dependent Raman Spectroscopy. *ACS Nano*, 8(1):986–993.
- Yang, J., Maragliano, C., and Schmidt, A. J. (2013). Thermal property microscopy with frequency domain thermoreflectance. *Review of Scientific Instruments*, 84(10):104904.
- Yang, J., Ziade, E., Maragliano, C., Crowder, R., Wang, X., Stefancich, M., Chiesa, M., Swan, A. K., and Schmidt, A. J. (2014). Thermal conductance imaging of graphene contacts. *Journal of Applied Physics*, 116(2):023515.
- Yang, J., Ziade, E., and Schmidt, A. J. (2016). Uncertainty analysis of thermoreflectance measurements. *Review of Scientific Instruments*, 87(1):014901.
- Yu, Y., Li, C., Liu, Y., Su, L., Zhang, Y., and Cao, L. (2013). Controlled Scalable Synthesis of Uniform, High-Quality Monolayer and Few-layer MoS<sub>2</sub> Films. *Scientific Reports*, 3(1):1866.
- Zeng, L., Collins, K. C., Hu, Y., Luckyanova, M. N., Maznev, A. A., Huberman, S., Chiloyan, V., Zhou, J., Huang, X., Nelson, K. A., and Chen, G. (2015). Measuring Phonon Mean Free Path Distributions by Probing Quasiballistic Phonon Transport in Grating Nanostructures. *Scientific Reports*, 5(1):17131.
- Zhang, X., Sun, D., Li, Y., Lee, G.-H., Cui, X., Chenet, D., You, Y., Heinz, T. F., and Hone, J. C. (2015). Measurement of Lateral and Interfacial Thermal Conductivity of Single- and Bilayer MoS<sub>2</sub> and MoSe<sub>2</sub> Using Refined Optothermal Raman Technique. *ACS Applied Materials & Interfaces*, 7(46):25923–25929.

# CURRICULUM VITAE

